

© Copyright by Joseph Edward Hilliard Jr., 2001

CONDUCTIVITY AND INTERFEROMETRY EXPERIMENTS ON YBCO/Pb RAMP-
EDGE JOSEPHSON JUNCTIONS

BY

JOSEPH EDWARD HILLIARD JR.

B.S., Massachusetts Institute of Technology, 1989
M.S., University of Illinois at Urbana-Champaign, 1992

THESIS

Submitted in partial fulfillment of the requirements
for the degree of Doctor of Philosophy in Physics
in the Graduate College of the
University of Illinois at Urbana-Champaign, 2001

Urbana, Illinois

CONDUCTIVITY AND INTERFEROMETRY EXPERIMENTS ON YBCO/Pb RAMP-EDGE JOSEPHSON JUNCTIONS

Joseph Edward Hilliard Jr., Ph.D.
Department of Physics
University of Illinois at Urbana-Champaign, 2001
Dale J. Van Harlingen, Advisor

In this thesis, we study the details of the order parameter symmetry in arbitrary directions of the high-temperature cuprate superconductor $\text{YBa}_2\text{Cu}_3\text{O}_{7-y}$ (YBCO) using YBCO/Pb ramp-edge Josephson junctions with lithographically defined corner and straight-edge geometries. Measurements of the critical current versus applied field, $I_c(H)$, and the dynamic conductance, dI/dV , are presented. For junctions with corner geometries, as well as for most of the straight-edge junctions, the known $d_{x^2-y^2}$ order parameter symmetry of YBCO is confirmed. For some of the straight-edge junctions oriented near 45° with respect to the YBCO a and b axes, an anomalous temperature dependence of the $I_c(H)$ pattern is found in the range from 5 down to 1.4 K. We consider the onset of a secondary order parameter and the onset of second-order Josephson coupling as possible interpretations of this anomalous temperature dependence and we find the second-order Josephson coupling interpretation more likely.

To my family and to Sts. Joseph and Jude who were invoked on my behalf.

ACKNOWLEDGMENTS

There have been many people who have helped me along the path to this Ph. D. thesis. I will do my best to acknowledge them in this section, but I apologize in advance to anyone I might inadvertently leave out.

Let me begin by thanking my advisor, Prof. Dale Van Harlingen. His knowledge and experience in low temperature experimental physics, his connections to theorists and others who knew right answers that we needed, his collegial attitude toward his students, and his general goodwill have made him an ideal advisor and a good friend. I wish to thank him in particular for his hand-on assistance with low temperature electrical measurements in the lab and also for keeping me, and all his students, well funded and well equipped. The work of this thesis has been supported the National Science Foundation under grants NSF-DMR91-20000, NSF-DMR97-05695, and NSF-DMR99-72087, and by the Department of Energy under grant DEFG02-96ER45439.

My other colleagues in the DVH group, Dave Wollman, Joe Walko, Mark Wistrom, Britton Plourde, Brian Yanoff, Kevin Osborn, Eric Tham, Tony Bonetti, Bill Neils, Trevis Crane, Jack Sadleir, Chris Michael, Martin Stehno and Adele Ruosi, also deserve my heartfelt thanks for their help in the lab, ideas in countless physics discussions, feedback on various practice talks I have given, and general friendship and moral support. Among these I wish to thank in particular: Mark Wistrom and Ralph Schweinfurth (who left before I arrived) for their work designing and building the AXL laser ablation system; Joe Walko, Mark Wistrom, and

Britton for training in the cleanroom and on various equipment; Brian Yanoff for assistance with data acquisition programming in Labview, as well as the use of some of his Labview code; Eric Tham for growing some of the YBCO films I used early on; and Tony Bonetti and Bill Neils for help with the frequent repair and maintenance jobs on the laser ablation system.

Among my colleagues outside the DVH group I should thank Prof. Ian Robinson, and especially visiting Prof. Ivan Vartaniants for their collaboration on applying iterative phase reconstruction algorithms to Josephson junction data. I also thank Bruce Davidson, a postdoc with Prof. Jim Eckstein's group, for feedback and advice on my work.

My thesis work has been greatly facilitated by the facilities and staff of the Materials Research Laboratory at the University of Illinois. I spent many hours using the cleanroom and other equipment of the MRL Microfabrication Facility, which is expertly run by Tony Banks, who has the ability to set up or fix nearly anything and from whom I gained a great deal of practical knowledge. I also gratefully acknowledge the help I received from Ray Strange of the MRL Laser Facility, Spencer Shultz and the rest of the machine shop staff, Bill Thrasher of the furnace brazing facility, Susan Johnson of the MRL business office, and Joyce MacMillan, Mauro Sardela, and Steve Burdin of the MRL Center for Microanalysis of Materials. It was in the CMM that I carried out x-ray analysis and stylus profilometry of my films and devices.

Lastly, but closest to my heart, I wish to thank God for the gift of life and the opportunity to study physics, His Church and all my friends therein for sustaining me spiritually, and my mother, father and brother for their constant prayers and support before, during, and after my graduate studies.

TABLE OF CONTENTS

Chapter	Page
1 INTRODUCTION	1
2 UNCONVENTIONAL PAIRING AND ORDER PARAMETER SYMMETRY IN YBCO AND OTHER CUPRATES	6
2.1 Basics of the Order Parameter in the BCS Theory	6
2.2 Unconventional Order Parameter Symmetry	9
2.3 Quasiparticle Evidence for the $d_{x^2-y^2}$ Pairing State	14
2.4 Tunneling Experiments and the Possibility of a Secondary Order Parameter	17
3 JOSEPHSON TUNNELING AS A PROBE OF THE CUPRATE ORDER PARAMETER AND ITS SYMMETRY	23
3.1 Basics of the Josephson Effect	23
3.2 Directionality of the Josephson Effect	27
3.3 Possible Second Order Josephson Coupling	28
3.4 Relevant Past Josephson Experiments on the Cuprates	29
3.4.1 Single Crystal Corner Junctions and SQUIDS	29
3.4.2 SSM Experiments on Tri-crystal Thin Films	40
3.4.3 SSM Experiments on Pb/YBCO Thin Film SQUIDS	43
3.5 Idealized Descriptions of the Experiments in this Thesis	45
3.5.1 Corner Junctions	45
3.5.2 Arbitrary Angle Single Edge Junctions	47
3.5.3 Variable-inductance SQUIDS	49
4 EXPERIMENTAL TECHNIQUES	56
4.1 Fabrication Techniques	56
4.1.1 Pulsed Laser Deposition	58
4.1.2 Photolithography	62
4.1.3 Ion Milling	64
4.1.4 Evaporation	65
4.1.5 Annealing	67
4.1.6 Sputter Deposition	68
4.2 Measurement Techniques	70
4.2.1 Cryogenics, Cryostat Inserts, and Sample Holders	70
4.2.2 Electronics and Data Acquisition for Junctions and SQUIDS	77
4.2.3 Flux Measurement of Variable-inductance Devices	80
5 DATA AND ANALYSIS OF CORNER EXPERIMENTS	83

5.1 Corner Junction Data and Analysis	84
5.1.1 Data and Qualitative Analysis	84
5.1.2 Quantitative Computation of $J_c(y)$ with Appropriate Assumptions	89
5.2 Preliminary Data on Variable-inductance SQUID Experiment	95
6 SINGLE EDGE JUNCTION (SPIDER) DATA AND ANALYSIS	96
6.1 Experimental Critical Current Results and Qualitative Discussion	96
6.1.1 $I_c R_N$ Products	96
6.1.2 $I_c(H)$ Diffraction Patterns	101
6.2 Dynamic Conductance Data (dI/dV)	109
6.3 Realistic Quantitative Simulations and Comparison	113
6.4 Discussion	121
7 SUMMARY AND FUTURE DIRECTIONS	125
REFERENCES	128
VITA	136

Chapter 1

INTRODUCTION

The discovery of high temperature superconductors such as $\text{La}_{2-x}\text{Ba}_x\text{CuO}_4$ (LBCO), (Bednorz 1986) $\text{YBa}_2\text{Cu}_3\text{O}_{7-y}$ (YBCO) (Wu 1987) and others with still higher transition temperatures has opened up a field of both scientific and technological interest in solid state physics. This represents a theoretical challenge since the previously known phonon-mediated mechanism of superconductivity does not occur on a high enough energy scale to produce superconductivity at the 92 K critical temperature of YBCO, for example. While as yet the specific mechanism for pairing in the high-temperature cuprates has not been distinguished, the experimental constraints that a proposed mechanism has to satisfy are narrowing. At the same time, increasingly detailed measurements of the properties of the cuprates have lead to a better understanding of the limitations, as well as the opportunities for applications of these materials.

The main property of the cuprates that this thesis will focus on is the superconducting order parameter, which is essentially the wavefunction of the superconducting state, and in particular on its symmetry properties. Experimental measurements of the order parameter, in particular as a function of momentum direction, can be used to eliminate models that predict the wrong form of the order parameter. Furthermore, knowledge about the order parameter is of technological interest because it affects both the designs of devices made from the high temperature cuprates and the ability to make electrical contact to them with other materials.

Finally, the order parameter is also of intrinsic interest because, as discussed below, the cuprates have been found to have an unconventional order parameter symmetry, that is a symmetry lower than the underlying crystal symmetry. With the exception of the heavy Fermion superconductors (Taillefer 1991), evidence for unconventional symmetry had never been found in any superconductor known before the high T_c cuprates. The main motivation for undertaking the work in this thesis was to gain more detailed knowledge of the unconventional cuprate order parameter, and in particular any changes to it that might be induced by the effects of surfaces at different orientations.

Measurements done in the mid to late 1990's have shown that the order parameter for hole-doped cuprates, which include YBCO and the majority of other cuprates, is of a predominantly $d_{x^2-y^2}$ character, while measurements in the last year or so (Prozorov 2000) show that the electron-doped cuprates, such as $\text{Ne}_{1.85}\text{Ce}_{0.15}\text{CuO}_4$ (NCCO), which was originally thought to have an s-wave order parameter, also appear to be $d_{x^2-y^2}$. The notations s, $d_{x^2-y^2}$ etc. correspond to those of orbitals in atomic physics, although the cuprates are layered planar materials for which only the in-plane (ab plane) momentum directions need be considered. For example, penetration depth (Hardy 1993), NMR (Schlichter 1994), and specific heat measurements (Moler 1994), which probe the number of quasi-particle excitations, showed a polynomial rather than exponential dependence on temperature at low temperatures for various hole-doped cuprates, implying that the energy gap (which is usually proportional to the order parameter) must approach zero for at least some directions in k-space.

More direct direction-sensitive measurements of the order parameter and the energy gap in hole-doped cuprates have been done by quasi-particle tunneling(Kane 1996), Josephson tunneling(Wollman 1993; Tsuei 1994; Mathai 1995; Van Harlingen 1995; Wollman 1995; Gim 1996; Tsuei 1996) and angle resolved photoemission spectroscopy (ARPES)(Shen 1993; Ding 1996a; Ding 1996b). Of particular interest are the Josephson tunneling experiments on single crystals (corner SQUIDs and junctions) by Wollman *et al*(Wollman 1993; Wollman 1995). These experiments, which take advantage the Josephson effect's directionality, and its dependence on the phase of the order parameter were the first truly phase sensitive measurements of the order parameter. By looking at the Josephson critical current and related quantities as a function of applied magnetic flux, these experiments showed that the order parameter has a sign change for directions differing by 90 degrees in k-space. This result was confirmed by Kirtley and Tsuei *et al.*,(Tsuei 1994; Tsuei 1996) who used scanning SQUID microscopy (SSM) to observe the spontaneous magnetic flux in rings of thin film cuprate superconductors with Josephson junctions formed at the grain boundaries of their SrTiO₃ tricrystal substrates. Further confirmation has been provided by Wellstood *et al.* (Mathai 1995; Gim 1996) who performed SSM experiments on thin film Pb/Ag/YBCO corner SQUIDs with various junction plane orientations.

Since 1997, evidence has been reported for the possible existence of a secondary order parameter in YBCO near a surface. Theoretical work has shown (Hu 1994)(Buchholtz 1995) that a $d_{x^2-y^2}$ wave superconductor will exhibit a suppression of the order parameter within a few coherence lengths of a specularly reflecting surface not oriented in the a- or b-axis

directions, with the strongest suppression for the (110) direction. The same effect would also be expected at a diffuse surface because most facets of it would not be oriented in the a- or b-axis directions. In regions where this suppression happens, an alternative pairing mechanism which leads to a symmetry other than $d_{x^2-y^2}$ can take effect. Calculations show that it is most energetically favorable for the resulting secondary order parameter to be $\pi/2$ radians out of phase with the bulk $d_{x^2-y^2}$ order parameter resulting in an overall $d_{x^2-y^2} + i, s$ or $d_{x^2-y^2} + i, d_{xy}$ order parameter near the surface. (Buchholtz 1995)(Matsumoto 1995) Possible evidence for this effect has been seen in YBCO/Cu tunnel junctions (Covington 1997a; b) where a low temperature splitting of a zero bias conductance peak has been interpreted in terms of the expected surface currents from the $\pi/2$ phase difference. Other possible evidence comes from penetration depth measurements (Walter 1998) where an anomalous increase in the penetration depth near artificial boundaries created by ion damage tracks in YBCO oriented at 22.5 and 45 degrees is attributed to surface currents of the same origin.

In this thesis, further studies are made on the cuprate order parameter based on the Josephson effect in thin film devices made from YBCO, a noble metal barrier, and a second, conventional, superconductor with a ramp-edge technology. These results fall into two general categories. First, for junctions with corner geometries, of various angles, measurements that confirm the known $d_{x^2-y^2}$ order parameter are presented. Also in this first category are preliminary results on a novel variable inductance corner SQUID experiment intended as an alternative method for Josephson order parameter measurements. The second category of results is for edge junctions oriented in various single directions ranging over 180° . For most of

these junctions, the results are consistent with the known $d_{x^2-y^2}$ order parameter of YBCO, but for some within about 10° of the (110) direction, anomalous temperature dependences of the Josephson critical current are seen. We will consider and discuss the possible secondary surface order parameter mentioned above, and possible second-order Josephson coupling as potential interpretations of these anomalous temperature dependences.

The remainder of this thesis is organized as follows. Chapter 2 covers the definition of conventional and unconventional order parameter symmetries in the context of the BCS theory of superconductivity, the relevant past work on the cuprate order parameter (except Josephson experiments), and the suppression of the $d_{x^2-y^2}$ order parameter and possible onset of a secondary order parameter near a surface.. Chapter 3 discusses the Josephson effect in general, the possibility of second-order Josephson coupling, the use of the Josephson effect in past studies of the cuprate order parameter, and an idealized description of the Josephson experiments in this thesis. Chapter 4 explains the details of device fabrication and experimental measurements for this thesis. In chapter 5, the results of the corner junction experiments and preliminary results of the variable inductance SQUID experiment are presented and discussed, while in chapter 6, the results and discussion of the single-direction edge junctions are covered. Finally, chapter 7 summarizes the conclusions of and possible future directions for this work.

Chapter 2

UNCONVENTIONAL PAIRING AND ORDER PARAMETER SYMMETRY IN YBCO AND OTHER CUPRATES

Since this thesis deals primarily with the order parameter of the cuprates, particularly YBCO, we shall begin by defining what the superconducting order parameter (OP) is and discuss some of the symmetry properties that it may possess, in particular, the definition of the so-called unconventional symmetry. With this background in hand, we shall go on to discuss the relevant experiments and theory of the order parameter in the cuprates, both in the bulk and near a surface, again with particular reference to YBCO.

2.1 Basics of the Order Parameter in the BCS Theory

According to the Bardeen-Cooper-Schrieffer theory (BCS)(Bardeen 1957) superconductivity is the result of phase coherence among paired electrons. This many- particle phase coherent state is the result of an effective attraction between electrons in the superconductor which at least for some subset of electron states near the Fermi level is strong enough to overcome the electronic coulomb repulsion. In the case of classical BCS superconductors, this effective attraction between electrons is provided by a retarded interaction with lattice phonons. The macroscopic occupation of this phase coherent state makes it impossible for the normal single electron scattering mechanism of electrical resistance to operate and hence accounts for the persistent currents observed in superconductivity. The

phase coherent state can be described by a single complex order parameter, which in general can vary in space and time.

In second quantized notation, the BCS state with phase θ and Cooper pair momentum $2\mathbf{k}$ is given by

$$\prod_{\mathbf{k}} (u_{\mathbf{k}} + e^{i\theta} v_{\mathbf{k}} c_{\mathbf{k}+\mathbf{s}\uparrow}^{\dagger} c_{-\mathbf{k}+\mathbf{s}\downarrow}^{\dagger}) |0\rangle$$

where the sum is over momentum states, $|0\rangle$ is a state with no electrons, the c^{\dagger} 's are electron creation operators, and the u 's and v 's are complex numbers known as coherence factors which are the probability amplitudes for a Cooper pair state to be respectively unoccupied or occupied. The BCS ground state has $\mathbf{s} = 0$ and does not carry any supercurrent. Conversely, uniform current carrying states have $\mathbf{s} \neq 0$, but still very small compared to the Fermi momentum. More complicated current carrying BCS states can in principle be constructed, but usually it is simpler to deal with such states in a non-microscopic theory such as the Ginzburg-Landau theory (Ginzburg 1950). It is not our purpose to consider such states in detail here.

In the original BCS argument (at zero temperature), the order parameter $\Delta_{\mathbf{k}}$ is defined in the course of determining by a variational calculation the set of u 's and v 's which minimize the energy of the BCS state. This definition is given by

$$\Delta_{\mathbf{k}} = -\sum_{\mathbf{k}'} u_{\mathbf{k}'} v_{\mathbf{k}} V_{\mathbf{k}\mathbf{k}'}$$

where $V_{\mathbf{k}\mathbf{k}'}$ is the interaction matrix element between electrons in states \mathbf{k}' and \mathbf{k} . When the variational problem for the minimum energy is solved, it is found that

$$u_{\mathbf{k}}^2 = \frac{1}{2} \left(1 + \frac{e_{\mathbf{k}}}{E_{\mathbf{k}}} \right)$$

$$v_{\mathbf{k}}^2 = \frac{1}{2} \left(1 - \frac{e_{\mathbf{k}}}{E_{\mathbf{k}}} \right)$$

where $e_{\mathbf{k}}$ is the electron energy of state \mathbf{k} (relative to the Fermi energy) in the absence of pairing, $E_{\mathbf{k}}$, which will turn out to be the energy of the elementary excitations (quasiparticles) above the BCS state, is the positive root of

$$E_{\mathbf{k}}^2 = e_{\mathbf{k}}^2 + \Delta_{\mathbf{k}}^2$$

and $\Delta_{\mathbf{k}}$ must satisfy the self-consistency equation

$$\Delta_{\mathbf{k}} = - \sum_{\mathbf{k}'} \frac{\Delta_{\mathbf{k}'}}{2E_{\mathbf{k}'}} V_{\mathbf{k}\mathbf{k}'}$$

Note that the quasiparticles, which in general can be electron-like or hole-like cannot have energy lower than $\Delta_{\mathbf{k}}$. For this reason, order parameter, $\Delta_{\mathbf{k}}$ is also referred to as the energy gap in the quasiparticle spectrum, or just the gap.

Now, in order for the BCS state to have lower energy than the ordinary Fermi sea state

($\Delta_{\mathbf{k}}=0$), $V_{\mathbf{k}'\mathbf{k}}$ must be negative (attractive) for at least some subset of \mathbf{k}',\mathbf{k} . For classical phonon-mediated low- T_c superconductors $V_{\mathbf{k}'\mathbf{k}}$ is well approximated in the BCS theory by

$$V_{\mathbf{k}'\mathbf{k}} = -V_0 : \mathbf{e}_F - \hbar\omega_C < \mathbf{e}_{\mathbf{k}'}, \mathbf{e}_{\mathbf{k}} < \mathbf{e}_F + \hbar\omega_C ,$$

$$\dots\dots = 0 : \textit{otherwise}$$

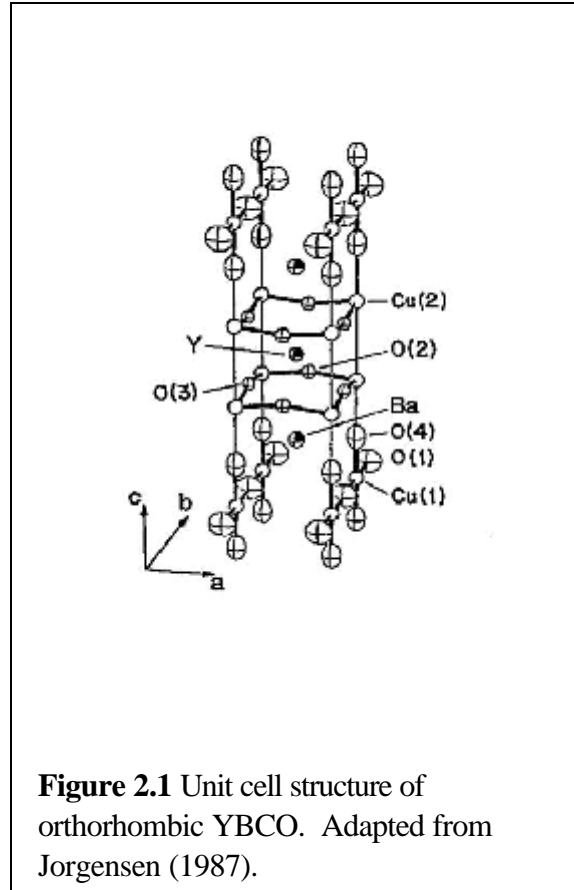
where T_c is a cutoff frequency of the order of Debye frequency of the material. This results in a spherically symmetric $\Delta_{\mathbf{k}}$, given in the so-called weak-coupling limit ($NV_0 \ll 1$) by

$$\Delta_{\mathbf{k}} = \Delta_0 = 2\hbar\omega_C e^{-1/NV_0}$$

where N is the density of states at the Fermi level in the normal state. This spherically symmetric $\Delta_{\mathbf{k}}$ is called an s-wave pairing state in analogy with s states in atomic physics. Of course there will be some distortion due to the fact that crystals do not have arbitrary rotational symmetry, but the term s-wave pairing is generally used interchangeably to mean either an idealized spherically-symmetric pairing state or realistic pairing state which possess the full symmetry of the crystal in question.

2.2 Unconventional Order Parameter Symmetry

In the case of YBCO and other cuprates, however, $\Delta_{\mathbf{k}}$ is more complicated. To understand this, we first consider the crystal structure of the cuprates. The unit cell (Jorgensen 1987) of YBCO is shown in figure 2.1 and has dimensions $a = 3.81\text{\AA}$, $b=3.88\text{\AA}$, $c=11.66\text{\AA}$ at



optimal oxygen doping. Like all the cuprates, the electrical conduction in YBCO occurs primarily in the CuO_2 planes (i.e. normal to the c direction), while the other elements of the unit cell act to fix the separation of the CuO_2 planes and act as charge reservoirs. The charge carriers are holes in the case of YBCO and most other cuprates, but are electrons in the case of cuprates containing Ce such as $\text{Nd}_{1-x}\text{Ce}_x\text{CuO}_4$ (NCCO) and $\text{Pr}_{1-x}\text{Ce}_x\text{CuO}_4$ (PCCO). The dominance of the CuO_2 planes in cuprate conduction results in an effective 2D Fermi surface and hence a 2D order parameter, χ_k .

Secondly, we note that the interaction causing the effective attraction between charge carriers cannot be the same phonon-mediated interaction found in the low- T_C case because the

energy scale for the phonon interaction $\hbar T_D$ is much smaller than the pairing energy scale $k_B T_C$ for the cuprates, where T_C is 92K for YBCO and even higher for some other cuprates. Now, while it is possible that the stronger attractive mechanism responsible for cuprate pairing will retain the full s-wave symmetry of χ_k (in 2D) of the classical phonon mechanism, this need not be so. When χ_k has less than the full crystal symmetry in k-space, it is referred to as unconventional pairing symmetry. Alternatively, unconventional symmetry can be seen in the real space pair wavefunction $N(\mathbf{x}_1 - \mathbf{x}_2)$, which is related to χ_k by a Fourier transform, when $N(\mathbf{x}_1 - \mathbf{x}_2)$ has less than the full crystal symmetry in real space.

The possible pairing symmetries, both conventional and unconventional, for the cuprates have been reviewed in full generality by Annett *et al.* (Annett 1990). Applying group theory to a general expression for the Ginzburg-Landau free energy near T_c , they reach the conclusion that the order parameter must belong to one of several distinct symmetry classes, and that barring a second phase transition, the symmetry class of the order parameter will not change as the temperature is lowered below T_c . (For a detailed discussion of the use of group theory in quantum mechanical problems, the reader is referred to the textbook by Tinkham (Tinkham 1964)). Technically, these symmetry classes are called irreducible representations of the symmetry group of the cuprate crystal. From here, they continue their analysis by enumerating all the irreducible representations consistent with the crystal structure of the cuprates and their corresponding possible functional forms for the order parameter.

We will not repeat the exhaustive enumeration, but instead briefly discuss the most important possibilities. To begin with, we note that the cuprate carriers have been shown by

NMR Knight shift measurements (Barrett 1991) to be paired as spin singlets. This eliminates from consideration the complicated 3-component order parameter states such as those seen in ^3He that would be associated with spin triplet pairing. It also implies that the orbital part of the pair wave function, and hence also $\chi_{\mathbf{k}}$ must have even parity under inversion.

Secondly, since the a and b cell dimensions of YBCO are within 3% of each other, it is useful to approximate YBCO as tetragonal and then consider the effect of the small orthorhombic distortion as a perturbation. In fact, there are other cuprates such as $\text{Tl}_2\text{Ba}_2\text{CuO}_6$ (Tl2201), which are rigorously tetragonal. Further, the effect of the orthorhombic distortion in YBCO is expected to average out in the laser ablated YBCO films used in the experiments of this thesis because of twinning of the YBCO, i.e. the formation of domains with the a and b axes interchanged, on the simple cubic substrates used. The typical size of these twin domains is of the order of the growth island size, $\sim 100\text{nm}$, compared to a typical smallest lithographic feature of $10\ \mu\text{m}$.

Thus, we list in table 2.1 the remaining possible pairing states corresponding to the two-dimensional irreducible representations for a tetragonal crystal system, along with example functions for $\chi_{\mathbf{k}}$ (Scalapino 1995). Among these, the $d_{x^2-y^2}$ state has now been shown, as discussed below, to be the best description of the cuprate order parameter. This state was originally predicted on the basis of a phenomenological model of cuprate superconductivity involving the exchange of anti-ferromagnetic (AF) spin fluctuations (Bickers 1989; Moriya 1990; Monthoux 1992) as the interaction responsible for cuprate carrier pairing, but is also predicted by other models (see (Scalapino 1995) and references therein). In the AF spin

Irreducible representation	symmetry name	example $\chi_{\mathbf{k}}$
Γ_1^+	isotropic-s, anisotropic-s	$1, \cos(2\mathbf{2}_{\mathbf{k}}) +,$
Γ_2^+	g-wave	$\sin(2\mathbf{2}_{\mathbf{k}})\cos(2\mathbf{2}_{\mathbf{k}})$
Γ_3^+	$d_{x^2-y^2}$	$\cos(2\mathbf{2}_{\mathbf{k}})$
Γ_4^+	d_{xy}	$\sin(2\mathbf{2}_{\mathbf{k}})$

Table 2.1 Even parity symmetry states and $\chi_{\mathbf{k}}$'s. Adapted from Scalapino (1995).

fluctuation case, the $d_{x^2-y^2}$ state arises because this interaction turns out to be attractive for conduction electrons (or holes) of nearest-neighbor electrons in the a and b directions in the copper oxide planes, but repulsive for the next-nearest-neighbors, which are along the 45° directions. Before the establishment of the $d_{x^2-y^2}$ state, the other leading candidate pairing state was the anisotropic s-wave state, which has essentially the same magnitude dependence as $d_{x^2-y^2}$, but has no sign change and need not go all the way to zero in the 45° directions.

In the orthorhombic system, or in the case of so-called accidental degeneracies in either crystal system, it is possible for the order parameter to be a linear combination of pairing states from different irreducible representations. In the orthorhombic case this turns out to be a real linear combination (see the following chapter), but in general one expects a complex linear combination in order to minimize the total energy of the resulting BCS state by avoiding nodes in the order parameter. There are several theories which have predicted such complex mixture states (Kotliar 1988; Rokhsar 1993; Beasley 1994), but these would require a fully formed quasiparticle gap, which is not consistent with quasiparticle evidence for nodes in the gap (see section 2.3 below). However, it is also possible to get a complex mixture state near a surface

or interface, either of which would break the crystal symmetry, as will be further discussed below and in subsequent chapters.

2.3 Quasiparticle Evidence for the $d_{x^2-y^2}$ Pairing State

Although the specific interaction responsible for high temperature cuprate pairing has still not been established, it has been shown beyond reasonable doubt that the pairing state is unconventional, and in particular is well described by the $d_{x^2-y^2}$ state. The most direct evidence for this comes from various Josephson effect experiments which will be discussed in more detail in chapter 3. However, several other techniques, all of which rely on the relationship between the order parameter and the quasiparticle excitations above the superconducting ground state, also provide complementary evidence.

Among these, some are sensitive to the presence of nodes in the order parameter, such as the temperature dependent specific heat and temperature dependent penetration depth. Here, penetration depth refers to the fact that applied magnetic fields below a critical field are screened out of superconductors by surface supercurrents. The screened field and screening currents decay exponentially into the bulk with characteristic length λ , the penetration depth. However, the penetration depth experiments generally measure the change in λ from its zero temperature limit rather than the absolute value of λ .

In either of these types of measurements, an exponential low-temperature dependence of the measured quantity indicates a gap, $\Delta_{\mathbf{k}}$, with no nodes. This is because for low enough temperatures with a nodeless gap, the quasiparticle excitations are effectively frozen out.

Conversely, if a polynomial low-temperature dependence is found it indicates nodes in the gap, or at least minima small compared to the smallest temperature measured. However, this finding could be consistent with either $d_{x^2-y^2}$ or anisotropic s-wave pairing because the quasiparticle spectrum is not sensitive to a sign change in the order parameter. In the case of the hole-doped cuprates, which include YBCO and the vast majority of the rest, polynomial temperature dependences for these types of experiments have been observed (Hardy 1993; Moler 1994; Schlicter 1994). In the case of electron-doped cuprates, such as $\text{Nd}_{1.85}\text{Ce}_{.15}\text{CuO}_4$, early penetration depth measurements reported an exponential temperature dependence (Wu 1993), but more sensitive recent work (Prozorov 2000) has found a polynomial temperature dependence, thus making it likely that all cuprates have the same order parameter symmetry.

Other quasiparticle-sensitive techniques, such as angle resolved photoemission spectroscopy (ARPES) and tunneling (see next section) are sensitive to the quasiparticle gap in specific directions. In ARPES, the emitted electrons reflect the density of states with respect to energy, $N(E, \mathbf{k})$, and hence the quasiparticle energy gap for momenta in the direction of emission. Figure 2.2 shows a map of the magnitude of the energy gap as a function of direction extracted from ARPES data on BiSrCaCuO (BSCCO). This magnitude follows the $|\cos 2\theta|$ form expected for $d_{x^2-y^2}$, but like the other quasiparticle techniques mentioned above, it cannot detect the sign of the order parameter and hence would also be consistent with anisotropic s-wave. It is interesting to note that the gap measured by ARPES is found to persist to

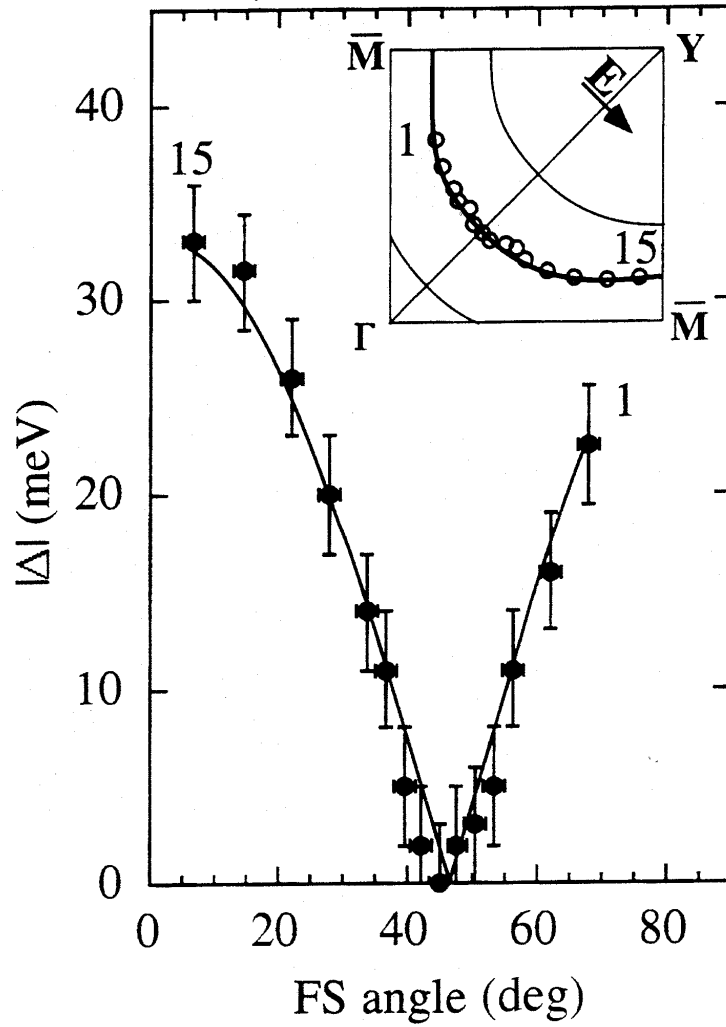


Figure 2.2 Angular dependence of the energy gap of BSCCO obtained by ARPES by Ding (1996). Inset shows directions probed on the Fermi Surface.

temperatures above the T_c of BSCCO, but the possible explanations being actively researched for this fact are beyond the scope of the present thesis.

2.4 Tunneling Experiments and the Possibility of a Secondary Order Parameter

Here we will discuss the tunneling experiments in more detail since unlike the other quasiparticle-sensitive techniques, they can in some cases give information about the phase of the order parameter as well as its magnitude. Furthermore, past tunneling results provide some of the motivation for the experiments in this thesis.

In general, tunneling refers to the quantum mechanical ability of particles, in this case electrons or quasiparticles, to pass through a region in which they are classically forbidden to exist, for example a vacuum in the case of STM or an insulator in the case of a planar tunnel junction. The tunneling current depends on the density of available states in the electrodes, the geometry and height of the barrier, and the applied bias voltage. Specifically, within the so-called semiconductor model of tunneling for superconductors (see for example chapter 3 of (Tinkham 1996)),

$$I = A|T|^2 \int_{-\infty}^{\infty} N_1(E)N_2(E+eV)[f(E)-f(E+eV)]dE$$

where A is a geometry-dependent proportionality constant, T is the tunneling matrix element, N_1 and N_2 are the densities of states on either side of the barrier, V is the applied voltage and f

is the Fermi function. For the case of a normal metal and a superconductor at zero temperature this gives a differential conductance of

$$G_{ns} = \frac{dI}{dV} |_{T=0} = G_{nn} \frac{N_{2s}(e|V|)}{N_2(0)}$$

where $N_2(0)$ is the normal state density of states at the Fermi energy for the superconducting side and G_{nn} is the normal state conductance of the junction. Thus at $T=0$, the differential conductance is directly proportional to the superconducting density of states, N_{2s} . At higher temperatures, G_{ns} is smeared by the Fermi function, as shown schematically in figure 2.3 (a) (Van Harlingen 1995). The symmetry between positive and negative voltage can be understood by considering the physical processes involved for the two bias directions. In the $+V$ case, the electron, which tunnels from the normal metal must have enough energy $eV > \Delta_{\mathbf{k}}$ to occupy one of the quasiparticle states on the superconducting side. In the $-V$ case, the electron, which tunnels into the normal metal comes from a Cooper pair and the eV energy gain, provided $|eV| > \Delta_{\mathbf{k}}$ is used to excite the other electron from the pair into a quasiparticle state which travels in the opposite direction to conserve current.

However, in the case of a tunnel junction involving a cuprate superconductor on one side a conductance characteristic of a fully-formed energy gap, as in figure 2.3 (a) is not observed. Figure 2.3 (b) shows tunneling conductance data for a c-axis oriented planar tunnel junction (Van Harlingen 1995) which effectively samples all \mathbf{k} directions in the a-b plane. Here we see that the quasiparticle energy gap is not fully formed, but rather has rather has finite

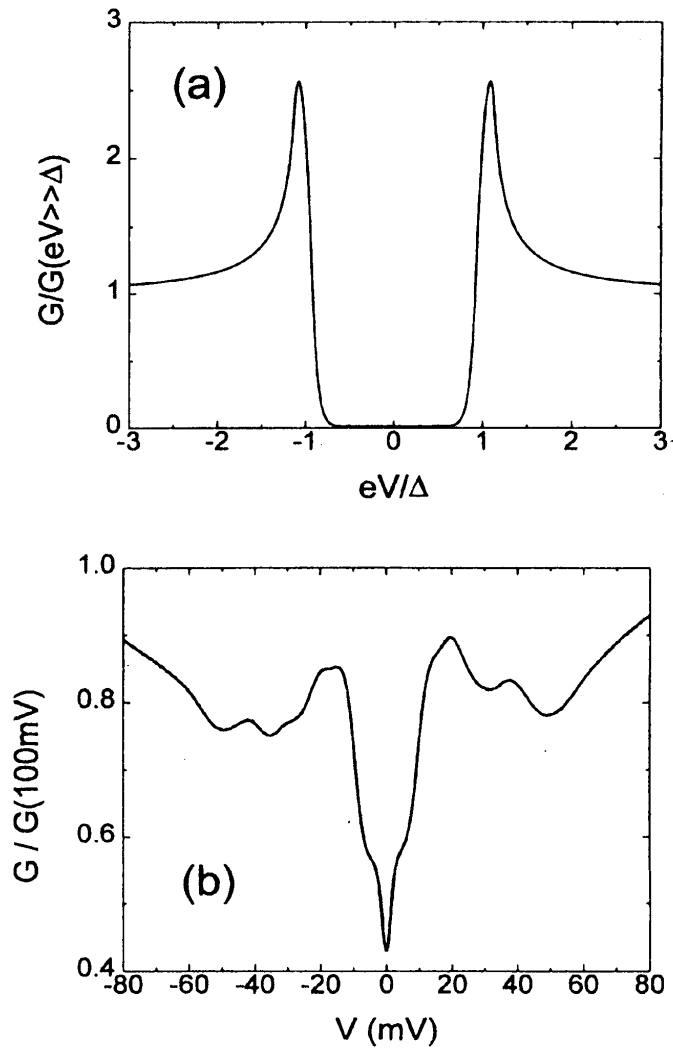


Figure 2.3 Tunneling conductance for (a) ideal NIS junction to fully isotropic s-wave superconductor with thermal smearing and (b) Pb/YBCO c-axis junction with the Pb in its normal state. Adapted from Van Harlingen (1995).

weight for quasiparticles all the way down to zero (relative to the Fermi energy). This is consistent with the results from the other quasiparticle techniques described above.

In the case of a tunnel junction with the tunneling direction along one of the vectors in the a-b plane (for example,(Geerk 1988; Lesueur 1992; Covington 1997a)) another important feature is seen in the tunneling conductance, namely a zero bias conductance peak (ZBCP). While originally explained in terms of spin flip scattering in the barrier, this feature is now believed to be related to the suppression of a $d_{x^2-y^2}$ order parameter near a surface.

The theory for this explanation was first worked out by C-R Hu.(Hu 1994) Qualitatively, this explanation goes as follows. The quasiparticle states near the surface are actually bound states confined by specular reflection off the surface and Andreev reflection a short distance within the superconductor. Andreev reflection is a process where an electron-like quasiparticle of momentum \mathbf{k} , and energy less than $\Delta_{\mathbf{k}}$ is retro-reflected as a hole-like particle with momentum $-\mathbf{k}$, or vice versa. Current is conserved in the Andreev reflection process by a Cooper pair traveling in the bulk to or from the surface. Now, as a consequence of a rigorous theorem, the Atiyah-Potodi-Singer index theorem (Atiyah 1975; Kos 2001), any quasiclassical trajectory which samples a sign change of the order parameter, such as one which reflects off a (110) surface for a $d_{x^2-y^2}$ superconductor must have a zero energy (relative to E_F) quasiparticle bound state solution. It is these bound states, most common for a (110) surface, less so for a surface at a nearby angle or for a rough surface, which cause the ZBCP. When the quasiclassical Eilenberger equations are solved for $d_{x^2-y^2}$ superconductors with such surfaces (Buchholtz 1995), both the zero bias states and a suppression of the $d_{x^2-y^2}$ order

parameter within about 6 coherence lengths of the surface are seen. Finally, when the effects of an applied magnetic field are included in such calculations (Fogelstrom 1997a; b) a linear splitting of the ZBCP from a Doppler shift of the quasiparticle energies for bound states which carry current with or against the Meissner screening currents is found. Such splitting has been observed and was of a magnitude which was better explained by this surface bound state model than by the previous spin flip scattering model, but was not linearly proportional to the field.(Lesueur 1992; Covington 1997a)

However, some of the tunneling results using YBCO/Cu junctions (Covington 1997a; b) have not only a magnetic field splitting of the ZBCP, but also a zero field splitting as the temperature is lowered from 4.2 to 1.4K as shown in figure 2.4. This zero field splitting was not observed in earlier work (Lesueur 1992) mentioned above because Pb, which requires the application of a magnetic field to drive it normal for NIS tunneling was used as the counter electrode. Their explanation (Covington 1997a; b) for this zero field splitting is onset of a low temperature secondary order parameter which pairs quasiparticle states from the ZBCP.

The proposed secondary order parameter might arise from a phonon-mediated interaction as in classical superconductors or from some other mechanism which does not produce a sign change in $\chi(\mathbf{k})$. The effects of such a secondary order parameter were first calculated by Matsumoto and Shiba (Matsumoto 1995). Here, however, we will discuss a simpler physical argument due to Kos (Kos 2001). Based on a first order perturbation calculation applied to each quasiparticle bound state, he derives their energy shift away from zero, resulting in a split of the ZBCP equally above and below zero energy (with respect to E_F).

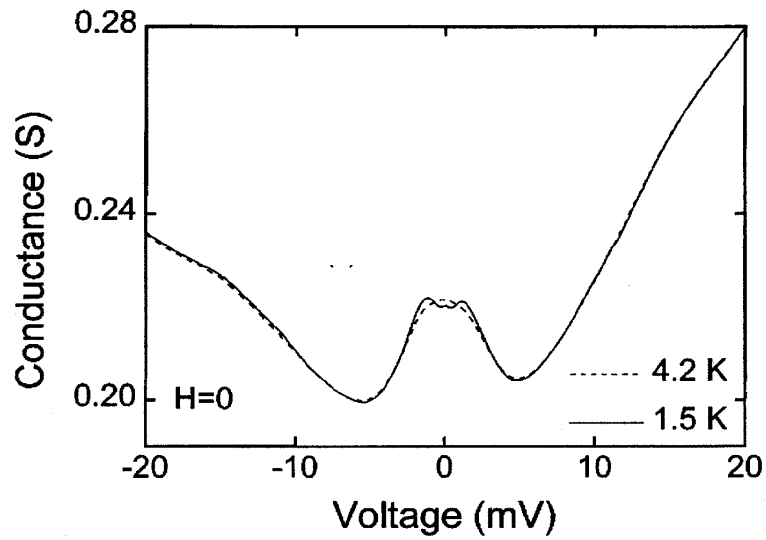


Figure 2.4 Conductance spectrum of YBCO/Cu tunnel junction at 4.2 and 1.5 K from (Covington 1997). Splitting of the ZBCP is seen at 1.5 K.

Also, he calculates a surface current carried by the lowered-energy, occupied bound states. In the case of an applied magnetic field and a secondary order parameter, the ZBCP splitting is predicted (Fogelstrom 1997a) to increase linearly from the zero field splitting until it reaches a saturation value. This is in fact what Covington *et al.* observe.(Covington 1997a)

Chapter 3

JOSEPHSON TUNNELING AS A PROBE OF THE CUPRATE ORDER PARAMETER AND ITS SYMMETRY

Having discussed the superconducting order parameter in general and its possible unconventional symmetries, we now proceed to discuss how the Josephson effect can be used to probe the cuprate order parameter and its symmetries. We first include a brief general background of the Josephson effect. From there, we go on to a description of some of the important past Josephson experiments on the cuprate order parameter. Finally, we present idealized descriptions of the Josephson experiments studied in this thesis.

3.1 Basics of the Josephson Effect

Since Josephson tunneling is the main experimental tool in this work, we begin with a brief theoretical discussion of Josephson tunneling in both conventional and unconventional superconductors. A Josephson junction consists of two superconducting electrodes separated by a barrier. This barrier can be an insulator (SIS junction), a normal metal (SNS junction), or even a constriction between two regions of a superconductor (microbridge junction). All Josephson junctions obey the so-called dc and ac Josephson equations. The dc equation describes the supercurrent density across the junction due to the coherent tunneling of Cooper pairs and is given by

$$J(x,y) = J_c \sin(\phi(x,y))$$

Here J_c is the critical current density, assumed to be in the z-direction, which depends on the materials involved and the geometry of the junction, and $\gamma(x,y)$ is the so-called gauge invariant phase difference between the condensate order parameters of the two superconducting electrodes. In most cases the sinusoidal current phase relation is correct, but in general the current phase relation could be a more complicated periodic function of γ (see section 3.3 below). The ac Josephson equation is

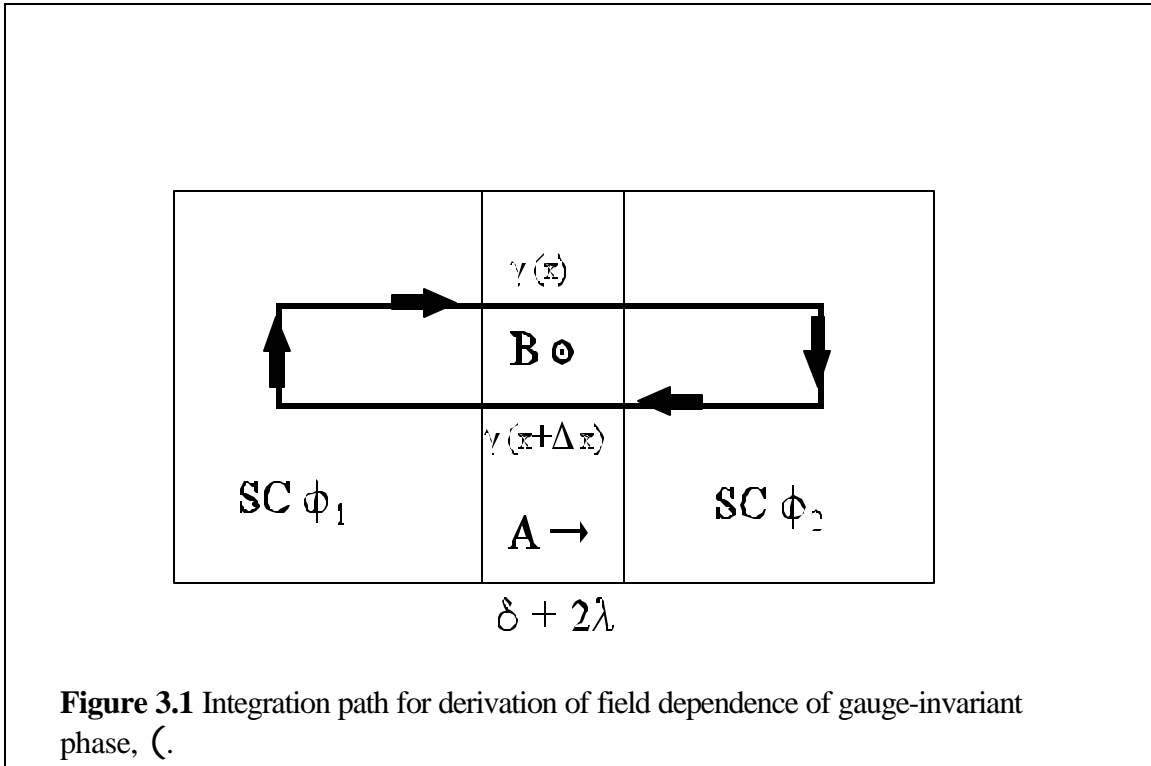
$$d\gamma/dt = 2eV/\hbar$$

which means that the gauge invariant phase difference evolves at a rate proportional to the applied voltage (if any) across the junction. In this thesis we will be concerned with the dc Josephson effect as it will be seen in junctions of various geometries and in superconducting quantum interference devices (SQUIDs), which consist of two Josephson junctions in parallel branches of a superconducting loop.

In most of the experiments in this thesis, it is of primary interest to measure the behavior of the junction or SQUID as a function of applied magnetic field threading the junction or SQUID loop. The dependence of the gauge-invariant phase difference on magnetic field with vector potential A is given by

$$g(x, y) = \Delta\phi - (2\pi / \Phi_0) \int \vec{A} \cdot d\vec{s}$$

where $\Delta\phi$ is the phase difference for the specific gauge corresponding to A , the integral is taken along any path between the two points, (x,y,z_1) and (x,y,z_2) on the two sides of the junction, and $\Phi_0 = hc/2e = 2.0679 \times 10^{-15}$ Wb, is called the flux quantum. Because of this, a difference in γ will be



induced between any two locations x_1, x_2 along the length of the junction. Quantitatively, the difference $\gamma(x_2, y, z) - \gamma(x_1, y, z)$ is found by integrating \mathbf{A} around the closed path shown in figure 3.1 and using

$$\oint \vec{A} \cdot d\vec{s} = \int \vec{B} \cdot d\vec{A} = \Phi$$

and

$$\nabla f = \frac{2e}{\hbar c} \left(\frac{mc}{2e^2} \vec{J}_S + \vec{A} \right)$$

where the contribution of \mathbf{J}_S is zero because the screening current is perpendicular to the path until far past the penetration depth, λ , from the junction. Working this through, we find

$$\mathbf{g}(x_2, y, z) - \mathbf{g}(x_1, y, z) = \frac{2p\Phi}{\Phi_0}.$$

For a junction short enough in width, x , and low enough in Josephson current density, J_c , so that an applied field is not appreciably screened by the Josephson currents, the flux for a uniform applied field H is $M = (x_2 - x_1)H(d + \delta_1 + \delta_2)$. This limit, which will apply to all the junctions in this thesis, is called the short junction limit.

Thus, the variation of γ along the length of a uniform junction with uniform threading flux is linear and the resulting current distribution, $J(x) = J_c \sin(\gamma(x))$, is sinusoidal. The critical current occurs when the sinusoidal pattern, or equivalently the integration constant in the definition of γ , shifts to allow the maximum total supercurrent current for the given field. The critical current assumes a Fraunhofer pattern as a function of applied flux in exact analogy with the optical single slit diffraction pattern. For more general local critical current densities, the critical current as a function of applied flux becomes proportional to the magnitude of the Fourier transform of the critical current density $J_c(x)$ (Barone 1982). This remains true even when we have $d_{x^2-y^2}$ and other more exotic candidate order parameters for which $J_c(x)$ can have sign changes or even a complex phase. In the case of a non-uniform magnetic field, a simple Fourier transform relation between $I_c(H)$ and $J_c(x)$ no longer holds. However, in the experiments of this thesis, we typically have a small but non-uniform constant stray field and a uniform applied field of variable magnitude. In this latter case, the constant field can be accounted for by a phase factor in a new effective $J_c(x)$ to which the Fourier transform calculation can then be applied.

Using a similar argument to that for the single junction, one finds that the case of the SQUID is analogous to the two slit interference problem in optics, giving $I(\Phi) = I_c |\cos(2M\Phi/\Phi_0)|$. Here, M is the flux threading the SQUID loop rather than the individual junctions, which are assumed small compared to the loop area. However, it is important to note that the flux in the SQUID loop comes not only from external fields, but also from the self inductance, L , of the SQUID when there is a net circulating current. Conventionally, the inductance of the SQUID is described by a dimensionless parameter $\beta = 2LI_c/\Phi_0$.

3.2 Directionality of the Josephson Effect

Since we are using SNS Josephson junctions to probe the order parameter of a (predominantly) d-wave superconductor, it is necessary to know how a d-wave superconductor, a normal metal, and s-wave superconductor will couple. A useful treatment of several important aspects of this coupling has been given by Ohashi. (Ohashi 1996) Specifically, using quasi-classical Green function techniques he calculates expressions for the decay of the superconducting pair amplitude into the normal metal from an s-wave superconductor or a pure d-wave superconductor. The pair amplitude $F(k,x)$, is defined in terms of the order parameter $\Delta(k,x)$ and the interaction strength $g(k,x)$ by

$$\Delta(k,x) = g(k,x)F(k,x)$$

Ohashi finds that the pair amplitude decay in normal metal in this case has the form

$$F(k,x) \propto \exp\{-x/(\xi_N \cos(\theta_k))\}, \quad (-90^\circ < \theta_k < 90^\circ)$$

as a function of transport direction, θ_k , away from the interface normal, where x is the distance into the normal metal and ξ_N is an effective decay length, called the normal metal coherence length, which depends on the Fermi velocity and the temperature. In this expression the transport direction in k -space or real space is the same. This exponential form for $F(k,x)$ is the same as what one would expect for the tunneling current in an ordinary tunneling process, but ξ_N , which is typically of order a thousand angstroms, is much longer than typical decay lengths for tunneling. Furthermore, Ohashi finds that s -wave superconductivity can be induced by the proximity effect near a d -wave superconductor unless the interface is at exactly 45 degrees. This is because the angular dependence of the decay distorts the pair potential from the bulk d -wave so that it is no longer an orthogonal function to an s -wave state. However, at a 45 degree interface the plus and minus lobes of the decaying d -wave pair potential will exactly balance, leaving no possibility to couple to an s -wave state from a conventional superconductor, at least not by the usual first order dc Josephson coupling.

3.3 Possible Second Order Josephson Coupling

However, it has been shown in a theory paper by Yukio Tanaka (Tanaka 1994) that it is possible to have second or higher order Josephson coupling between an s -wave and a $d_{x^2-y^2}$ superconductor, and further that for an ideal planar junction interface near the 45 direction of the $d_{x^2-y^2}$ superconductor the second-order coupling would be the dominant contribution. In this paper, Tanaka generalizes an earlier calculation by Furusaki and Tsukada (Furusaki 1991), which accounts for multiple Andreev reflections in the Josephson barrier, to the case of d -

wave/s-wave junction. He obtains an expansion for the Josephson supercurrent as a function of junction phase difference,

$$I(\mathbf{g}) = \frac{e}{p\hbar} \int_0^{p/2} d\mathbf{q} \int_{-p}^p d\mathbf{f} \frac{\Delta_s \Delta_d(\mathbf{q}, \mathbf{f}) f(\mathbf{q}, \mathbf{f}) \sin \mathbf{g}}{G(Z, T, \mathbf{q}, \mathbf{f})} \sum_{n=0}^{\infty} \left[\frac{\Delta_s \Delta_d(\mathbf{q}, \mathbf{f}) f(\mathbf{q}, \mathbf{f}) \cos \mathbf{g}}{G(Z, T, \mathbf{q}, \mathbf{f})} \right]^n$$

where $\mathbf{2}$ and \mathbf{N} are spherical coordinates, \mathbf{g} is the gauge-invariant phase, $f(\mathbf{2}, \mathbf{N})$ is called the tunneling form factor, which accounts for the directionality of the Josephson effect and G is a function which depends on the barrier strength, Z , temperature, T , and $\mathbf{2}$ and \mathbf{N} . For an ideal planar 45° junction, the \mathbf{N} integral of the $n = 0$ term, as well as all even n terms is zero, but the odd n terms are not zero. Thus for this junction orientation, $I(\mathbf{g}) \propto \sin \mathbf{g} \cos \mathbf{g} \propto \sin 2\mathbf{g}$. The temperature dependences for $Z = 1.0$ and 5.0 that (Tanaka 1994) calculated of the maximum of $I(\mathbf{g})$ for both the 45° case and the 0° case, which has an approximately $\sin \mathbf{g}$ phase dependence, are plotted in figure 3.2. Clearly the 45° junction depends more sensitively on Z and has a more gradually temperature dependence than the 0° case.

3.4 Relevant Past Josephson Experiments on the Cuprates

3.4.1 Single Crystal Corner Junctions and SQUIDS

The earliest successful attempt to use the directionality and phase sensitivity of the Josephson effect to probe the order parameter of the cuprates (Wollman 1993) was a SQUID formed by a Pb/Au bilayer evaporated onto the perpendicular faces of a YBCO single crystal. However, we will first discuss a similar single crystal Josephson experiment where a

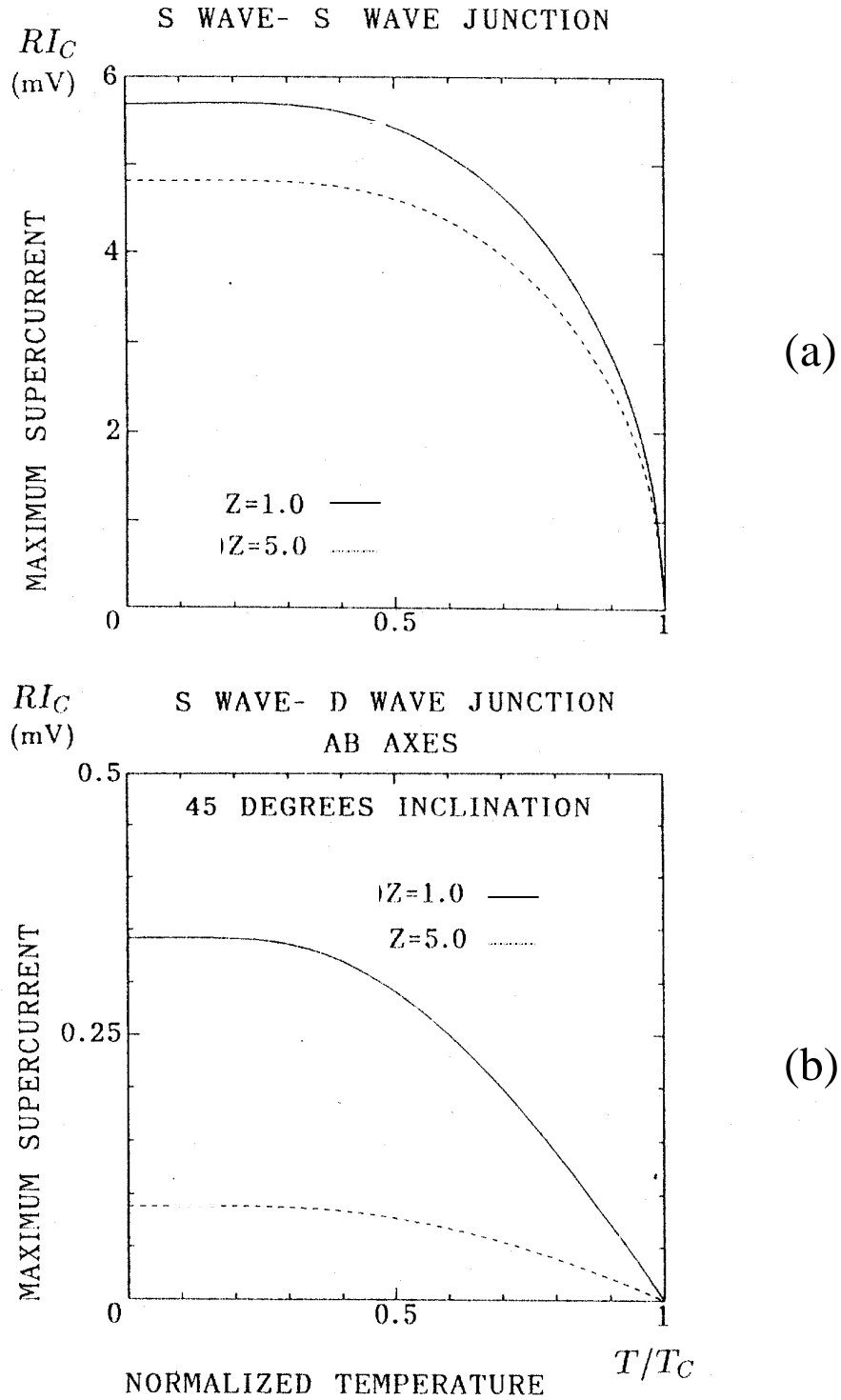


Figure 3.2 Temperature dependence of maximum supercurrent for all s-wave junction and 45° s-d junction with barrier strength $Z = 1.0$ and 5.0 from (Tanaka 1994). T_c is for the s-wave superconductor which is taken to have the lower T_c . The temperature dependence of a 0/ s-d junction is similar to the all s-wave junction.

single Josephson junction was formed around a 90 degree corner (Wollman 1995) because the data analysis of this latter case is more direct. Since this experiment is the direct predecessor to the experiments of this thesis, this discussion will be more detailed than that for the other background order parameter experiments we cover. A schematic of this experiment is shown in figure 3.3.

To distinguish between the leading candidate states of $d_{x^2-y^2}$ and anisotropic s-wave, the authors measured the critical current of the junction as a function of applied magnetic field. For a uniform current density, $J_c(x)$, and an anisotropic s-wave order parameter, the predicted $I_c(H)$ is just the Fraunhofer pattern, $|I_{cmax} \sin(BM/M_0)/(BM/M_0)|$, as discussed above in section 3.1. However, in the d-wave case, the current density has opposite signs for the two perpendicular faces. This is because the Josephson coupling between the Pb and the YBCO on the two faces involves k-states which correspond to opposite-signed lobes in the $d_{x^2-y^2}$ order parameter, $J_k(\cos(k_x) - \cos(k_y))$. The ideal signature of $I_c(H)$ for $d_{x^2-y^2}$ can be calculated by assuming equal lengths and $|J_c|$ for the two faces using the Fourier transform to get

$$I_c(H) = |I_{cmax} \sin^2(BM/2M_0)/(BM/2M_0)|.$$

This function is zero at $H=0$ and has maxima and minima at twice the period of the simple Fraunhofer case. The ideal predictions for both d-wave and anisotropic s-wave are also shown in figure 3.3.

However, there are a number of potentially complicating issues which might cause the corner junction results to differ from the ideal predictions of figure 3.3. To begin with, we consider the orthorhombicity of YBCO and its proclivity to form twin domains. First, if the

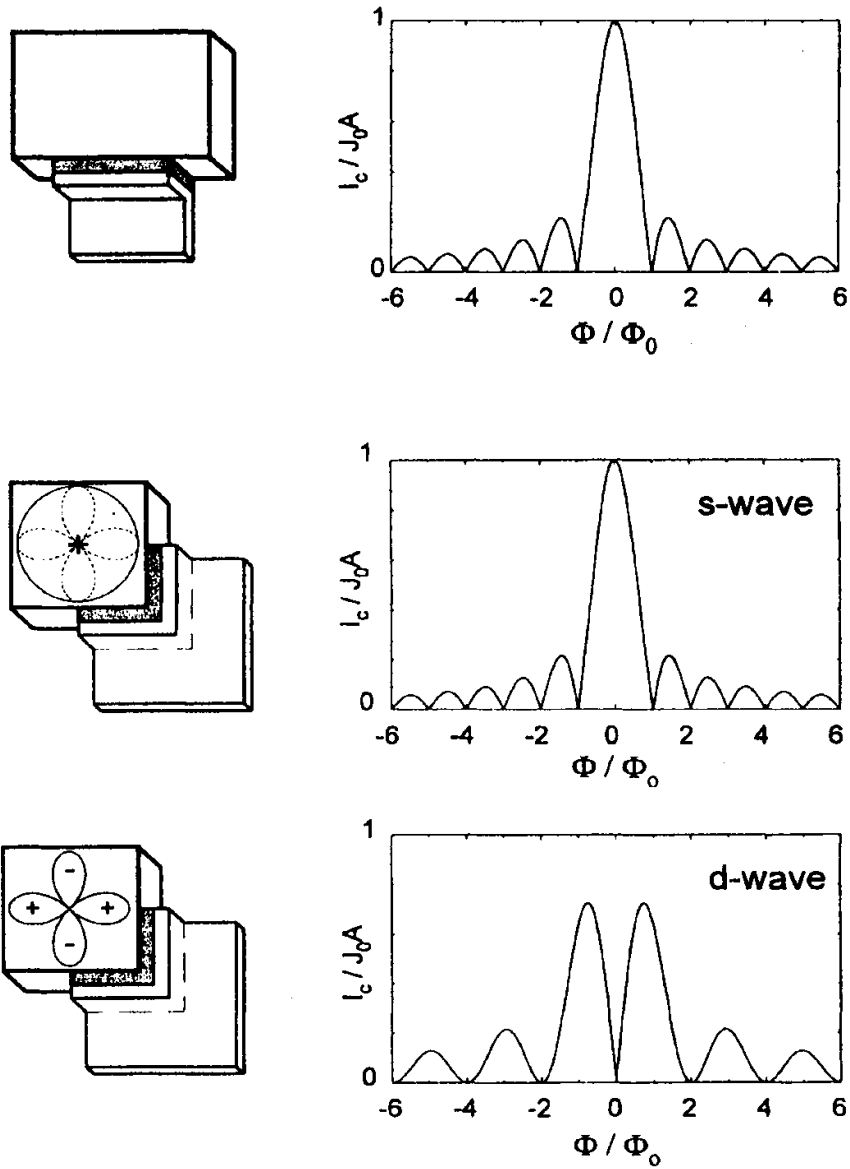


Figure 3.3 Schematics and ideal $I_c(M)$ diffraction patterns from the single-crystal junction experiment of (Wollman 1995). Top is an edge junction control case; middle is a corner junction for anisotropic s-wave; and bottom is a corner junction for $d_{x^2-y^2}$.

order parameter were to invert its sign across a twin boundary that happened to separate the two perpendicular faces of the junction, this might remove the sign change in the critical current density, resulting in the ordinary Fraunhofer signature of anisotropic s-wave instead of the $d_{x^2-y^2}$ signature. However, the energetics of such a domain wall formation at a twin boundary turn out to be unfavorable (Wollman 1996). Secondly, for the case of a single twin domain, the orthorhombicity could cause the magnitude of the order parameter to differ in the a and b directions due to a small admixture of s-wave in the dominant $d_{x^2-y^2}$. This would lead to an incomplete cancellation of the critical current at $H=0$. A similar incomplete cancellation could also be caused by different coupling strengths along the two faces of the junction or by unequal junction lengths. See figure 3.8 below for an example of this incomplete cancellation in the context of the arbitrary-angle corner junction experiment of the present thesis.

Another possible deviation from the prediction of figure 3.3 would occur in the case where the order parameter sampled was actually a complex mixture such as the YBCO d+is state discussed in section 2.3. ($d_{x^2-y^2} + id_{xy}$ would not alter the $I_c(H)$ because the id_{xy} component makes zero contribution in the a and b directions probed in this corner junction experiment.) In this case Fourier transforming the complex effective critical current density gives

$$I_c(\Phi) = J_0 A \sqrt{\frac{[1 - \cos(\mathbf{p}\Phi / \Phi_0)][1 - \cos(\mathbf{p}\Phi / \Phi_0) - \mathbf{p}\mathbf{e}]}{\mathbf{p}(\Phi / \Phi_0)}}$$

where the order parameter is taken to be $(1 - \delta)d + i\delta s$. For $\delta \dots 0$ or 1 , this I_c breaks symmetry between $\pm M$.

Lastly, we consider the possibility that $I_c(H)$ for any given order parameter may be distorted by stray magnetic field due to poor shielding of the apparatus, or, more likely, to the trapping of flux vortices in the component superconductors near the junction. Like the case of a complex order parameter, flux trapping fields threading through the junction will cause the symmetry of $I_c(H)$ about $H=0$ to be broken. Since the stray field H_{trapped} is constant and independent of H_{applied} its effect on $I_c(H_{\text{applied}})$ can be calculated by Fourier transforming using an equivalent phase factor as discussed in section 3.1 $I_c(H_{\text{applied}})$ for the relatively simple case of $M_0/2$ of magnetic flux in a gaussian distribution of $1/10$ of the total junction length at various locations along the junction length is shown in figure 3.4 for both a s-wave and a $d_{x^2-y^2}$ order parameter. While such an H_{trapped} located right at the corner can change the zero at $H=0$ of the d-wave pattern to a maximum or the maximum at $H=0$ of the s-wave pattern to a minimum, it still causes noticeable asymmetry about $H=0$ in the side peaks. ($M_0/2$ of flux with width zero right at the corner would actually switch the s-wave and d-wave patterns exactly into each other, but this need not concern us because flux threading with zero width would be unphysical.)

Thus, an $I_c(H)$ pattern which is symmetric about $H=0$ and agrees with the d-wave or the s-wave prediction is a clear indication of the corresponding order parameter symmetry. On the other hand, an asymmetric $I_c(H)$ can in principle indicate either a complex order parameter or the presence of trapped flux. Fortunately, these last two cases can be distinguished by repeatedly heating above the T_c of the component superconductors and re-cooling because flux trapping need not occur, or at least need not occur in the same locations on re-cooling, while a complex order parameter would re-appear on each re-cooling.

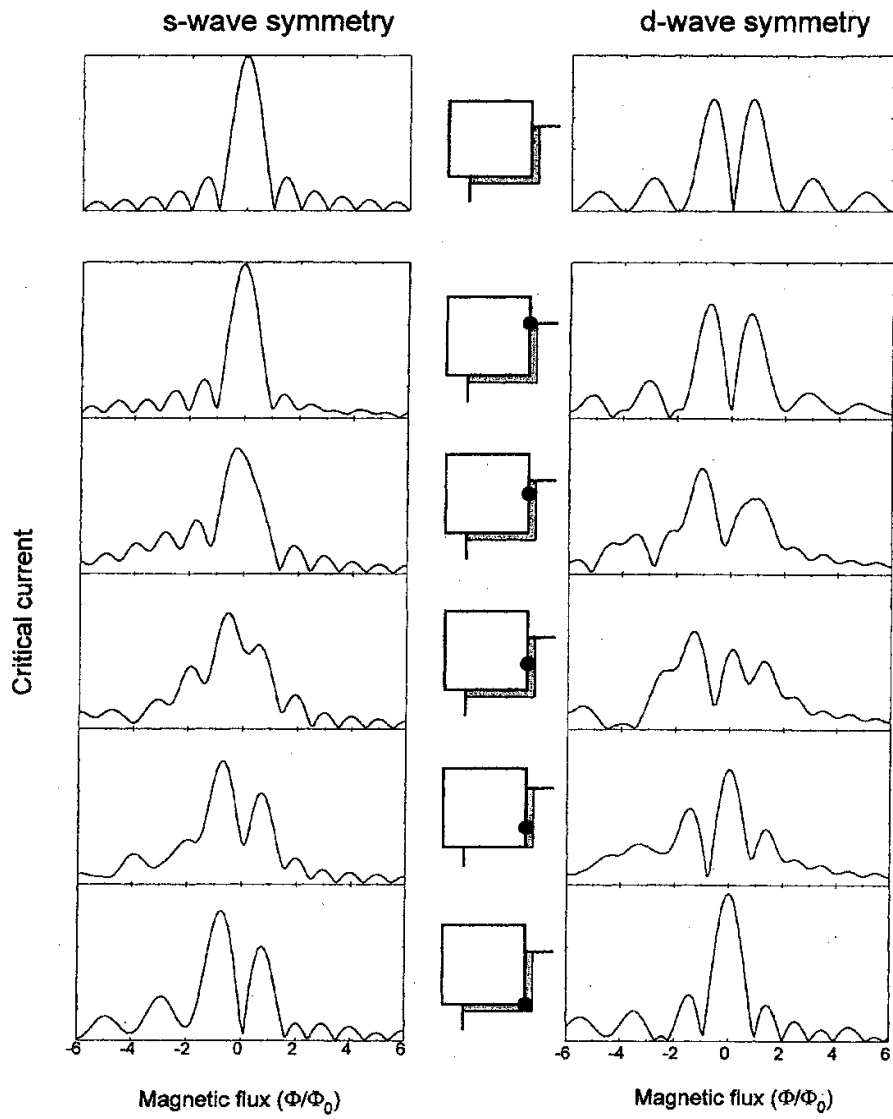


Figure 3.4 Effect on $I_c(M)$ of one half flux quantum of trapped flux threading a corner junction at the locations shown. Adapted from (Van Harlingen 1995).

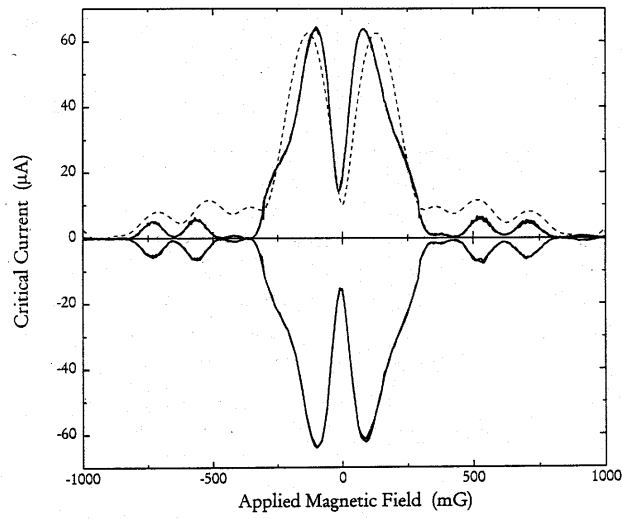
The actual $I_c(H)$ data for a typical single-crystal corner junction is shown in figure 3.5 (a). The data exhibit a pronounced minimum at $H=0$, although not all the way to $I_c = 0$, major peaks on either side of zero, and smaller evenly shaped minor peaks further out. A reasonable fit to the data can be made by assuming a 15% asymmetry in critical current between the two faces. The difference of the fit from the actual magnitude of the side peaks are explained by non-uniformities in the critical current density. The slight asymmetry between the plus and minus sides of $I_c(H)$ is due to residual stray field as can be seen by comparing to figure 3.5 (b) for a different cooldown where flux trapping occurred.

The overall conclusion of this single crystal junction experiment is that the $I_c(H)$ signature indicates a sign change in the order parameter between the a and b directions. Hence, the single crystal corner junction experiment supports a $d_{x^2-y^2}$ order parameter.

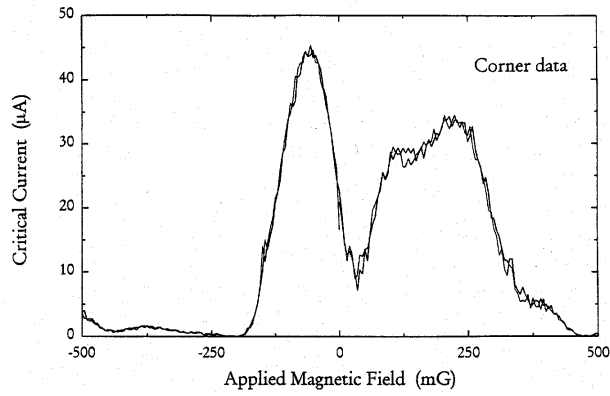
The same conclusion for a sign change in the order parameter between the a and b directions was also reached in the single crystal SQUID experiment (Wollman 1993). Under ideal circumstances the SQUID modulation $I_c(H)$ is given by

$$I_c(M) = I_c |\cos(\phi + 2BM/M_0)|$$

as discussed in section 3.1 and where ϕ is an additional phase term to account for the order parameter symmetry. ϕ is 0 for s-wave and π for $d_{x^2-y^2}$. Thus analogously to the single junction case, a minimum at $H = 0$ corresponds to $d_{x^2-y^2}$ and a maximum to s-wave. However, the SQUIDs in these single crystal experiments had much smaller modulation depths due both the asymmetry between the two SQUID junctions and to inductance effects, which we will



(a)



(b)

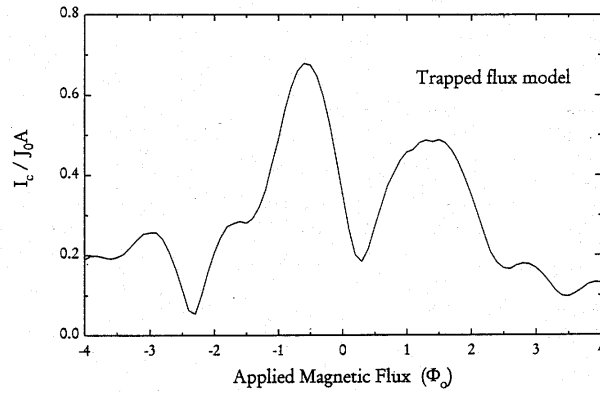


Figure 3.5 (a) Typical corner junction $I_c(M)$ diffraction pattern from (Wollman 1995) showing both polarities of I_c . (b) Corner junction diffraction pattern data and model for a run from (Wollman 1995) with flux trapping.

discuss in more detail below in conjunction with the variable inductance SQUID experiment of this thesis.

The effect of the asymmetry in SQUID junction critical currents is obviously a proportional reduction of the modulation depth of $I_c(H)$ by the factor $\eta = |I_1 - I_2|/(I_1 + I_2)$, while the effect of the self-inductance of the SQUID loop is more subtle. This is because the self-flux alters the phase equation around the loop. It turns out that for large values of the inductance parameter $\Phi = 2LI_c/M_0$, the modulation depth is proportional to $1/\Phi$ (Ouboter 1970)(Orlando 1991).

To increase their sensitivity in the face of small modulation depth, as well as to account for the additional shifting of the SQUID $I_c(H)$ pattern due to asymmetry and inductance effects, the authors (Wollman 1993) resorted to a technique of measuring the dynamic resistance dV/dI at several bias currents I . Typical data from this procedure are reproduced in figure 3.6, where the shifting of the pattern by self flux for different bias currents can be seen. Note that in the absence of additional pattern shifting from inductance and asymmetry, dV/dI will have the opposite signature from $I_c(H)$, namely $d_{x^2-y^2}$ will have a maximum in dV/dI at zero and a minimum at \mathbf{B} and vice versa for s-wave. It has been shown (Rzchowski 1997) that for the parameters of the SQUIDs used by these authors, the intrinsic phase of the SQUID $I_c(H)$ pattern can be found by linear extrapolation to zero bias current. The results of the extrapolation for the corner SQUIDs show that the minima of dV/dI , which correspond to maximum of $I_c(H)$ are clustered around \mathbf{B} as expected for $d_{x^2-y^2}$. For the control case of edge

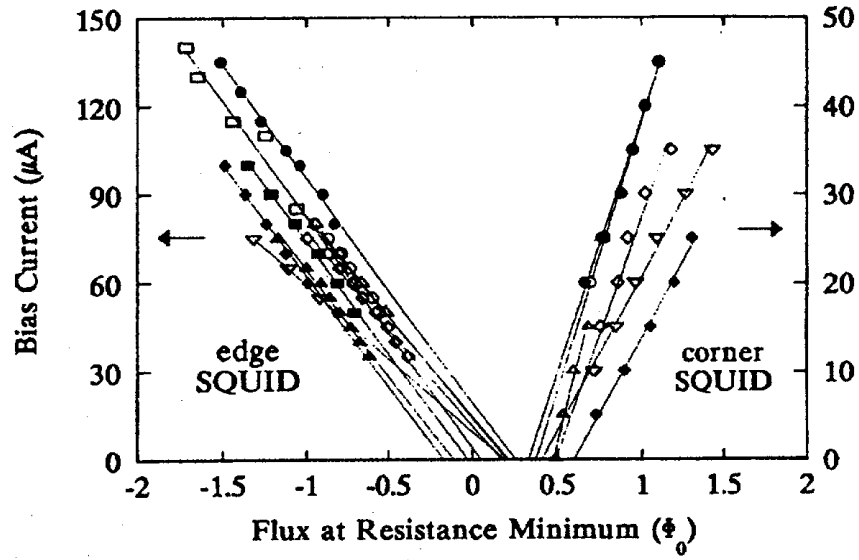
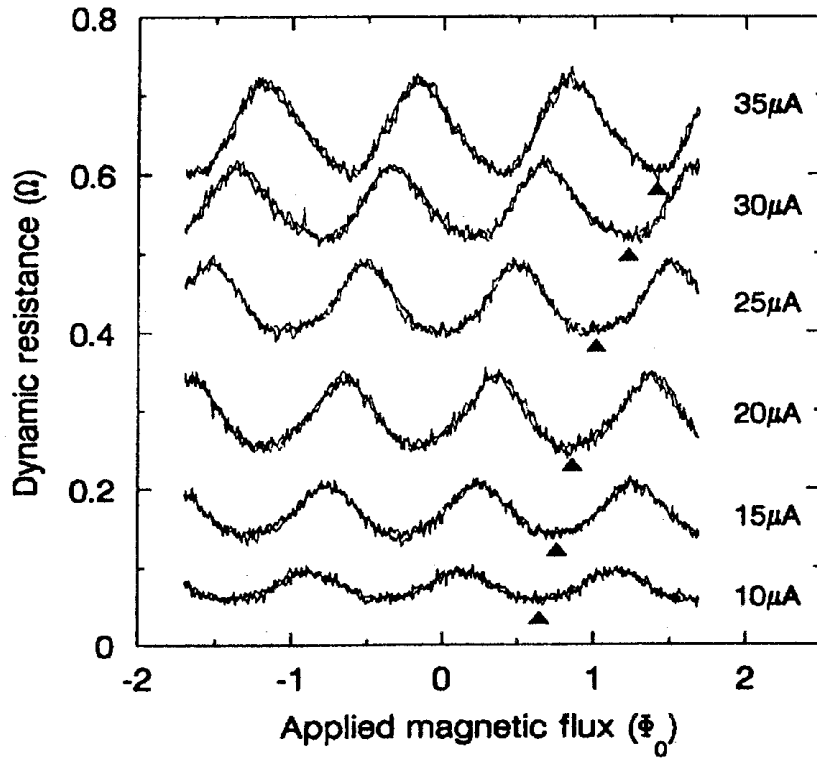


Figure 3.6 From (Wollman 1993). Top: modulation pattern of corner SQUID sample for different bias currents. Bottom: extrapolation to zero bias current for several edge and corner SQUIDs showing intrinsic phase shift for the corner junctions.

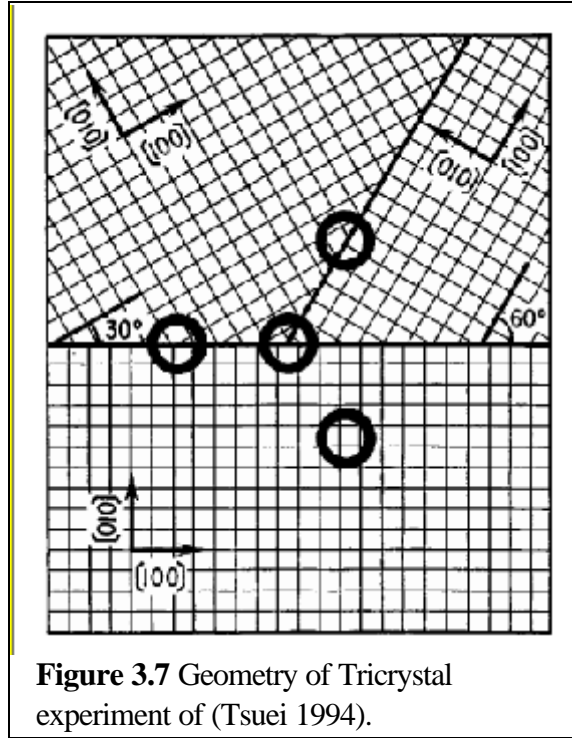
SQUIDs, the minima in dV/dI clustered around zero, as expected for an edge SQUID with either d-wave or s-wave order parameter symmetry.

The difference from \mathbf{B} or zero respectively is attributable to different amounts of trapped flux threading through the SQUID loops on different runs. Trapped flux is a more difficult problem in the SQUID experiment than in the single junction experiment because it results only a shift of an otherwise uniform modulation pattern and hence is indistinguishable from the shift of the modulation pattern due to the cuprate order parameter. However, since the spread of the interpolated minima is less than \mathbf{B} , the data of this experiment is still sufficient to distinguish $d_{x^2-y^2}$ from s-wave.

3.4.2 SSM Experiments on Tri-crystal Thin Films

A different approach to measuring the phase of the order parameter involving scanning SQUID microscopy (SSM) of a thin film ring of YBCO (or other cuprates) deposited on tri-crystal SrTiO_3 substrates has been developed by Kirtley and Tsuei (Tsuei 1994). This experiment depends on the fact that for a short coherence length superconductor, like the cuprates, a grain boundary, across which the order parameter has a different orientation is sufficient to form a Josephson junction. Grain boundary junctions of this sort occur when a thin film of YBCO (or other cuprate) is grown on a substrate consisting of pieces, each with a different desired template orientation, fused together. In this case three pieces are used to form a tri-crystal.

The distinguishing signature for a $d_{x^2-y^2}$ order parameter in this experiment occurs when the three crystal orientations are chosen such that each of the three junctions in a ring samples



opposite signs of the $d_{x^2-y^2}$ order parameter on either side. The crystal directions used by Kirtley and Tsuei to achieve this are shown schematically in figure 3.7(a). The phase constraint for the tri-crystal ring geometry is given by

$$\Phi_{ext} + I_s L + \frac{\Phi_0}{2p} \sum_{jcts} \Delta \mathbf{j}_i = n \Phi_0$$

which is similar to a SQUID equation except with three junctions (Tsuei 1994). Here I_s is the circulating supercurrent and the sum of phase differences is taken over all junctions in the ring. This constraint can be satisfied by having one of the junctions phase equal to \mathbf{B} , as occurs in the low Φ limit, by having a circulating current which generates $\pm M_0/2$ of flux in the ring, as happens in the high Φ limit, or some combination in between. Other $1/2$ -integer multiples of M_0 are also

possible when the sample is cooled down in an applied field. On the other hand, for an s-wave order parameter or for either order parameter in a ring with only two junctions, there need not be any phase drop across any of the junctions and the flux in the ring will be zero or an integer multiple of M_0 .

To determine the amount of spontaneous flux in the 3-junction ring, as well as the 2-junction control ring, the SSM is used. Without going into detail, we note that an SSM is an instrument which produces a 2D image of the magnetic field of a sample by mechanically scanning a SQUID and associated circuitry relative to the sample. Exploiting the SQUID's sensitivity to fluxes less than or of order the flux quantum and using feedback techniques, an SSM can achieve a typical field resolution of 10^{-10} T, flux resolution of $10^{-5}M_0$ and a typical spatial resolution of a few microns (Van Harlingen, Private Communication). Integration of the calibrated flux in each ring from their SSM images showed $M_0/2$ in the 3-junction ring and 0 or M_0 in the 2-junctions rings. The SSM images also doubled as a check for flux trapping, since any trapped flux would be easily seen in the image of the superconducting thin film pattern.

Several other cuprate materials have been investigated by the same technique, namely, Tl 2201 (Tsuei 1996), BSCCO 2212 (Kirtley 1996), and more recently the electron-doped materials NCCO and PCCO (Tsuei 2000). The tri-crystal technique is particularly well suited for testing a variety of cuprates, once they are successfully grown as thin films, since the grain boundaries virtually guarantee successful Josephson junctions without having to solve the additional materials problems of making superconducting contact with a second or third material as in the corner junction and SQUID techniques. All of the materials tried in the tri-crystal

experiment have show $\frac{1}{2}$ integer flux quantization and hence have been found consistent with $d_{x^2-y^2}$ pairing.

3.4.3 SSM Experiments on Pb/YBCO Thin Film SQUIDs

The third (and final) Josephson-based order parameter measurement that we will consider in this section also involves the use of a scanning SQUID microscope (SSM). In these experiments (Mathai 1995; Gim 1996), thin film Pb/Ag/YBCO SQUIDs were fabricated with one of the SQUID junctions at zero degrees and the other at another chosen angle. Each such SQUID was then cooled and scanned in an SSM to check for the absence of flux trapping (and heated and re-cooled as necessary: see 3.4.1 above). The SQUID sensor from the SSM was then positioned over the center of the Pb/Ag/YBCO SQUID under test and the resultant magnetic field (applied + that from the circulating current of the SQUID under test) was measured as a function of applied field.

The result turns out to be a series of lines, each of which represents the diamagnetic response of the YBCO/Ag/Pb SQUID to the applied field for a different number of flux quanta in the SQUID under test. By mapping a time reversed data set (with all currents and fields reversed, including those of the control circuitry of the SSM) onto the original, they find excellent overlap for both 0-0 and 0-90 geometries. Furthermore, by noting whether there is a particular line which maps to itself, which would correspond to zero flux in the SQUID under test at zero applied field, they can determine whether there is an intrinsic phase difference between the two junctions. If no line maps to itself, even though the overall pattern does, then there is a \mathbf{B} phase shift between the two junctions. As expected for a $d_{x^2-y^2}$ order parameter,

the 0-0 SQUID has a line which maps to itself, but the 0-90 corner SQUID does not.

Combing this fact with an analysis of the uncertainty of the overall time reversal symmetry for the three such samples of (Mathai 1995), they find that the phase change for the 90 degree corner is $\phi_d = (0.90 \pm 0.05)\pi$.

SQUIDs with junction angles other than 0-0 or 0-90 are presented in (Gim 1996) Here the SQUIDs turned out to have much smaller ϕ 's than in (Mathai 1995), so that the data had to be analyzed differently. In the low ϕ regime, one expects zero current at zero applied field independent of whether the order parameter symmetry is s-wave or d-wave (as will be further discussed in the context of the variable inductance SQUID experiment of this thesis in the next section.) However, the behavior slightly away from zero applied field is paramagnetic for a $\phi \neq 0$ shift between the two junctions of the SQUID under test, but diamagnetic for a zero shift. The results of 11 such working SQUIDs at various angles generally agree with the angular dependence of the phase for a $d_{x^2-y^2}$, but four of their working SQUIDs had the opposite phase change to that expected for their orientation. The authors attribute these discrepancies to either misalignment of the pattern or to surface roughness, either of which could change the true angle being measured. When they tested the working SQUIDs in this paper for time reversal symmetry by reversing all fields and currents, they found good but not perfect time reversal symmetry. Quantitatively, they concluded that the phase shifts of all their working Pb/Ag/YBCO were within 0.2π of 0 or π , but were distributed randomly within this range. They attributed this to drift of the background field, but could not rule out a small ($\approx 2\%$) complex component of the order parameter.

3.5 Idealized Descriptions of the Experiments in this Thesis

Having discussed the past experiments that motivated the present work, we now describe the specific experiments of this thesis. As noted above, these experiments are intended both to provide confirmation of the $d_{x^2-y^2}$ order parameter and to search for small deviations from $d_{x^2-y^2}$ such as the onset of a secondary order parameter near a (110) surface. The descriptions that follow are idealized, in that the effect of such things as surface roughness and non-uniform Josephson contact are neglected. However, when we turn to the data in chapter 5, we shall see that such non-idealities play an important role in the analysis.

3.5.1 Corner Junctions

The first geometry we will consider are single junctions spanning an arbitrary angle with equal junction length on either side of the corner. For a 0 or 90 degree angle, this will constitute a repeat in thin films of the single-crystal edge and corner junctions discussed above in section 3.4.1. For other angles, these junctions effectively combine the phase and direction sensitivity of (Gim 1996) with magnitude information.

Figure 3.8 shows the predicted $I_c(H)$ for corner junctions with one face at 0 degrees and the other at 0, 30, 45, 60, 75, and 90 degrees respectively, assuming a $d_{x^2-y^2}$ order parameter. The 0/ case is the ideal Fraunhofer pattern for a uniform edge junction, $|I_{\text{cmax}} \sin(BM/M_0)/(BM/M_0)|$, while the 90/ pattern is $|I_{\text{cmax}} \sin^2(BM/2M_0)/(BM/2M_0)|$ as seen above in section 3.4.1. The other angles are a progression between these two cases with the 30/ case showing a doublet structure to the side lobes, the 45/ case being equivalent to

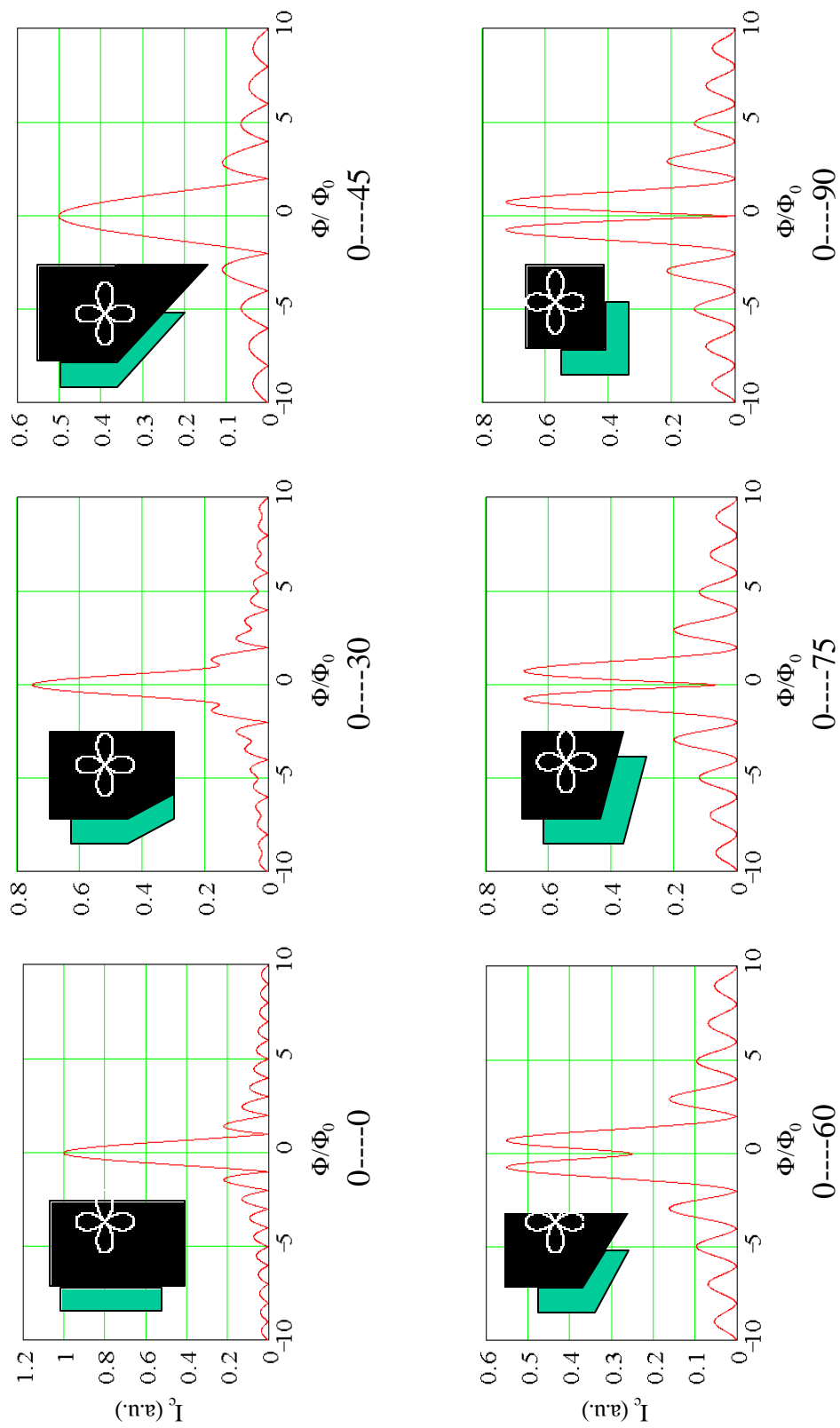


Figure 3.8 Ideal $I_c(M)$ predictions for 0,30,45,60,75 and 90 degree corner junctions.

an edge junction with half the length and hence twice the period in $I_c(H)$, and the 60/ and 75/ cases showing a local minimum at $H = 0$. If the order parameter were anisotropic s-wave, The 0/ and 90/ corner junction patterns would look identical, as would the 30/ and 60/ corner junction patterns. Of course a result consistent with $d_{x^2-y^2}$ will not be surprising, but it will at least indicate that the phase and direction sensitivity of these experiments is at least as good as those of past experiments in spite of what ever non-uniformities may exist.

For corners with one face near 45 degrees, this experiment also has the potential to detect the onset of the predicted secondary order parameter. Fig 3.9 show the expected change in the $I_c(H)$ for the, 45/ corner junction when an α_z is component grows from $\alpha_z = 0$ to 0.2 to 1.0 for the 45 / surface. For $\alpha_z = 0.2$, the central peak shifts slightly and acquires a shoulder, while the side lobes acquire a slight distortion. At $\alpha_z = 1.0$, the shoulder on the central peak becomes a separate peak, while each side lobe becomes a doublet.

3.5.2 Arbitrary Angle Single Edge Junctions

A schematic of the layout for two versions of this class of junction geometries is shown in figure 3.10. the first case (figure 3.10(a)) has junctions spaced every 7.5 degrees around a semi-circle, while the second case (figure 3.10(b)) has junctions in straight planes spaced every 2 degrees from 35 to 55 and 235 to 245 degrees plus junctions at 0, 90 and 180 degrees.

Ideally, the junctions sample only a small range of angles given by the acceptance cone for the straight plane junctions, or its convolution with a small arc of 4.6 degrees for the junctions on the semi-circular surface. However, as we shall see in chapter five,

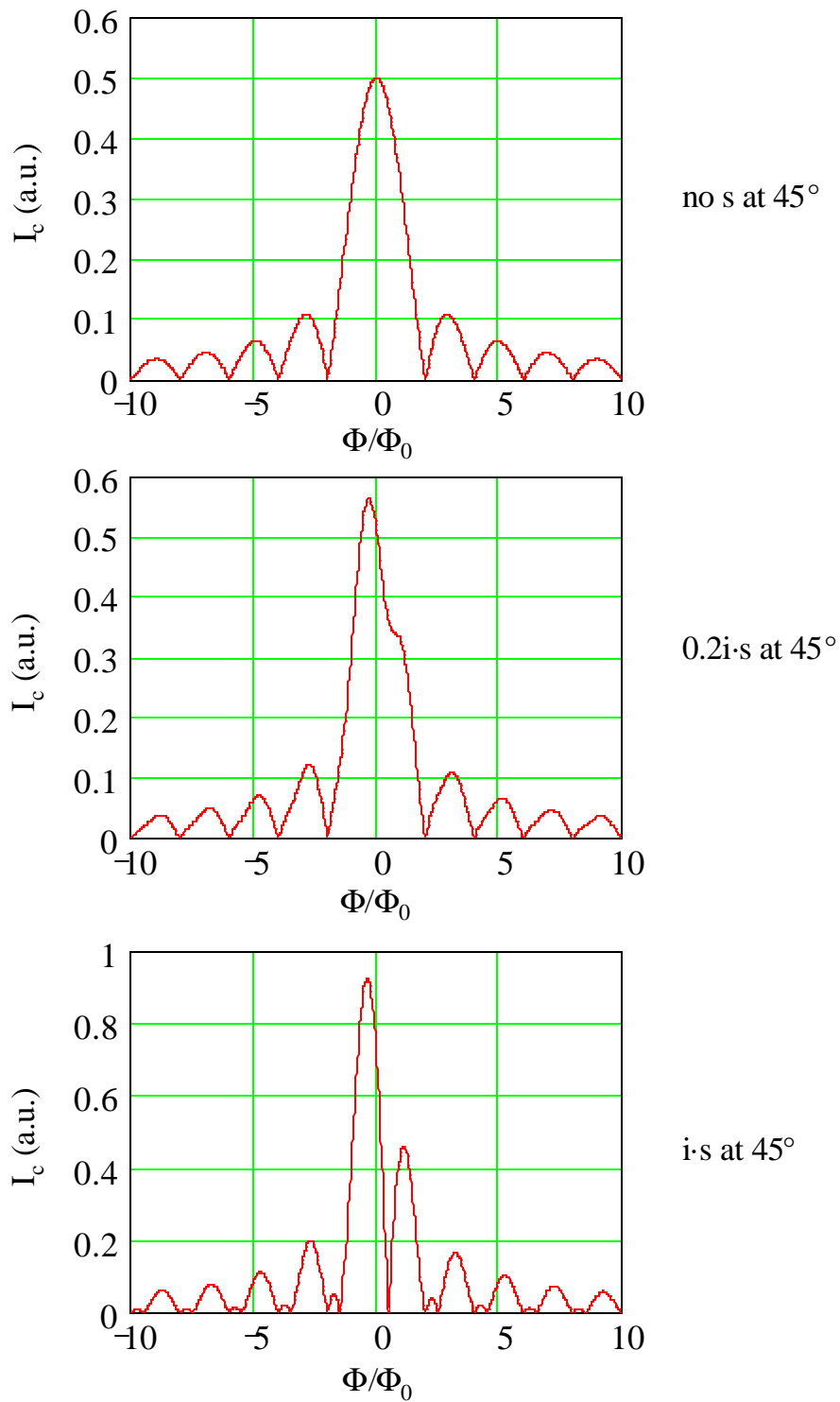


Figure 3.9 Effect of complex s-wave order parameter component at 45 degree surface of 45 degree corner junction.

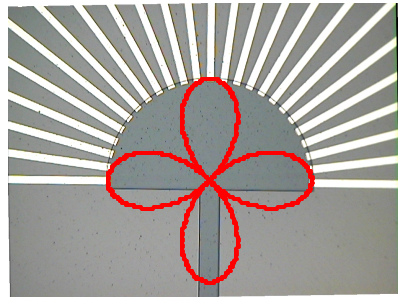
surface roughness will cause more directions to be sampled. This will complicate the analysis, but still leave the data interpretable. Here, for simplicity, we will confine ourselves to an idealized description and simulation, as noted above.

The purpose of these single junction experiments is two-fold: first, to map out the Josephson coupling to the YBCO order parameter over the full range of angles; and second, to look for surface effects in junctions near 45 degrees such as a possible secondary order parameter onset.

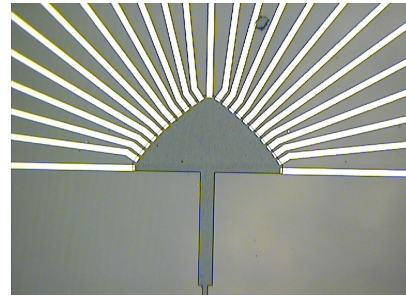
Figure 3.11(a), shows the expected current density $J_c(x)$ and Josephson diffraction pattern $I_c(H)$ for a 45 degree junction with a curved interface going from 42.7 to 47.3. degrees and assuming an ideal $d_{x^2-y^2}$ order parameter on the YBCO side. Figure 3.11(b) shows the effect of admixing a fraction of s-wave secondary order parameter near the YBCO surface. Thus the primary signature of a secondary order parameter onset for this experiment is the dramatic rise of the zero-field value in the $I_c(H)$ diffraction pattern, starting from zero above the onset temperature. Of course in the simpler case of a perfectly straight 45 degree junctions, one would expect $I_c(H)$ to be zero for all H without a secondary order parameter and to be an ideal Fraunhofer shape after the onset of a secondary order parameter.

3.5.3 Variable-inductance SQUIDS

The last and most novel of our experimental geometries is the variable inductance SQUID, shown schematically in figure 3.12. A conceptual description of this experiment has been previously published (Van Harlingen 1999). Unfortunately, the variable inductance experiment was not completed, but some preliminary results will be presented in section 5.2.



(a)



(b)

Figure 3.10 Optical micrographs of spider experiments. (a) Junctions every 7.5° . (b) Junctions at 0° , 90° , 180° , and every 2° between 35° and 55° and between 125° and 145° . An ideal d-wave clover leaf is shown in (a) for reference.

Like the tri-crystal experiments, this experiment measures the spontaneous flux generated when the two SQUID junctions probe different directions of the $d_{x^2-y^2}$ order parameter, but unlike the tri-crystal case, a fixed pickup coil and measurement SQUID is employed, rather than an SSM. The inductance of the SQUID under test is varied by moving a superconducting shield over the length of the long narrow SQUID loop, and the change in spontaneous flux as a function of this varying inductance is recorded. Figure 3.13 shows the predicted variation of the spontaneous flux with inductance, $M(\Phi)$, as well as the spontaneous current, energy, and phase across the smaller junction for the simplified case where one junction

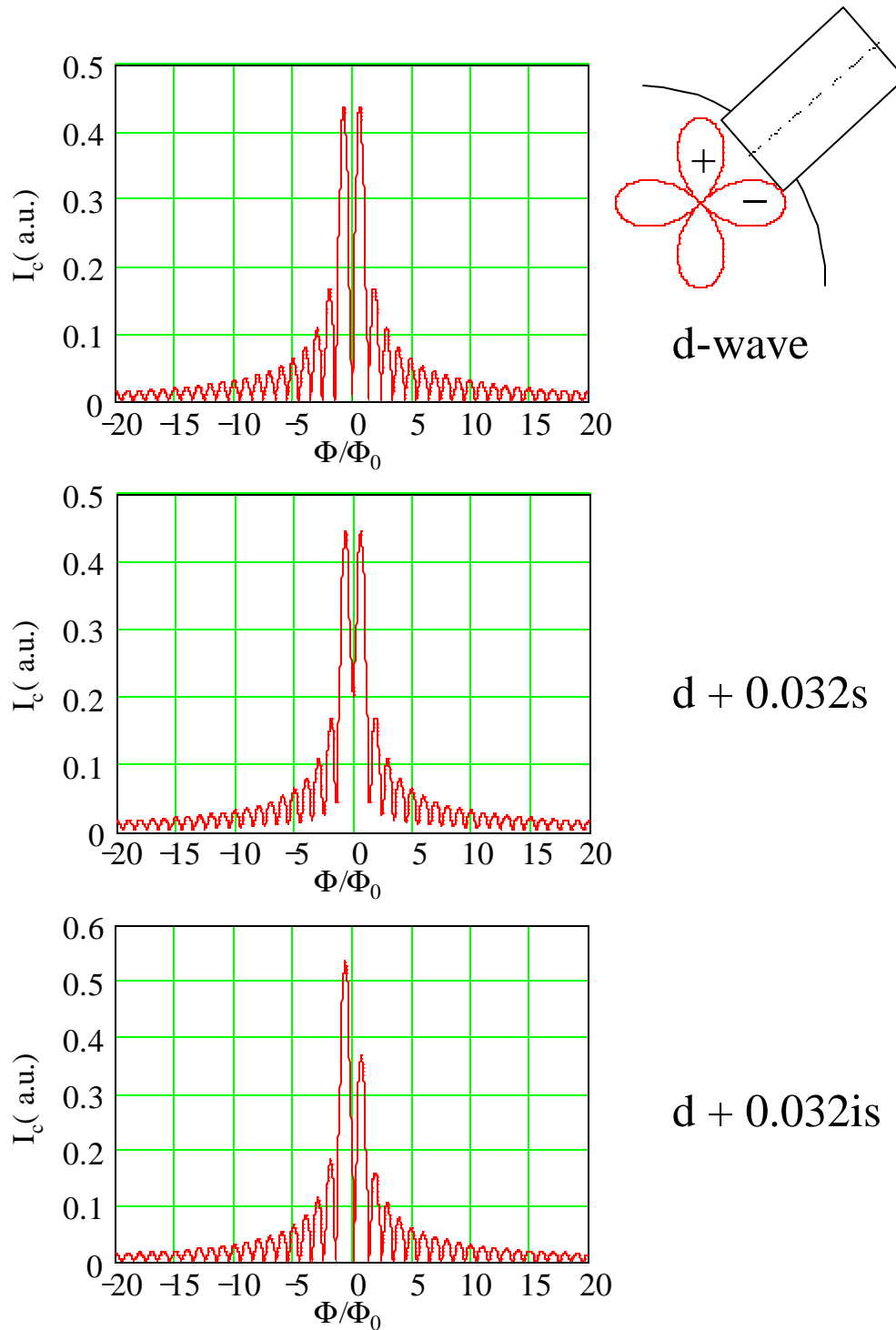


Figure 3.11 Ideal I_c versus flux for a rounded edge junction covering $\pm 2.3^\circ$ of arc about the 45° direction (shown schematically in upper right) with pure d-wave order parameter (top) and real and complex admixtures of s-wave (middle and bottom).

in the SQUID under test has a much smaller critical current than the other. Here β' is dimensionless inductance parameter defined in terms of the critical current of the lower I_c junction, $\beta' = \beta L I_{c1} / 2M_0$. Three different phase differences, 0, $\beta/2$, and β between the two SQUID junctions are shown in this figure. These cases would correspond physically to an edge SQUID with any order parameter, or a corner SQUID with an s-wave order parameter for 0, a 0-90 corner SQUID with a d-wave order parameter for β , and 0-45 degree corner with an equal complex mixture of s and d for $\beta/2$.

Our calculations show that in the case of an edge SQUID or s-wave SQUID, no flux signal is expected, while in the case of a d-wave corner SQUID, no signal is seen for $\beta' < 1$, but an initial peak and an asymptotic decay to one half flux quantum are predicted as β' increases above one. This is easiest to understand in terms of the energetics and the single value phase constraint around the SQUID loop,

$$\phi = 2\beta L I / M_0 + \theta^* = 0 \pmod{2\beta}$$

where θ^* is the intrinsic phase shift between the two junctions, 0 for an all s-wave system or a same edge SQUID, β for a s-d corner SQUID. For an s-wave SQUID, ϕ can and will be zero for any β' , but for a d-wave SQUID, the phase constraint prevents ϕ from being zero, leading to a competition between inductive energy, $\frac{1}{2} L I^2 = \frac{1}{2} L I_c^2 \sin^2 \phi = \beta' \sin^2 \phi$, and Josephson energy, $-E_J \cos \phi = -(M_0 I_c / 2\beta) \cos \phi$. For large β' , it takes relatively little current to satisfy the phase constraint, but as β' decreases, the I^2 increase in inductive energy becomes more and more important until at $\beta' = 1$, it becomes equal to the Josephson energy at zero current. For $\beta' < 1$, the phase constraint can only be satisfied by $\phi = \beta$, and hence $I = M = 0$.

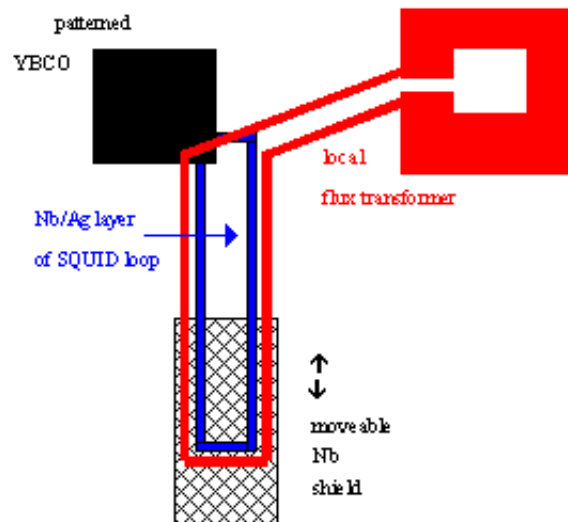
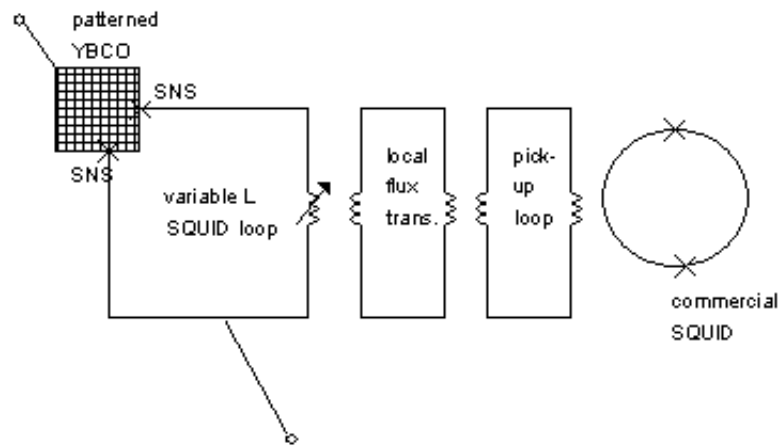


Figure 3.12 Circuit diagram (top) and schematic layout (bottom) of variable-inductance SQUID experiment (trombone).

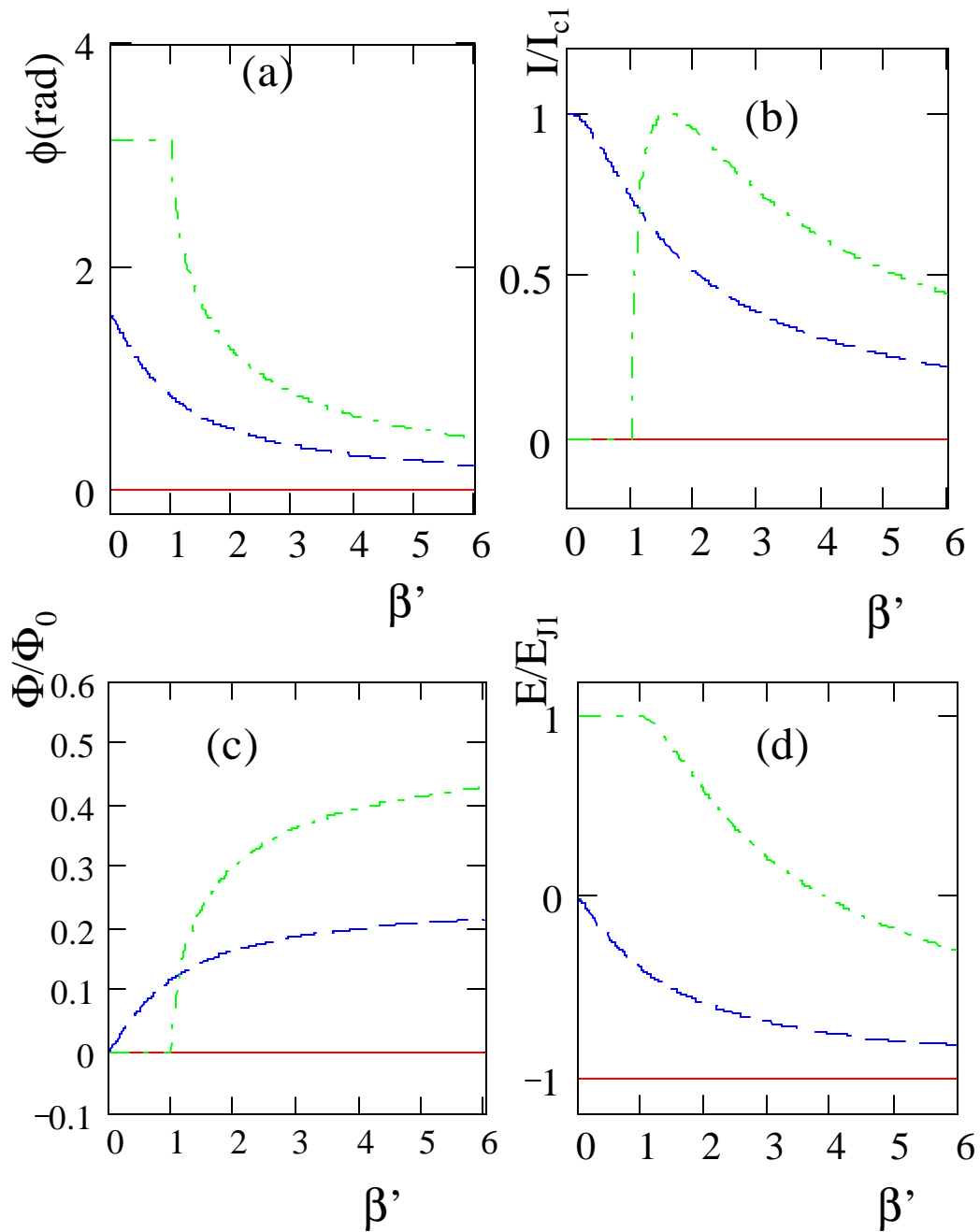


Figure 3.13 Ideal predictions for variable-inductance SQUID (trombone) experiment for phase differences between the junctions of 0 (solid), $B/2$ (dashed) and B (dash-dot). (a) is phase across the smaller $I_c (= I_{c1})$ junction; (b) is the circulating current; (c) is the flux produced by the circulating current; and (d) is the energy in terms of the Josephson energy, E_{J1} of the smaller I_c junction.

Also shown in figure 3.13 is the expected signal for a SQUID with an intrinsic phase shift of $\pi/2$. A $\pi/2$ phase shift would be expected for a SQUID with one junction at a 45 degree angle if that junction could be made sensitive to the predicted secondary surface order parameter for a d-wave superconductor with an abrupt surface at that angle. Here the phase constraint does not permit $\phi = \pi$ or 0, so there is always a finite flux signal. Finally, we note that when the I_c 's of the two junctions are comparable, the ϕ' value for which $M(\phi')$ begins to increase from zero changes, but the overall shape of $M(\phi')$ is retained.

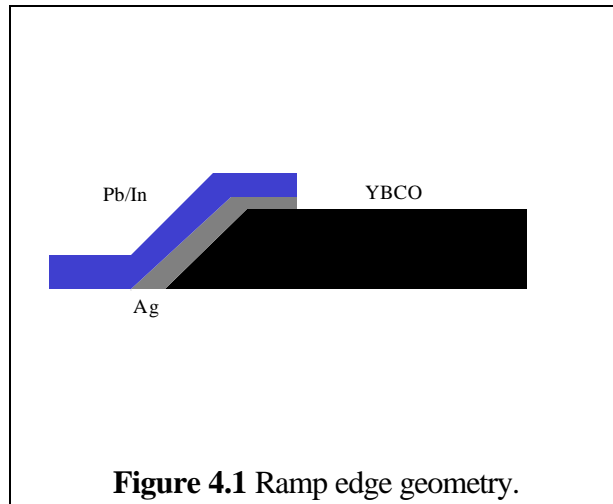
Overall, there are two advantages to this variable inductance technique. First, it allows us to separate out the effects of inductance on the spontaneous circulating current from those due to intrinsic phase differences in the cuprates. Secondly, if the technique were applied to future materials for which the large ϕ' limit, and hence an exact $M_0/2$ spontaneous flux were difficult to obtain, a signature of the $d_{x^2-y^2}$ or some other order parameter could still be obtained by varying the inductance over whatever range of ϕ' is available. Of course to observe $d_{x^2-y^2}$, one would have to at least get above $\phi' = 1$.

Chapter 4

EXPERIMENTAL TECHNIQUES

4.1 Fabrication Techniques

All of the Josephson junctions used in this thesis are based on the ramp-edge technology shown in cross-section in figure 4.1. Using standard lithographic techniques, the ab plane component of the normal to YBCO ramp where the junction is formed can be oriented in any arbitrary direction.



The core steps to fabricate the junctions are shown schematically in figure 4.2, and include: pulsed laser deposition of the YBCO thin film; photolithography and ion milling to pattern the YBCO thin film; evaporation or sputter deposition of the normal metal layer; annealing to improve the contact of the normal metal with the YBCO; evaporation or sputter deposition of the conventional superconductor; and finally photolithography and ion milling to pattern the conventional-superconductor/normal-metal bilayer. The variable-inductance devices (trombones) have an additional set of fabrication steps to make and insulate the on-chip pick-up circuitry. All the devices are connected to contact pads on the chip for making electrical measurements. Small indium blobs are pressed onto each contact pad to facilitate electrical

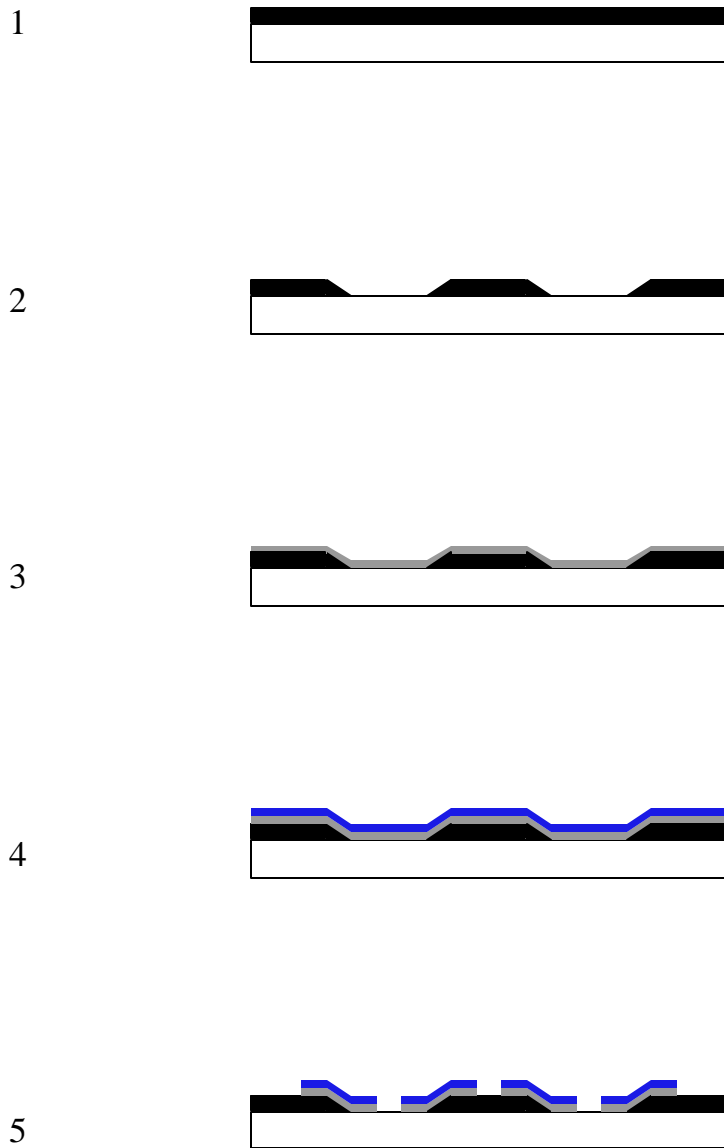


Figure 4.2 Core device processing steps: 1. LASER ABLATE YBCO film. 2. ION MILL YBCO pattern using photoresist mask. 3. EVAPORATE Ag, 1000 to 2000 Å typical. ANNEAL in O₂, 1 hr. 450 C typical. 4. EVAPORATE Pb (or sputter Nb in early runs), 2000 to 3000 Å typical. 5. ION MILL Pb/Ag layer pattern using photoresist mask.

contact either with a rigid pin in a screw-down sample holder (described in section 4.2.1) or with a copper wire lead with another small blob of indium melted onto one end.

The rest of section 4.1 covers these steps, their required equipment, and the choices and tradeoffs involved therein. Unfortunately, many of the early runs through this fabrication process resulted in a very poor yield of only a few percent of working Josephson junctions. By the end of the experiments of this thesis, the yield had been raised to about 75% with all of the junctions on each chip as a whole either working or not working. However, to reach this point adjustments had to be made to every step in the process, a frustrating journey through parameter space. As will be mentioned below in context, the important adjustments made were the increase of the oxygen pressure during ablation, the obtainment and use of a liquid nitrogen cooled stage and the use of lower voltages during ion milling, the raising of the normal metal annealing temperature to 450/ C and the increasing of the normal metal thickness, and the use of Pb instead of Nb as the conventional superconductor.

4.1.1 Pulsed Laser Deposition

Laser ablation is a physical vapor deposition technique in which a target material is stoichiometrically vaporized by a short intense laser pulse. The resulting plume, which consists of ions and neutral species of various sizes, travels away from the target toward the substrate where it sticks to form a thin film. The ablation can be performed in vacuum or in the presence of a desired gas at pressures less than or of order 1 torr and the substrate can be heated if desired to enhance surface diffusion and epitaxial film growth. This technique was first applied to the YBCO system in 1987 (Dijkkamp 1987), and since then has been extensively

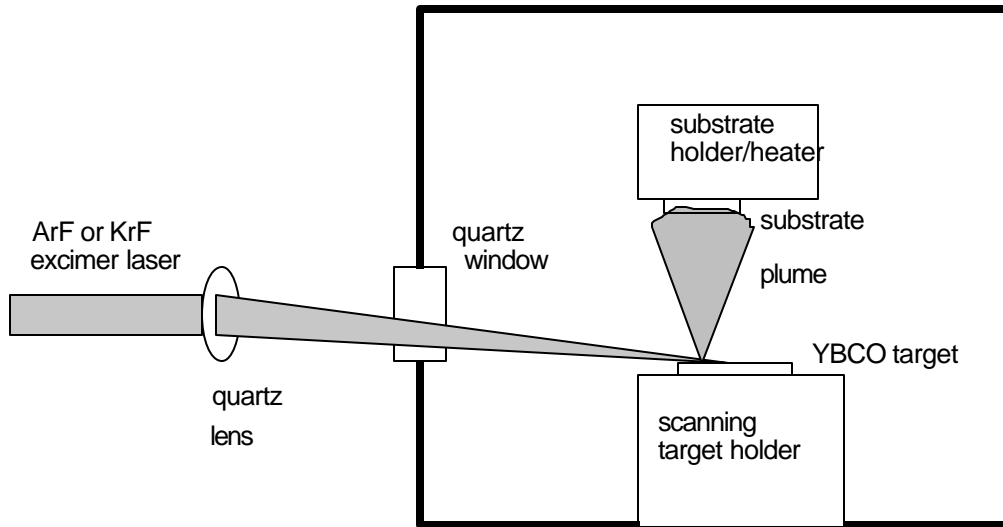


Figure 4.3 Picture and schematic of pulsed laser deposition system.

studied in papers too numerous to cite in detail here.

The pulsed laser deposition (laser ablation) system used for the YBCO films is shown in figure 4.2. This system was originally built by former Van Harlingen group graduate student Ralph Schweinfurth with assistance from Mark Wistrom and dubbed the AXL (Schweinfurth 1994), but the laser has since been replaced and other modifications made by the author. The laser in the system is now a Lambda Physik Compex 301, capable of running either an ArF (193nm output) or KrF (248 nm output) gas mixture. A quartz lens and quartz window focus and direct the beam into the ablation chamber and onto the target, which is mounted on a 6 target carousel. The ablation targets for this system were all commercially made and included YBCO targets from Superconductive Components Inc. and Jupiter Technologies. Other targets, namely NCCO, MgO, SrTiO₃, and CeO₂, all from Superconductive Components Inc were also available. The target carousel was mounted on a manual-rotating feedthrough and bellows assembly with a stepper motor controlled XY translation stage (Huntington model MTS 275-155), which thus allowed for manual selection of the target and automated scanning of the selected target to avoid always hitting the same spot with the beam. The resulting plume deposited material onto the sample which was mounted with Ted Pella Inc. Leitsilber silver paint on a stage heated with a quartz halogen bulb (Ushio JCV 1200W). The temperature was monitored by a K-type thermocouple and controlled with an Omega CN2011 temperature controller with its continuous analog output connected to a Phasetronics EP1-2425-BFX1 power supply for the bulb. The vacuum chamber was pumped by a Balzers TP240 turbo pump backed by an Alcatel mechanical pump, both with inert Fomblin pump oil to avoid any reaction

with the oxygen being pumped. Ultra high purity gases were introduced into the system by a network of copper tubing, valves and MKS mass flow controllers. Finally, the system also had two *in-situ* sputter guns and a 3 cm ion mill that could be accessed by means of a magnetically coupled load lock arm.

In most ablation runs, we have used the $\lambda=193$ nm ArF excimer laser gas mixture at a pulse energy of 300 mJ and a repetition rate of 3 Hz. The laser spot was typically focused down to roughly an 8×3 mm area on the target resulting in a fluence of about 0.6 J/cm^2 after accounting for losses in the quartz lens and chamber entrance window. During the ablation, the substrate was heated to typically 800 C and a pressure of typically 500 mtorr of oxygen was maintained by adjusting the mass flow controller. The substrates used are MgO, SrTiO₃ or LaAlO₃ and could be reused after repolishing to an epitaxial finish with a Buehler Minimet polisher. After each ablation, the pumps were turned off, the chamber filled to 1 atm with oxygen and the sample annealed for typically one hour at 425 C. A typical ablation lasted for 4 minutes, and deposited about 2000 Å of c-axis oriented material epitaxially with a critical temperature that can range from 80 to 92 K and transition width from 1 to 10 K.

In addition to the critical temperature, which was measured in a flow-through helium gas cryostat by the standard inductive pick-up technique using two hand wound coils and a lock-in amplifier, two other characteristics were recorded for every ablated film. First, the surface quality was inspected with an optical microscope. The best samples had no pinholes visible when illuminated from below and only sparse particles of size $1 \text{ : } \mu\text{m}$ or smaller, but did have a uniform background texture with feature size of order 300 nm which was barely resolvable with

the optical microscopy. Samples which had too many pinholes or too many particles larger than the background texture were rejected. The second characteristic was the sheet resistance, as measured with a four point probe technique with probe spacing approximately 2 mm. Good films had raw sheet resistances of order 3 to 6 ohms. Those with higher resistance were never found to make good devices, presumably due to film non-uniformity, and were usually rejected out of hand. Most samples with such high sheet resistance date from fairly early in the process when lower oxygen pressures were used than the eventual standard of 500 mtorr. Those with lower sheet resistance were found to be excessively thick and would usually run into processing trouble due to excessively long ion milling times.

4.1.2 Photolithography

Photolithography has long been a standard technique in the semiconductor microfabrication industry in which a photosensitive layer is applied to the sample, exposed to a pattern of light developed and used as a stencil for further processing. All photolithography equipment used in this work belongs to the MRL Microfabrication Facility. In this work, one of the simplest versions of photolithography is used, namely contact printing. In this process, AZ5214 photoresist is spun onto the sample at 4000 RPM making a layer about 1.8 μ m thick. AZ5214 is a positive photoresist, which means that areas of the resist which are exposed through the mask end up being developed away, thus making a positive image of the mask. After a softbake, the photoresist is exposed to broadband UV light through a mask aligned and contacted to the sample with a Karl Suss MJB3 aligner. The masks are either electron beam written chrome originals made for the Van Harlingen group by John Hughes of the University of

Illinois at Urbana Microelectronics Laboratory, or ferric oxide mask copies made from the originals. After exposure, the resist is developed in a dilution of AZ351 developer (4 deionized H₂O: 1 AZ351) and postbaked for 2 minutes at 130 C to harden it for the ion milling step. Finally, after ion milling the photoresist was removed by ultrasounding in acetone and further cleaning in isopropyl alcohol.

In a few cases, however, it was necessary to make a negative image of the mask, which was done by adding a post-exposure baking step (115 C for 40 sec) and a UV flood exposure step (typically twice as long as the mask exposure) between the mask exposure step and the development step. This reversal procedure is well-established for AZ5214 and is discussed extensively in the AZ photoresist product literature from Hoechst Corporation. Usually the purpose of image reversal when done was to create a lift-off mask for deposition of an insulator layer to use as the ion milling mask instead of using the photoresist itself as the milling mask.

The most important aspect of the photolithography, aside from avoiding major defects such as breaks in the pattern, was the quality of the pattern edge. This defines the edge of the finished ramp junction on the YBCO level which determines the accuracy of the junction as a directional probe. In the best lithography, these edges appeared perfectly straight on the highest magnification of an optical microscope over the entire junction length, which ranged from 20 to 50 : m depending on the particular device pattern. This puts an upper limit of about 300 nm on the scale of any possible edge roughness. To ensure this quality of lithography, it was necessary to pay attention to the cleanliness of the sample and mask and also to ensure the

smoothness of the back side of the sample since any debris or bumps there would wedge the sample, preventing flat contact of the whole top surface with the mask.

4.1.3 Ion Milling

Ion milling is a standard dry physical etching technique, which removes material from the sample by bombardment with accelerated ions. Most of the ion milling in this work was done with a Commonwealth Scientific 8cm ion gun powered by a Commonwealth ID3501 power supply and using Ar^+ ions. The system is pumped out first by a mechanical roughing pump, then by a cryopump to high vacuum. Like the photolithography equipment, this equipment belongs to the MRL microfabrication facility. Some other milling was done either in the ablation system or in the Nb sputtering system (described below). Both the Commonwealth system and the Nb sputtering system had the capability of cooling the stage with cold N_2 gas. Typical ion milling steps for the YBCO layer were carried out at a beam voltage of 350 V, a current density of 1 mA/cm^2 , and a total milling time ranging from 15 to 30 minutes with the ion mill cycled on and off in 5 minute intervals to further minimize sample heating. The milling stage temperature for the best samples was -50 to -70 $^{\circ}\text{C}$. For the metallic layers, a higher voltage of 500 V was used for Nb or 375 V for Pb and other metals, but the milling times were typically much shorter, usually less than 5 minutes.

Because the Josephson effect is most sensitive to the order parameter nearest the surface, possible crystal damage to the exposed YBCO ramp surface created by the milling process was a concern. Unfortunately, little has been published about ion damage at the energies less than 1000 eV typical of ion milling. The most relevant quantitative information the

author could find is a study of the perovskite substrate crystals LaAlO_3 , SrTiO_3 and NdGaO_3 (Takeuchi 1997) where a damage depth of 60\AA was reported. In any case, it appears that crystal damage may have been a minor factor since junction critical currents were generally greater for junction ramps milled at a glancing angle of 45 to 60 degrees than for junctions milled straight on or at an acute angle.

Possible damage to the YBCO from surface heating, both from the beam itself and from radiation from the ion mill's hot neutralizer filament was also a concern. This is both because heating in a vacuum with no oxygen will deoxygenate the YBCO, increasing the dead layer and because heating during ion milling tends to increase the damage depth.(Kaufman 1987) In both of these cases, making metallic contact to the YBCO with the subsequent normal metal deposition and annealing steps becomes more difficult. However, the attainment of working Josephson junctions indicates that the cooled stage and cycling on and off of the ion mill were an adequate solution to these potential problems. Earlier runs before the nitrogen-cooled stage was obtained on the Commonwealth system and also runs that used higher ion milling voltages for the YBCO milling had much lower yields.

4.1.4 Evaporation

Thermal evaporation has long been a standard deposition technique in materials processing, which involves the straightforward application of heat from an electric current through a refractory boat containing the metal (or other solid) to be deposited. The evaporant first melts, then evaporates, following straight line paths to coat everything in the chamber, including the sample, provided the vacuum chamber is pumped down low enough (typically the

low 10^{-6} torr range) to prevent collisions with significant amounts of residual gas. Most of the evaporation in this work was done in the same chamber with the Commonwealth 8cm ion mill described above, although some was done in an older system belonging to the Van Harlingen research group. Both systems were equipped with quartz crystal monitors for measuring the thickness of the deposited evaporant in real time.

The normal metal layer was typically evaporated Ag. Au was also used in some cases, but not in any of the junctions specifically presented in the data and analysis chapters of this thesis. Each of these metals was also deposited by sputtering in some cases. Both of these metals have been used in previous publications on phase sensitive YBCO/Pb Josephson junction and SQUID experiments.(Wollman 1993; Mathai 1995; Wollman 1995) The typical normal metal thickness used in this work was 1000 to 2000 Å.

Although many of the early devices were made with sputtered Nb as the conventional superconductor (described below), the best data were obtained with a Pb/In alloy (5% In by weight). This alloy was prepared by weighing out a total of 0.95 g Pb and 0.05 g In, cutting the metal wires thus weighed into small pieces and mixing them up in the evaporation boat. This mixture was then evaporated to completion onto the sample. Although the In was almost completely gone (as seen by the crystal monitor) before significant amounts of Pb evaporated, it is known that the In will migrate through the Pb as the Pb accumulates (Lahiri 1978; Sharifi 1989). For protection, a thin cap layer of about 100 Å of Ag was evaporated after the Pb/In because Pb is attacked by the alkaline photoresist developer during the next photoresist step and thus might otherwise discolor and buckle.

4.1.5 Annealing

Most of the annealing in this work was done in an Astro Industries A325 tube furnace or a Lindberg 59544 tube furnace with flowing oxygen, but some was done on the heater stage of the ablation system with 1 atm of oxygen sealed in the chamber. Although the annealing is simple to carry out it is one of the most critical steps in the process, since it is what allows the normal metal to diffuse through the YBCO dead layer caused by deoxygenation and any possible milling damage to make metallic contact to the superconducting YBCO.

The typical annealing temperatures were 450 C for Ag normal metal layers and 500 C for gold. The typical time was one hour. Time temperature and the presence of oxygen were all significant since devices attempted with significantly lower annealing temperatures (less than 400 for Ag or 475 for Au), short times (less than 20 min.) or without oxygen (either high vacuum or a nitrogen atmosphere) all resulted in large contact resistances, which increased substantially when the sample was cooled and precluded any chance at obtaining a Josephson current. In early fabrication runs with Ag as the normal metal, 400 C was used as the annealing temperature, but the yield of these runs was very erratic. This was likely due to variations in ablated film quality and ion milling damage which the metal would be less likely to diffuse all the way through at the lower temperature.

While hotter temperatures, longer times and more oxygen are needed to get good contact resistance, this combination can lead to another problem, namely roughening or even complete agglomeration of the normal metal layer. This problem has been reported previously in the literature (Sharma 1979b; a; 1980), but was stumbled upon independently by the author

before finding it in the literature. For the temperature range used in this work, there is always some roughening, but complete agglomeration only occurs in the presence of oxygen which enhances surface diffusion. The temperature required for roughly the same amount of roughening was 50 to 100 C higher for Au than for Ag. However, even in oxygen, the roughening could be reduced and the agglomeration usually avoided by going to thicker silver or gold layers. For the 1000Å normal metal thickness typically used in this work roughening was usually about the same order of magnitude as the background texture size of the ablated YBCO films, about 200 to 300 nm, although some samples were worse, presumably due to variations in substrate surface quality or defects in the as-deposited normal metal film. The 500 Å thickness used in early parts of this work gave much poorer results for roughening and agglomeration.

4.1.6 Sputter Deposition

Sputter deposition of Nb, for those devices using Nb was done in a custom sputtering system belonging to the Van Harlingen research group, which also had two other sputtering guns with SiO₂ and Al targets respectively. Since Nb is the superconductor of choice for commercial SQUID devices, there have been many investigations of the sputtering parameters for this refractory metal. The primary factors involved in obtaining a good Nb film are rate and sputtering pressure. Since Nb is an excellent getter of O (which is used in this chamber for sputtering SiO₂ and AlO₃) it is important to sputter fast enough to minimize oxygen incorporation to avoid a suppressed or absent superconducting T_c. A rate of 15 Å/s has been found by various members of the Van Harlingen group to be sufficient for this purpose in our system. Sputtering pressure is the main factor affecting the tensile (pressure too high) or compressive

(pressure too low) stress of the film. A pressure of 10 mtorr Ar has been found to be optimal for our Nb system, based on lift-off tests by past Van Harlingen group members, where curling of the Nb during lift-off indicates tensile stress and buckling indicates compressive stress.

In cases where the silver or gold normal metal was sputtered instead of evaporated, this was done with a sputtering gun mounted on the ablation chamber. The purpose of this was to attempt to improve the yield of the Josephson devices by doing the ion milling (with an insulator mask), normal metal deposition and annealing all *in-situ*. In the end, however, it proved possible to get good devices without necessarily using an all *in-situ* process.

4.1.7 Pick-up and Insulation Layers of Variable-inductance Devices

The on-chip pick-up loop for the variable inductance (trombone) devices was isolated from the circuitry below by a double layer of SiO_2 , rf sputtered on using one of the other guns in the Nb sputtering system described above. The purpose of using a double layer was to ensure that there were no pinhole shorts between the pick-up layer and the circuitry below. To this end, the sample was thoroughly cleaned in between these two layers of SiO_2 to remove any dust or other debris that might inadvertently have caused pinholes in the first layer. To save cleanroom time, the contact pads were protected from the SiO_2 sputtering by small hand applied dabs of old photoresist, which was then lifted off in acetone and cleaned after each SiO_2 sputtering step. The pick-up loop itself was made of sputtered Nb patterned by lift off of a regular photolithography pattern. Finally, yet another protective layer of SiO_2 , or in some cases AlO_3 was added on top of the Nb pick-up loop, with the contact pads protected by dabs of old photoresist as in the insulation steps.

4.2 Measurement Techniques

Since the superconductivity of Pb and Nb, the conventional superconductors in this project, occurs at T_c 's of 7.2 and 9.2 K respectively, it was necessary to make all data measurements on the Josephson devices in a liquid helium cryostat, with the sample on an insert that allowed for electrical feedthroughs to the outside. Also, because flux trapping and other sources of spurious magnetic field would adversely affect the experimental results, it was important to employ magnetic shielding and to be able to heat and cool the superconducting devices slowly through their transition temperatures to expel trapped flux. The remainder of section 4.2 covers the cryostats, inserts and other equipment necessary to do this, as well as the room temperature electronics, and methods used for data taking.

4.2.1 Cryogenics, Cryostat Inserts, and Sample Holders

The liquid helium cryostat, which is shown in figure 4.4 has been owned by the Van Harlingen research group for many years. The helium space is inside a vacuum-insulated glass dewar, which is suspended inside another glass dewar which is used for a liquid nitrogen buffer between the Helium dewar and room temperature. The top of the helium dewar is sealed from the outside world by an o-ring seal under the sample insert's top plate, which also has small quick-connect ports to accommodate the liquid helium transfer tube, or additional wire feedthroughs. The Helium dewar is connected near the top to an extensive system of pipes

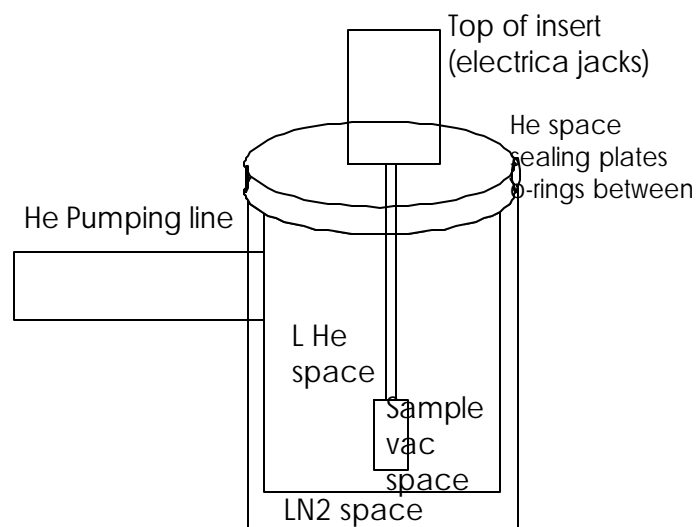


Figure 4.4 Picture and schematic of liquid helium cryostat.

valves and pumps which are permanently installed in the basement cryogenics lab of the MRL. The mechanical pumps in the system are capable of lowering the Helium bath temperature from its 1 atm value of 4.2K to as low as 1.35 K with the relevant valves open. A further reduction to 1.2 K can be obtained with one of the Roots blower pumps backed by a mechanical pump. Using the various other pipes and valves, the Helium dewar can also be backfilled with Helium gas and can be vented to a Helium gas recovery system to recover the boil off Helium gas.

The sample temperature was usually measured using a Lakeshore cernox resistor thermometer, although in cases where the sample was not in vacuum it could also be obtained by measuring the absolute pressure of the He space. In some early measurements, a Lakeshore diode thermometer was used, but it was found that the leads on its standard package (the SD) package were strongly magnetic and thus could affect the results both by introducing a stray offset field, and more importantly by causing flux trapping in the samples' superconductors as they cooled through their transitions.

Magnetic shielding was provided by a double-walled cylindrical mu-metal shield around the outside of the cryostat assembly. Further shielding inside the cryostat was provided by a lead can surrounding the sample space. A previous graduate student (Wollman 1996) has found that this arrangement reduces the residual magnetic field to below 1 mgauss, as compared to the ambient terrestrial field of about 0.5 gauss.

In this project, three inserts have been used to hold the samples in the helium dewar and allow wires for electrical measurements to feed through. These inserts are referred to as the sliding temperature-control insert (used primarily for the corner junction experiments), the spider

insert (used primarily for the single junction or “spider experiments) and the trombone insert (used for the variable inductance or “trombone” experiment, which was not completed). For most measurements, one of several small screw-down sample holders made by the author and mounted to the end of the insert was used to make electrical contact to the contact pads. Figure 4.5 shows the sample holders and insert hardware for the spider insert (a) and the trombone insert (b). The sliding temperature control insert was shown above in figure 4.4 installed in the liquid helium cryostat. All of the inserts were originally designed and built previously by other Van Harlingen students and the MRL machine shop, although the author has made substantial hardware changes to the spider and trombone inserts. The screw-down holders were made by the author and consist of a copper base and a plexiglass top with holes drilled in it to accommodate rigid non-magnetic pins in the exact pattern of the contact pads of the sample under test. The plexiglass top mounts on four threaded rods with springs around them coming up from the base plate and is tightened down onto the sample and base plate with four nuts.

All three inserts have electrical feedthroughs for electrical measurements of the samples, temperature measurements, resistive heating of the and applications of magnetic fields. The resistive heaters are non-inductively wound out of twisted pair manganin wire to avoid causing spurious magnetic fields, while the magnetic field coils are wound with superconducting wire to avoid spurious heating. The electrical measurement leads have non-magnetic 50 ohm resistors on the cold end of the insert to damp out electrical pick-up noise, but these can be bypassed to avoid unwanted heating in runs where large currents are needed.

(a)



(b)

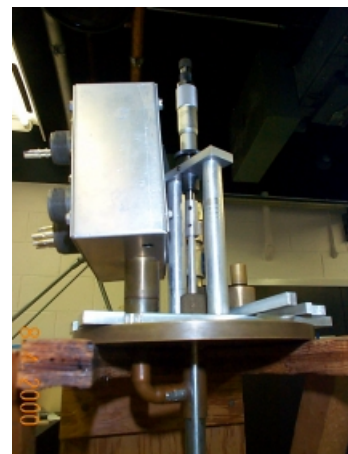
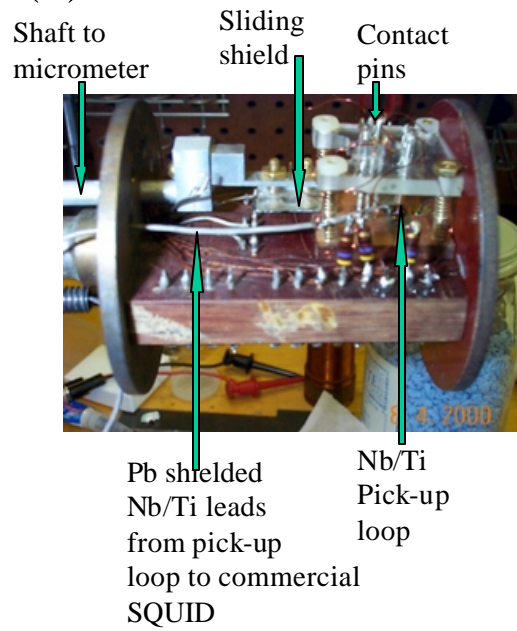


Figure 4.5 (a) Sample holder for spider insert (left) and whole insert(right)
(b) Sample holder, sliding shield, and pick-up loop with shielded leads (left) and micrometer hardware (right) for trombone insert.

In addition to the electrical feedthroughs, the trombone insert also has a 3/16 inch phenolic rod feed-through which is used to move the movable shield which is used to vary the cuprate SQUID loop inductance for the variable-inductance experiments done on this insert. The rod is attached outside the insert top plate to a non-rotating micrometer head which is anchored to the top plate and is used to position the rod and shield assembly within a precision of .001 inches. The shield itself is a superconducting thin film with a protective oxide layer and was held in a flip chip arrangement on top of the sample (which also had a protective oxide layer as discussed above in 4.1.7) by a spring-loaded holder on the end of the rod with two adjustment screws to adjust the pressure and levelness of the contact. The shield used for the preliminary data presented below was a Nb film on a silicon or glass substrate with a SiO_2 protective layer. An improved design would use a multilayer film consisting of YBCO on SrTiO_3 , protected by a MgO/SiO_2 bilayer buffer, and then further blanketed by a layer of Nb and top protective layer of SiO_2 . Since the shield's YBCO transition temperature was 92 K, higher than the post processing T_c of any of the devices under test, it will provide much better shielding for the devices during cool-down. The extra Nb layer is included to shield flux that may have gotten trapped in the YBCO or threaded through defects during the actual low-temperature data run.

While the trombone insert is always used with the sample directly in the helium bath, the sliding insert and the spider insert have the capability, if desired, to enclose the sample in a vacuum space inside the liquid helium space so that the sample can be heated to a temperature higher than the liquid helium bath temperature with a resistive heater on the insert's end paddle .

On the sliding insert, this is accomplished by means of a brass can which seals around the sample space on the end with a taper seal, while the spider insert uses a large stainless steel tube which encloses the whole insert from its top o-ring down and has a second o-ring to seal the liquid helium space. The sliding insert also has the capability of sliding the sample space up out of the helium bath without disturbing any of the seals to heat the sample still higher, but this feature was not used. Because of the size of the stainless steel tube, the temperature stability of the spider insert under vacuum was much worse than that of the sliding insert. Thus, while the spider insert was the only one with enough feed-through leads (80) to accommodate all 56 contact pads of a spider sample, the sliding insert had to be used for precise temperature-dependent measurements of spider samples. In this case, only 24 feed-through leads were available and contact to the pads had to be tediously made by pressing indium end coated copper wires onto the selected pads' indium blobs because the sliding insert's sample space was too small to accommodate a screw-down holder for the spider samples.

In addition to controlling the temperature, having the sample in a vacuum space was also useful for cooling down initially. By filling the helium space with liquid helium while the sample space is still well above the YBCO transition temperature, the lead can shield, which is directly in the bath outside the sample vacuum space can be made to go superconducting before the sample does. This way, the sample in the vacuum space can be made to cool slowly through its superconducting transition while taking advantage of both the mu-metal shielding and the lead can shielding, thus minimizing the possibility of initial flux trapping. Afterwards, when the sample

is close to 4.2 K, a small amount of helium exchange gas can be added to the sample space to speed up equilibration for subsequent temperature dependent measurements.

4.2.2 Electronics and Data Acquisition for Junctions and SQUIDS

Current-voltage characteristics, dynamic resistance measurements, and critical current vs applied flux interference patterns were all performed with a common set of equipment and a computer data acquisition system shown schematically in figure 4.6. The computer uses the National Instruments Labview software package and the National Instruments NI-DAQ general purpose data acquisition card. Most of the Labview programs used in this project were originally written by former graduate student Brian Yanoff, although some modifications have been made by the present author. In virtually all of the data runs on these devices, a bipolar retrace, that is sweeping the control variable out to its maximum, back to zero, out to its negative maximum, and back to zero again, is used in order to test the repeatability and symmetry of the data.

Of the three types of measurements covered in this section, the four-terminal current-voltage characteristic were conceptually the simplest. Here, current was run through the device under test (DUT) using one of several home-made voltage-controlled current sources previously built in the Van Harlingen research group, where the voltage was swept using one of the digital-to-analog converters (DAC) of the NI-DAQ card. The voltage drop across the device was then measured by two independent leads, which were wired into differential inputs of an Ithaco 1201 low noise preamp, whose output in turn was sent to one of the analog-to-digital converters(ADC) of the NI-DAQ card. The dynamic resistance measurements used the same

equipment plus a Princeton Applied Research lock-in amplifier. In this case, a 1 kHz reference

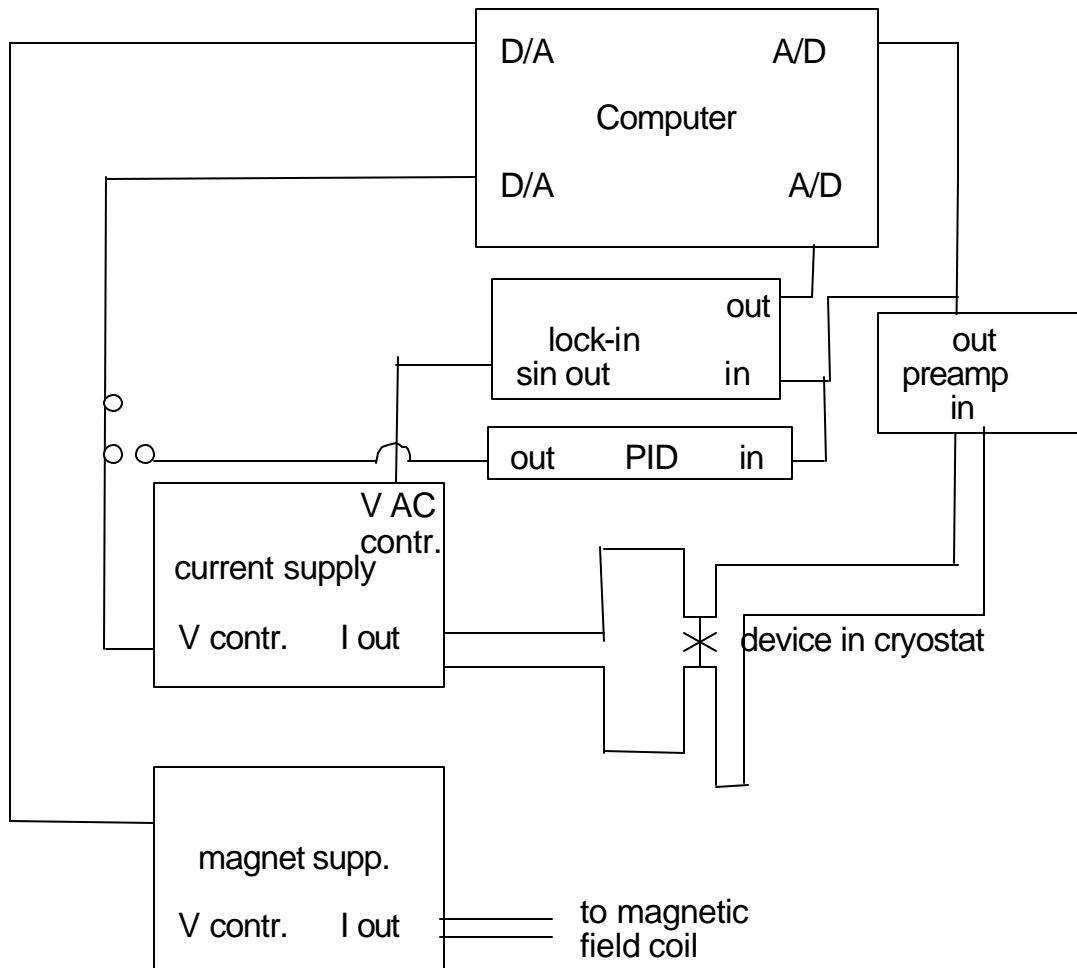


Figure 4.6 Schematic of data acquisition electronics.

sine wave from the lock-in was added to the current source output (typically less than 1% of the dc current) through a separate modulation voltage control input on the current source. The 1 kHz component of the DUT voltage was then detected with the lock-in and sent as a dc output voltage to a NI-DAQ ADC channel. Also, the current source used to drive the DUT for the dynamic resistance measurements was actually two current sources in parallel, with one providing a constant offset to the current of the other, which was controlled by the computer. This was done to avoid having zero current in the DUT correspond to zero current from either current supply since operation the current supplies near their zero points resulted in spikes in the dynamic resistance data due to so-called zero-crossing anomalies in the transistor circuitry inside the current supplies.

For the critical current versus flux interference patterns, flux was generated by current applied through the appropriate modulation coil on the insert in use. Usually a battery-powered voltage-controlled current supply was used for this purpose to avoid oscillations in the DUT voltage caused by ground looping. For the data taking on the interference patterns, two different methods were used. For many of the earlier measurements a ramp method was used. Here, the NI-DAQ card was used to step the voltage-controlled current source up from zero until a threshold voltage was exceeded by the preamp output from the DUT. The negative critical current was also taken for the same flux immediately afterward by ramping down from zero current until the negative of the threshold voltage was passed. Drift in the preamp was compensated by re-measuring the actual preamp output for zero DUT current immediately before each data point. The other method used for most of the later interference pattern data

was an analog feedback technique. Here, the DUT was maintained constantly at the threshold voltage by feeding back the difference between the preamp output and manually adjustable reference voltage to the voltage controlled current supply through analog proportional/integral/derivative (PID) circuitry previously made in the Van Harlingen group. The derivative gain was always set to zero. This second method offered the advantage of increased speed and increased sensitivity to small features in the interference, whereas the ramp method was limited by discretization error at low currents. The tradeoff was that only one polarity of the current could be measured and there was now a slow drift error from the preamp because the zero current preamp measurement could not be measured separately in this arrangement.

4.2.3 Flux Measurement of Variable-inductance Devices

Most of the time, measurement of the spontaneous flux in the variable inductance devices was made by means of a commercial dc SQUID, the model 50 from Quantum Design corporation controlled by a Quantum Design model 5000 control unit and a hand made secondary flux transformer. For a few measurements, however, a much older SHE corporation rf SQUID and controller was used while the newer Quantum Design equipment was gone for repair. That the SHE equipment still worked is a testament to the stability of Nb based SQUID magnetometers. In both cases, a voltage proportional to the change in flux through the SQUID could be read directly from the front panel by the operator or sent to the computer data acquisition system, oscilloscope, or voltmeter via an output jack on the controller.

The raw data, controller voltage versus moveable shield position needed to be calibrated in order to compare with the simulations which make predictions in terms of

spontaneous cuprate SQUID flux versus inductance parameter $\Phi = 2LI_c/M_0$. For the preliminary results presented in chapter 5, this calibration could not be completed because of a break in a lead on the chip needed to measure I_c . However, for completeness, the calibration procedure is described in the paragraph below.

In order to make this calibration, it is necessary to know the cuprate SQUID critical current, the true location of complete coverage (zero position) of the cuprate SQUID loop by the moveable shield, and the conversion from commercial SQUID output to the actual spontaneous flux from the cuprate SQUID. The cuprate SQUID critical current is obtained by connecting to the appropriate pads and using the same methods for taking current-voltage characteristics and interference patterns as for the other kinds of devices detailed in the previous section (4.2.2). For cuprate SQUIDS that don't have both junctions oriented at zero or ninety degrees, it is also useful to know what fraction of the maximum critical current comes from each of the two junctions. This can be deduced from the modulation depth of the interference pattern (i.e. $I_{cmax} = I_{c1} + I_{c2}$, $I_{cmin} = |I_{c1} - I_{c2}|$) in the low Φ limit (device fully shielded). The zero position can be reasonably well approximated by measurement of the position of the edge of the shield relative to the edge of the chip with a caliper before setting up the insert in the dewar and of the position of the lithography pattern relative to the same edge with a microscope before setting up the device on the insert. This position can be confirmed *in situ* by measuring the effect of the modulation coil field on the commercial SQUID output as a function of shield position. While the cuprate SQUID loop is still uncovered the ratio, I_{mod}/V_{out} of modulation coil current applied to commercial SQUID output is approximately a linear function of the amount of cuprate SQUID

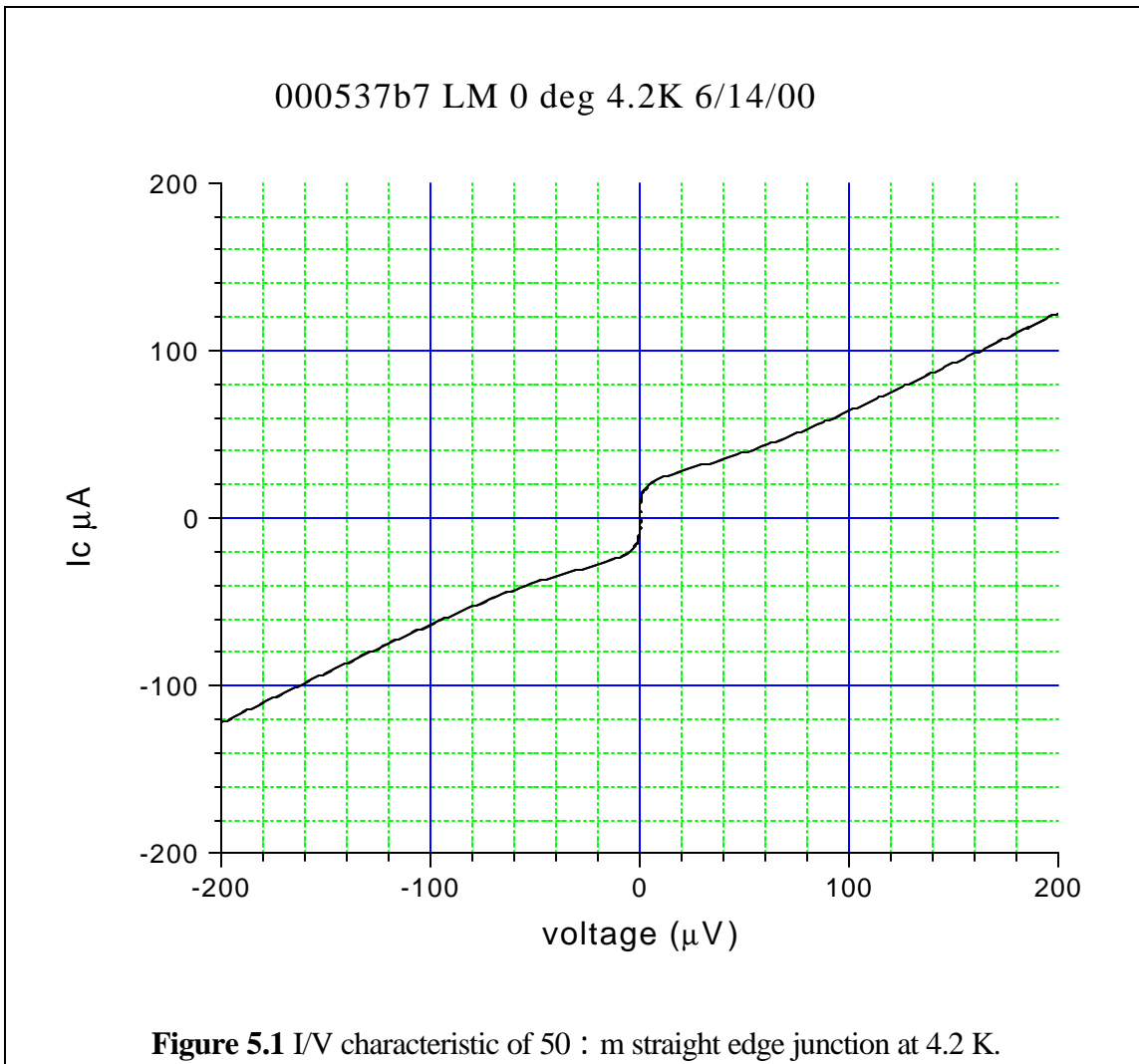
loop still uncovered. However, when the cuprate SQUID loop is completely covered, this ratio changes much less with shield position. The crossover point between these two regimes is the zero point. Finally, the calibration between flux in the SQUID loop and commercial SQUID output signal is made by first applying a field with the modulation coil, then either moving the shield, or changing the modulation coil until the cuprate SQUID critical current (measured simultaneously by four point technique as described above) goes through one or more cycles of its interference pattern. The change in commercial SQUID output divided by the number of cycles is the commercial SQUID signal corresponding to one flux quantum in the cuprate SQUID loop.

Chapter 5

DATA AND ANALYSIS OF CORNER EXPERIMENTS

In this Chapter, we present critical current versus field data and analysis on the arbitrary angle corner junctions and preliminary flux versus inductance data on the variable-inductance SQUID (trombone) experiment. The corner junction results confirm the established $d_x^2 d_y^2$ order parameter symmetry, but also provide information on the deviation from uniformity of the spatial critical current density profile $J_c(y)$ and allow us to estimate an upper limit on the stray field and /or intrinsic phase variation in the junctions. The preliminary data on the trombone experiment were not calibrated because of a break in a lead on the chip needed to measure the SQUID's critical current. These data are presented primarily to document the progress to date on the trombone experiment. Data and analysis on the single edge junctions, some of which show anomalous temperature dependences will be covered in chapter 6.

All of the junctions measured in this thesis showed non-hysteretic RSJ behavior. An I/V plot of a typical junction is shown in figure 5.1. The critical currents varied from junction to junction and with temperature ranging from 400 : A down to less than 10 : A. The amount of rounding also varied with the most rounding for the smallest critical currents. The normal state resistance of the junctions of this thesis varied over a typical range of 0.15 to 1 ohm.



5.1 Corner Junction Data and Analysis

5.1.1 Data and Qualitative Analysis

Figure 5.2 (a-f) shows the $I_c(H)$ results for the best corner junction sample at 1.38K. Although the field scale on these plots is in gauss, the actual field scale in the junctions is not known because the degree of flux focusing into the normal region of our ramp junctions is not known in quantitative detail. The lowest I_c 's in these data are offset from zero due to our use of a voltage criterion for measuring I_c . For all of these junctions, the critical current in the minus

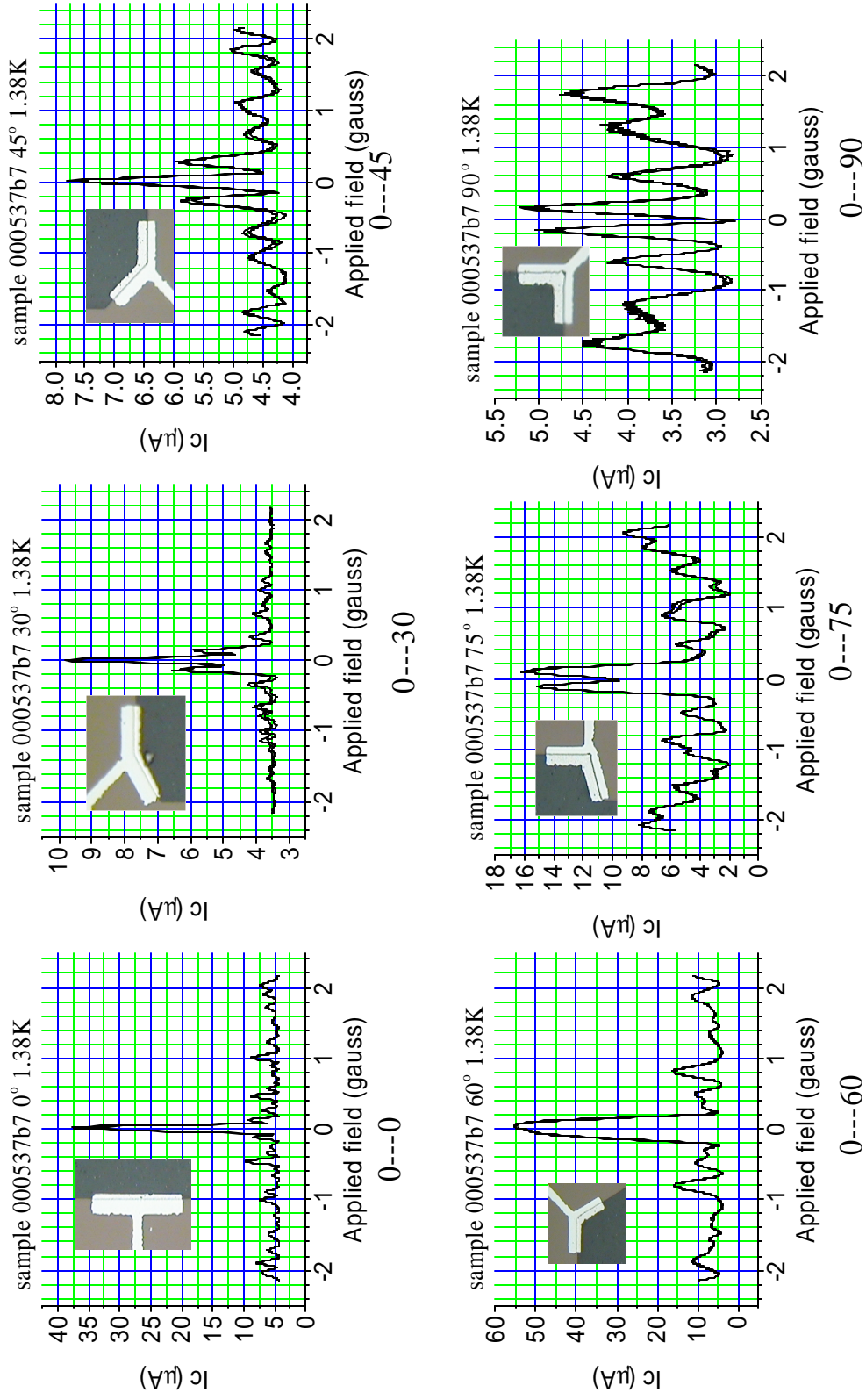


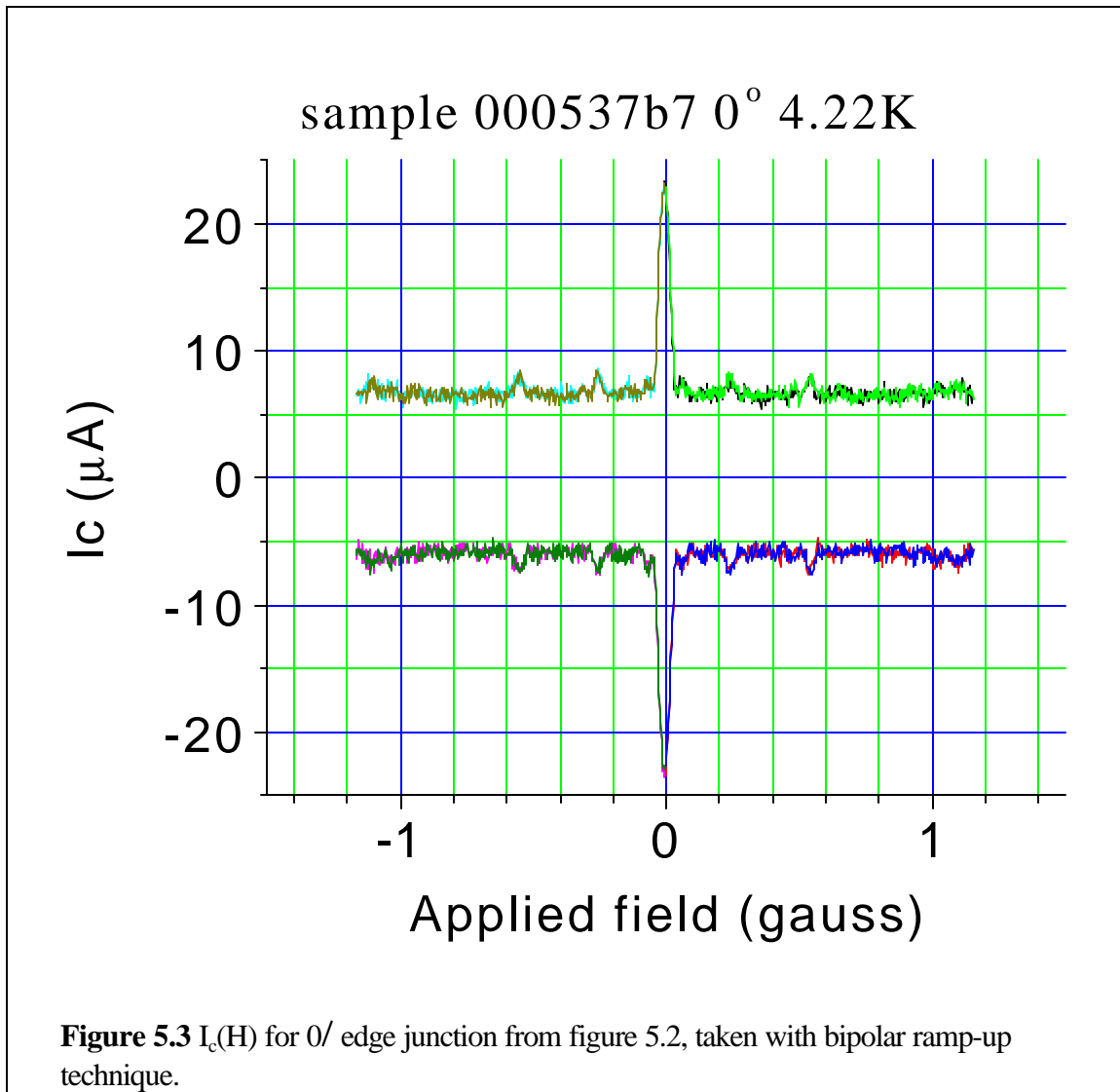
Figure 5.2 $I_c(H)$ patterns for 0° , 30° , 45° , 60° , 75° , and 90° corner junctions. Retraces are shown on each graph. Insets are optical micrographs of the junctions; the dark area is YBCO, the white is the Pb(In)/Ag bilayer.

direction always has the same magnitude as for the plus current direction (mirror symmetry).

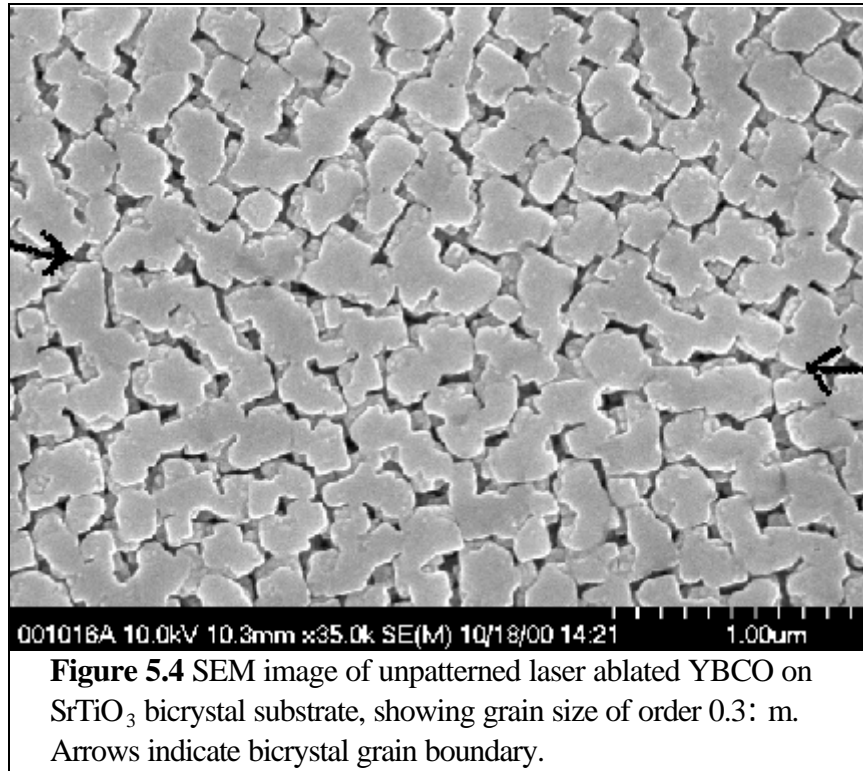
This can be seen for the zero degree corner junction in figure 5.3, which shows data from an earlier run where I_c was found by a ramp-up technique rather than a feedback technique.

This $\pm I_c$ symmetry is to be expected for any continuous Josephson junction in the short junction limit because in that case the critical current (or any lesser current) can be reversed by adding \mathbf{B} to the gauge-invariant phase difference $\phi(y)$ at each point, y , along the length of the junction, and this reversal will not change the net field which remains equal to the applied field. This mirror symmetry of I_c could only be broken in the case of significant self-field effects in the junction, since the detailed profile of current densities, $J(y)$ need not work out the same when the self field reverses direction with respect to the applied field. This self-field effect might occur in a long junction with a non-uniform critical current density $J_c(y)$ or in a junction with significant regions of negligible $J_c(y)$.

Now when we compare the experimental data of figure 5.2 with the ideal predictions of figure 3.8, we find good qualitative agreement, but quantitatively there is much more structure in the side lobes. In particular, for the 0° corner, which is equivalent to a straight edge junction, we see a strong central peak while the side lobes have no distinctive pattern to their magnitudes, but are approximately symmetric between positive and negative applied field. The slight offset from zero field of the central peak and slight asymmetry of the sizes of the side lobes are most likely due to stray field from trapped flux. Similar deviations from perfect mirror field symmetry are seen in the other corner junction data as well.



The 30/ corner junction has substantial shoulder peaks on the central peak, which appear to correlate with the shoulder peaks expected from the simulation. The side lobes are paired as doublets, again in qualitative agreement with the simulation. Aside from this, the 30/ corner is very similar to the 0/ junction, in particular, the periodicity of the side lobes is about the same. Assuming that the active length of the two junctions is about the same, this would indicate that the amount of flux focusing for the two junctions is about the same.



By contrast, the remaining corner junctions, from 45/ to 90/ have about twice the periodicity for the side lobes. This is also what is expected from the simulations, but again cannot be quantitatively confirmed because we have no independent way of measuring the flux focusing. As we proceed from the 45/ corner junction to the 90/ corner junction, we see that the central peak broadens and flattens in the 60/ junction and splits in the 75/ and 90/ junctions. If we account for the voltage criterion offset in I_c , we see that the 90/ corner junction has an approximate zero I_c at $H=0$, in good agreement with the simulation, but the 60/ and 75/ corner junctions have more I_c at $H=0$ than the ideal simulations would predict.

We attribute the quantitative deviation from the ideal $I_c(H)$ patterns primarily to junction roughness. Figure 5.4 shows an SEM micrograph (taken by fellow Van Harlingen student, W.

Neils) of an ablated YBCO film typical of those used to make the junctions in this project. Here, the typical grain size is seen to be about 0.3 μ m. For a straight junction oriented at 0 $^\circ$, we expect the critical current density to be approximately uniform along each grain, but drop considerably in between grains. A model current density and corresponding calculated $I_c(H)$ for such a junction is shown in figure 5.5. (The effect of roughness on junctions oriented close to 45 $^\circ$ will be considered below in section 6.4). Thus we see that junction roughness is a good qualitative explanation for the structure in the side lobes of the $I_c(H)$ patterns of our junctions.

5.1.2 Quantitative Computation of $J_c(y)$ with Appropriate Assumptions

A more quantitative analysis of this experiment is difficult because the experimental data represent only the magnitude of the Fourier transform of the critical current distribution $J_c(x)$ while the phase of this Fourier transform cannot be measured directly. This problem has been discussed in the literature on Josephson junctions (Dynes 1971; Zappe 1975; Barone 1982) and is also encountered in the reconstruction of objects from coherent x-ray diffraction (CXD) (Vartanyants 1997; Vartanyants 2000) and in optical holography (Gerchberg 1972; Millane 1990). In general, the only quantity that can be uniquely reconstructed from the magnitude of a Fourier transform $|F(k)|$ of a function $f(x)$ is the autocorrelation of $f(x)$, whose Fourier transform is $|F(k)|^2$. To extract a specific $f(x)$ would require additional a priori assumptions. In our case, we would like to extract whatever additional information about $f(x)$, and in particular about its phase, that we can, since this will allow us to make an estimate of the amount of stray field in the junction, as well as to estimate an upper limit on the amount of time reversal symmetry breaking that might be present in the junction.

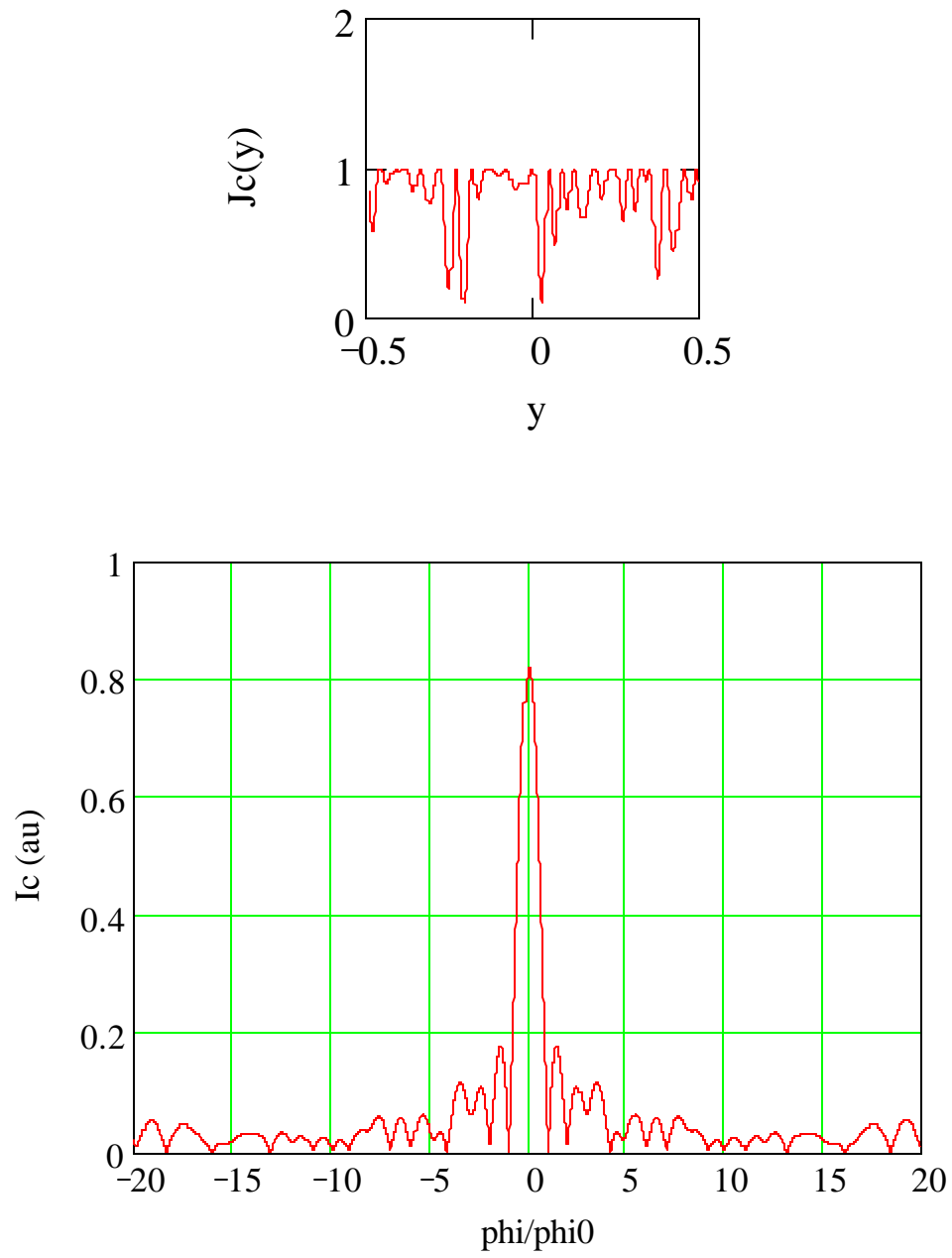


Figure 5.5 Model $J_c(y)$ and corresponding $I_c(M)$ for a rough 0/ edge junction.

One possible way to extract this information is to make the so-called minimum phase assumption (Dynes 1971), which essentially amounts to assuming a periodic phase of $|F(k)|$. Since $J_c(y)$ for a finite sized Josephson junction must be a causal function, the appropriate minimum phase for $|I_c(H)|$ can be found by the so-called Hilbert transformation (Papoulis 1962; Dynes 1971),

$$q(\mathbf{b}) = \frac{b}{2p} \int_{-\infty}^{\infty} db \frac{\ln(I_c(b)) - \ln(I_c(\mathbf{b}))}{b^2 - b^2}$$

where $\$$ represents the applied field H in units of flux quanta threading the junction. Some preliminary attempts to apply the minimum phase calculation to our junctions were made, but we ran into difficulty because of the sensitivity of the \ln functions to the regions of low critical current, which is exactly where the voltage criterion method of measuring the critical current creates the most distortion.

Instead, as an alternative to the minimum phase calculation, we have collaborated with Vartanyants and Robinson who have developed an iterative algorithm, based on the Gerchberg-Saxton (Gerchberg 1972) algorithm in optics, for solving the phase reconstruction problem in CXD (Vartanyants 1997; Vartanyants 2000). The algorithm begins by assuming a random phase $\mathbf{N}_{i=1}(k) = \mathbf{N}_{\text{rand}}(k)$ for $|F(k)|$. Then for each iteration, the inverse Fourier transform, $f_i(x)$, of $|F(k)|\exp(i\mathbf{N}_i(k))$ is taken. $f_i(x)$ is then altered to fit a desired assumption, such as finite spatial extent, and then Fourier transformed back to k -space, giving a new magnitude and phase $|F'(k)|\exp(i\mathbf{N}'(k))$. $\mathbf{N}_{i+1}(k) = \mathbf{N}'(k)$ is then used as the phase of the

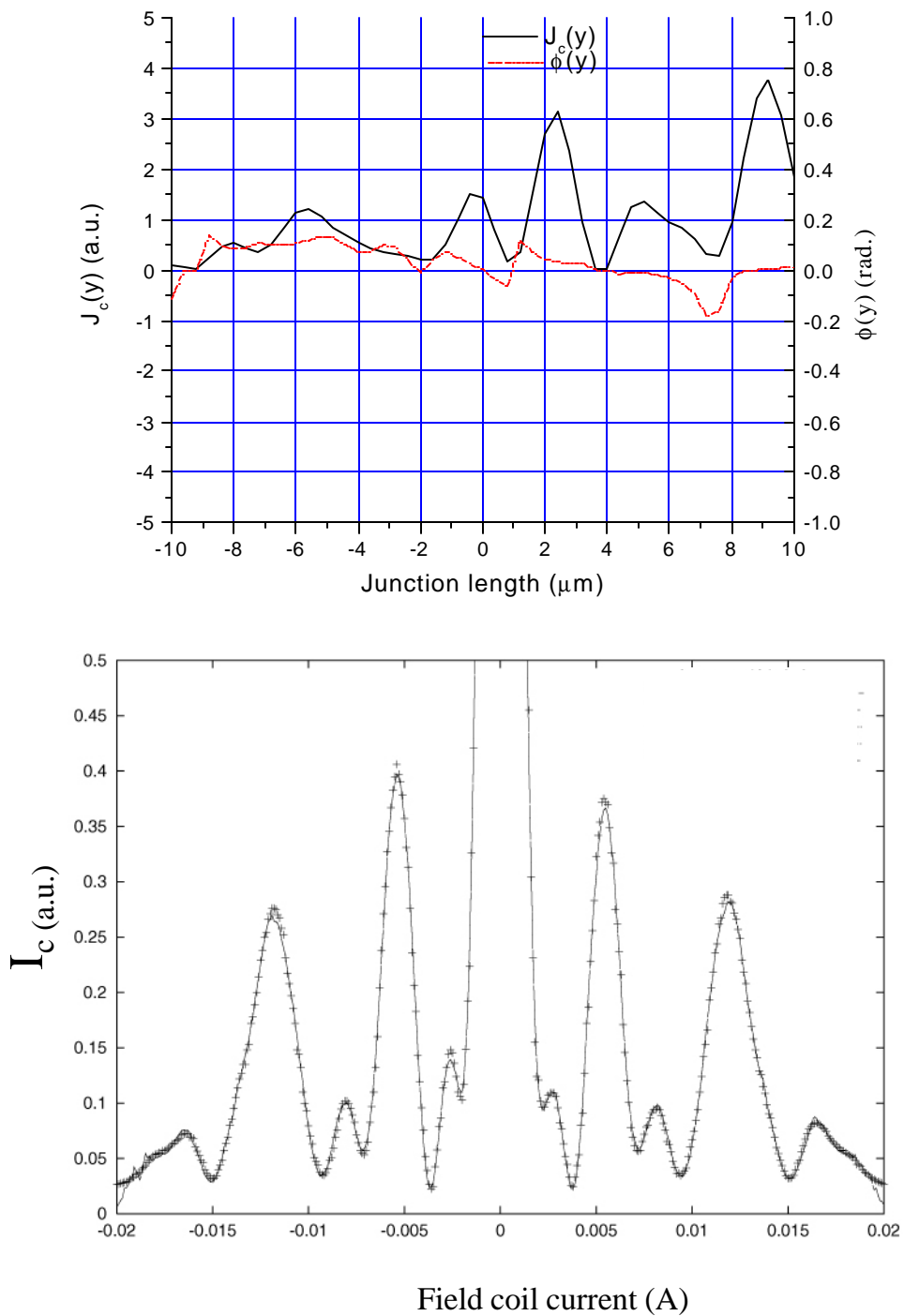


Figure 5.6 Top: $J_c(y)$ and $N(y)$ results on 20 : m edge junction from iterative algorithm described in the text. Bottom: fit to raw $I_c(H)$ data using this $J_c(y)$ and $N(y)$; crosses are data, line is fit.

original $|F(k)|$ for the next iteration. Iteration continues until convergence is obtained (typically 2000 iterations) and then the process is repeated with a new random initial phase to see if the same convergent result is obtained.

In our case, we had to restrict ourselves to $I_c(H)$ data that was at least qualitatively similar to the ideal Fraunhofer pattern and with only a small amount of asymmetry between + and - H in order to obtain consistent convergence. For junctions like these, we were able to obtain particular values for the magnitude and phase of the spatial critical current distribution, $J_c(y)$ by a two-stage application of the algorithm. In the first stage, we used the assumption that $J_c(y)$ was real (which is equivalent to ignoring the asymmetry in $I_c(H)$) and positive to find the magnitude, $J_{\text{creal}}(y)$, of $J_c(y)$. Then, in the second stage, we relaxed that assumption and required instead that the magnitude of $J_c(y)$ must remain equal to the $J_{\text{creal}}(y)$ calculated in stage one. After stage two, we now had the phase of $J_c(y)$ required to fit the asymmetry of $I_c(H)$. The magnitude and phase of $J_c(y)$ obtained with this method for a 20 : m wide edge junction are shown in figure 5.6, along with the original and best fit $I_c(H)$ for this junction. (For the 0/ junction of figure 5.2 convergence of the algorithm could not be obtained.) Differentiating the phase $N(y)$ gives an estimate of the stray field by $(M_0/2B)N(y) = M(y) = \int dy(\mathbf{g}_1 + \mathbf{g}_2 + d)B(y)$. Taking $(\mathbf{g}_1 + \mathbf{g}_2 + d) \sim 300\text{nm}$ gives an average stray field less than or of order 0.04 gauss.

Work will continue on the application of this algorithm to other corner junctions with the ultimate goal of publishing a study of the algorithm's range of applicability to Josephson interferometry. It is likely that corner junctions with neither face near 45/ will be good candidates for future analysis by this algorithm because they are expected to have at most one

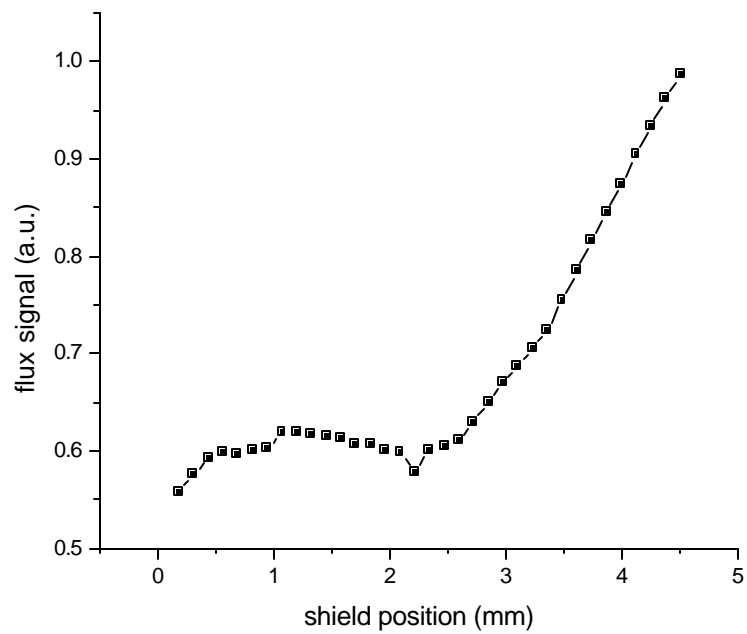
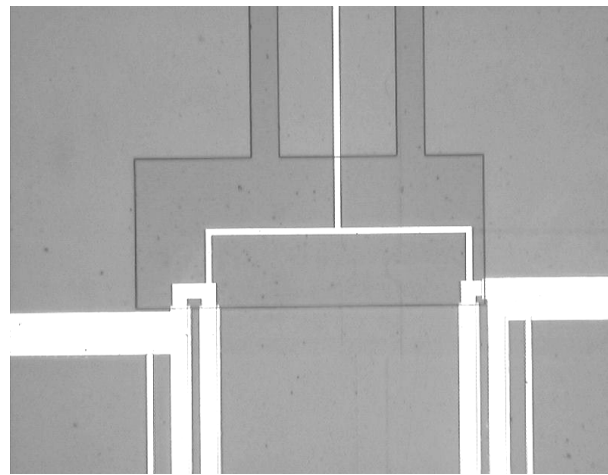


Figure 5.7 Optical micrograph (top) and flux vs position data for a preliminary measurement of the variable inductance SQUID (trombone) experiment.

sign change in their critical current density at a known location. For such junctions, successful convergence of the algorithm would be a useful test for their physical uniformity. On the other hand, edge or corner junctions with a face near 45° , such as many of the junctions studied in chapter 6 are not good candidates for analysis by this algorithm because they are expected to have many sign changes in their critical current density at unknown locations, and thus will not suggest obvious constraints to include in the algorithm to make it converge consistently.

5.2 Preliminary Data on Variable-inductance SQUID Experiment

Figure 5.7 shows an optical micrograph of a variable inductance SQUID (trombone) sample and the data for pick-up signal versus SQUID shield position obtained for that sample. Unfortunately, the position data could not be calibrated in terms of the inductance parameter Φ_0 , nor could the pick-up signal data be translated into flux-quanta in the variable inductance device (see sections 3.4.3 and 4.2.3) because one of the leads for measuring I_c of this device was broken. However, the increase in signal that begins at $x = 2.5$ mm is at least qualitatively suggestive of the prediction for a d-wave corner SQUID from figure 3.13(c).

Further measurements on this experiment were delayed by the need to send in both the commercial SQUID and its control box back to Quantum Design for repairs and were ultimately pre-empted by work on the corner and edge junctions reported in the rest of this thesis. Nevertheless, the trombone experiment is an elegant idea and it is the author's hope that it will be taken up again, if not by him, then perhaps by another Van Harlingen student in the context of investigating future superconducting materials.

Chapter 6

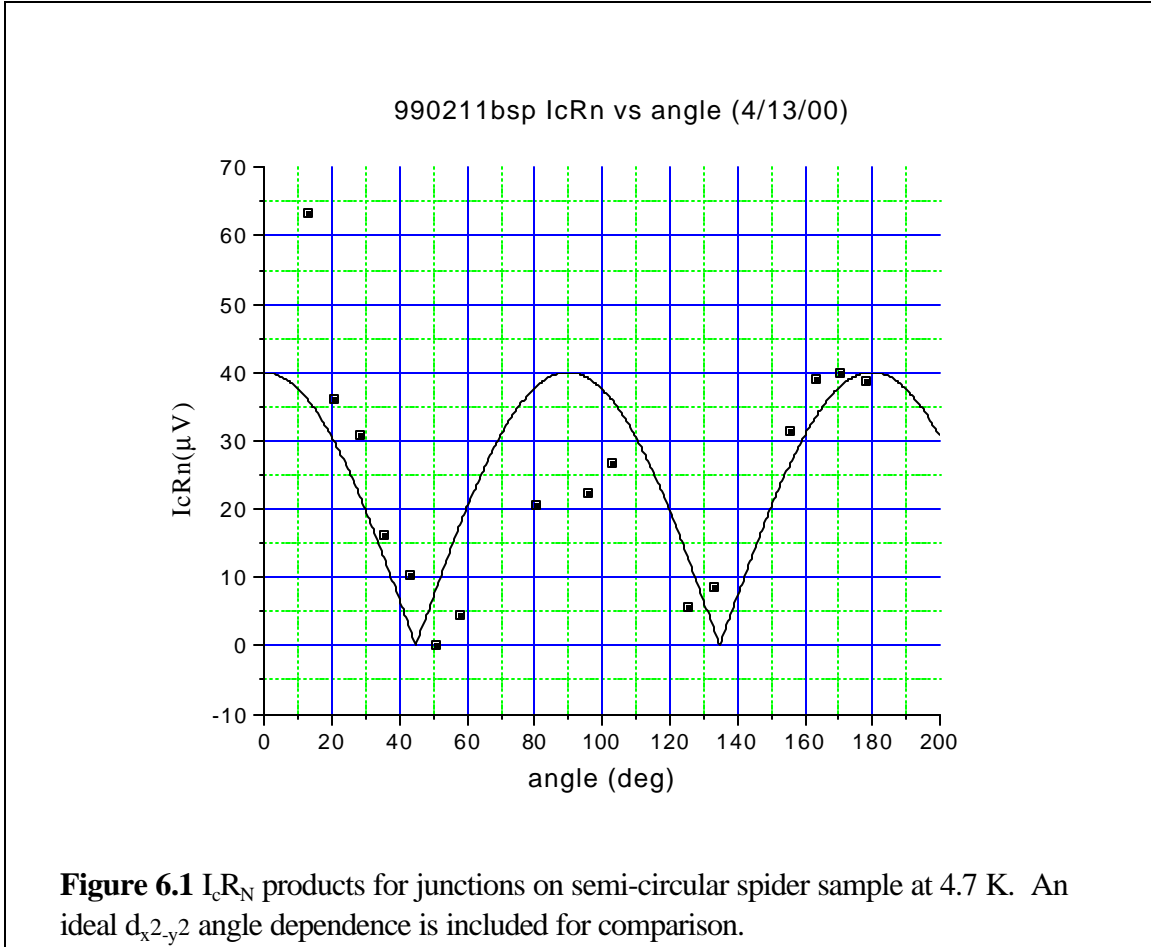
SINGLE EDGE JUNCTION (SPIDER) DATA AND ANALYSIS

While we've been able to get good directional phase and magnitude information from the corner junction experiments, our most direct information, particularly about the possibility of a secondary order parameter or second-order Josephson coupling near surfaces oriented close to 45 degrees with respect to the a and b axes, has come from the single junction (SPIDER) experiment. In this chapter we present data on single junctions oriented in various directions, including zero-field $I_c R_N$ products as a function of angle, critical current versus field, $I_c(H)$ measurements as function of temperature, and dynamic conductance measurements (dI/dV) as a function of temperature. While most of the results are explainable strictly in terms of the established $d_{x^2-y^2}$ order parameter, we find that some of the edge junctions oriented near 45 degrees show an anomalous increase in zero field critical current at temperatures below about 4K which could be a signature of the onset of either a surface secondary order parameter or the onset of second-order Josephson coupling. The section on simulations of the $I_c(H)$ patterns (6.3) and the discussion section (6.4) focus on these anomalous junctions.

6.1 Experimental Critical Current Results and Qualitative Discussion

6.1.1 $I_c R_N$ Products

First, though, we begin with $I_c R_N$ products for the full range of directions, since these products contain information about the magnitude of the order parameters of the



superconductors in our junctions. Figure 6.1 shows the $I_c R_N$ products for each direction probed on a semi-circular spider sample, taken at 4.7K. As mentioned in chapter 4, these angles are determined with respect to a Laue x-ray image of the sample substrate.

For comparison, the $I_c R_N$ product for an ideal SIS Josephson tunnel-junction with different order parameters on the two sides is given, in the limit of zero temperature by (Barone 1982)

$$I_c R_N = \frac{\Delta_1 \Delta_2}{\Delta_1 + \Delta_2} K \left(\frac{|\Delta_1 - \Delta_2|}{\Delta_1 + \Delta_2} \right)$$

where the θ 's are measured in terms of gap voltage, and K is the complete elliptic integral of the first kind whose value is $B/2$ for an argument of zero and goes as $\frac{1}{2} \ln(\theta_1/\theta_2)$ as θ_1 becomes large compared to θ_2 . When temperature dependence is included in the above formula, the result for $I_c R_N$ remains approximately unchanged out to 0.4 times the T_c of the lower temperature superconductor and drops gradually to zero between there and T_c . (see (Barone 1982) figure 3.3) Thus, this equation predicts that the $I_c R_N$ product will be a weak function of direction for directions (*i.e.* most directions) where the YBCO gap is greater than the Pb gap, but a linear function of the YBCO gap near 45 degrees where the YBCO gap approaches zero. In either case, the $I_c R_N$ product should be of the order of magnitude of the smaller of the two gaps for each direction.

The actual $I_c R_N$ data of figure 6.1 shows considerable scatter but a significant angle dependence near 45° and 135°. However, the $I_c R_N$ products are of order 60 mV or less, which is more than an order of magnitude less than the gap voltage of either Pb or YBCO in the temperature range near 4 K. In fact, the interpretation of the $I_c R_N$ data is complicated for several reasons, all of which will contribute to understanding the above discrepancies.

First, our junction barrier is not an ideal SIS tunnel barrier, but rather an SNS or possibly SNIS barrier. As described briefly in chapter 3, the main difference between an SNS interface and an SIS interface is that the superconducting pair potential decays into the normal metal with a characteristic length, λ_N . This length, is given by $\lambda_N = (\hbar^2 D_N / 2Bk_B T)^{1/2}$ in the dirty limit (mean free path, $l \ll \lambda_N$) and by $\lambda_N = \hbar v_F / 2Bk_B T$ in the clean limit ($l \gg \lambda_N$), where D_N is the diffusion constant and v_F is the Fermi velocity (Barone 1982; Waldram 1996). It is much

longer, typically of order 1000 \AA , than the decay length into an insulator, typically of order 10 \AA . Since the path length across the interface depends on the angle of transport with respect to the interface normal, there will be an acceptance cone for the Josephson current. Since we don't have detailed knowledge of l , and hence of λ_N , or the decay length of any insulating barrier that might be included in the junction, we don't know the magnitude or width of the acceptance cone, but it will result in a reduction of $I_c R_N$ by averaging over different directions of the YBCO order parameter.

A more significant reduction in I_c , but not R_N (Hilgenkamp 1998) comes from the roughness of the junction. In the context of cuprate grain boundary junctions, they have shown that there can be significant cancellation of the critical current due to the sign changes of the cuprate order parameter sampled by different facets of the interface. They find, in the grain boundary case, that this faceting effect can account for a ten times reduction in J_c as one side of the grain boundary is changed from 0° to 45° with respect to the other, but does not account for the whole 1000 times reduction in J_c they experimentally observed between grain boundary junctions of these orientations. They believe that the rest can be accounted for by band-bending effects giving rise to a depletion layer near the interface. (Mannhart 1998) For small angles, this band-bending effect has already been found sufficient to explain the observed $I_c R_N$ and J_c values (Gurevich 1998), but its effects at larger junction angles are not yet known quantitatively.

Returning to the $I_c R_N$ data of figure 6.1, we see that it is reasonable to expect that roughness effects, which primarily effect the directions probed and band bending, which effect primarily the strength of the Josephson coupling will be sufficient to explain the scatter and the

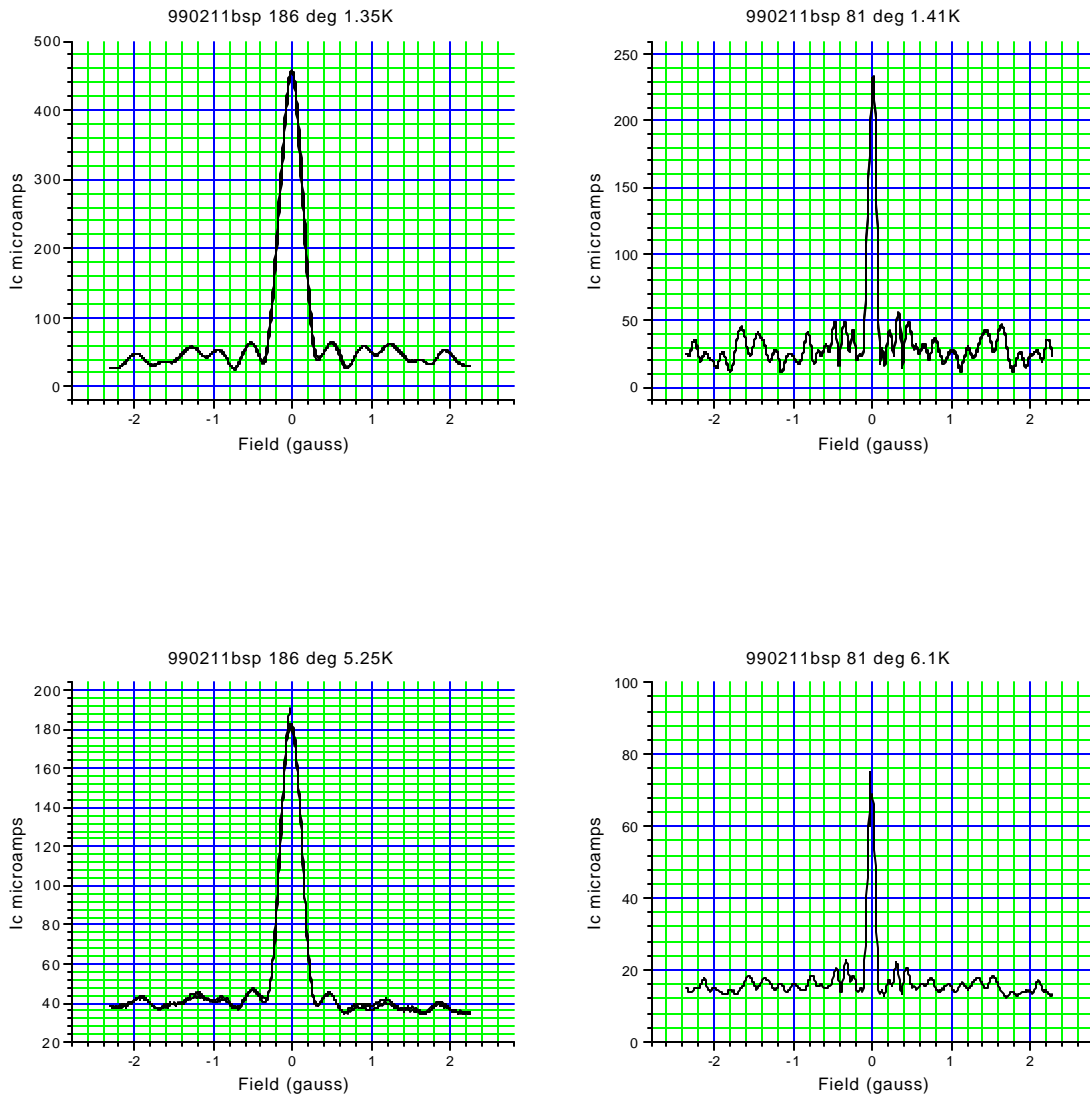


Figure 6.2 $I_c(H)$ pattern for 186/ edge-junction at 1.35 and 5.25 K (left) and for 81/ edge-junction at 1.41 and 6.1 K (right). Note the similarity of shapes at the different temperatures despite the different current scales.

ten to one hundred times reduction of the $I_c R_N$ products below the gap voltages of either Pb or YBCO.

6.1.2 $I_c(H)$ Diffraction Patterns

However, as discussed in section 3.5.2, the key signature of the surface secondary order parameter or second order Josephson coupling we are looking for will be seen in the temperature dependence of the $I_c(H)$ diffraction patterns. The junctions on which the diffraction patterns presented below were taken came from the two best spider samples, a semi-circular sample with 7.5/ junction spacing (990211) and 2/ spaced sample 001127. As in the $I_c R_N$ products, the angles in the a-b plane of the YBCO were calibrated using a Laue x-ray image and were found to be 6/ greater than the nominal edge orientation of the samples would have implied. Figure 6.2 shows $I_c(H)$ data for several temperatures between 1.4K and 7K for junctions on the same sample (990211) as figure 6.1 oriented at 81 and 186 degrees, but from a different run several months later.

The 186/ junction shows an $I_c(H)$ with a large central peak and smoothly varying side lobes with about 10 times smaller magnitude than the central peak and 1/2 the width of the central peak, but with more structure in the side lobes than expected for the ideal Fraunhofer pattern of a uniform junction. The side lobes exhibit excellent reflection symmetry between plus and minus H, indicating that nearby trapped flux or other sources of stray field did not significantly affect this junction. As we did for the corner junctions of the previous section, we attribute the structure of the side lobes to junction roughness from the ~0.3: m grains of the ablated film. The effect of changing the temperature from 1.4 to 6K is just a change in the overall scale of the

001127asp35 137 deg 1.41, 4.04 K

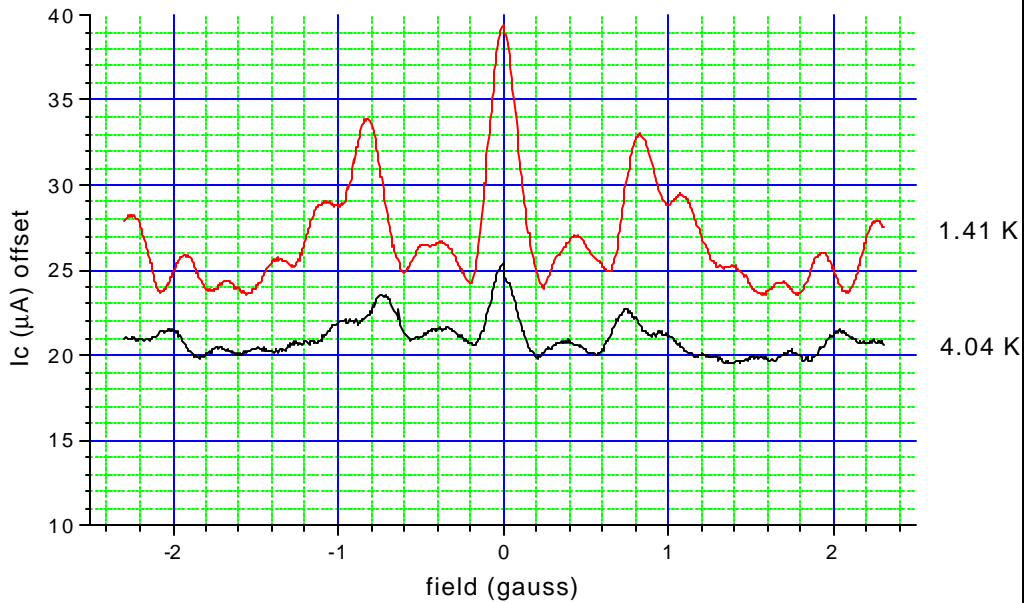


Figure 6.3 $I_c(H)$ data for 137/ edge-junction showing structure in the side lobes less than, but of order the central peak. Note that the overall shape does not change significantly with temperature.

critical current without any significant change in the pattern of the $I_c(H)$ data. The 81 degree junction had similar properties and temperature dependences, although the symmetry of the side lobes, especially the first four on either side, was not perfect. Most of the other junctions tested (not shown) on the two best and most extensively tested samples 990211 and 001127 also

showed similar general shapes and proportional temperature dependences of their $I_c(H)$, summing up to a total of 27 out of 38.

Of the remaining junctions, there were 5 which while retaining an overall proportional temperature dependence and having the zero field peak as the largest in the $I_c(H)$ diffraction pattern had side lobes as large as $\frac{1}{2}$ the size of the central peak. As an example of this, the 137/ junction from sample 001127 is shown in figure 6.3. This is what one would expect for a rough junction to a d_{x2-y2} oriented near 45° , since the critical current density, $J_c(y)$, of such a junction will sample many facets with opposing signs of the order parameter, but on average will have more of one than the other. Thus $J_c(y)$ would be represented by a constant plus a sum of oscillating terms of comparable but smaller magnitude. This is exactly what a Fourier transform, $I_c(H)$ with side lobes comparable to, but smaller than the central peak signifies. In fact, there was also a junction (143/ on 001127, not shown) whose $I_c(H)$ had a an overall proportional temperature dependence, and whose central peak was much smaller than its side lobes, as one would expect for a junction near 45° with roughly equal numbers of plus and minus facets occurring by random chance. Summing up, we thus see that 33/38 junctions tested on these two samples had $I_c(H)$ patterns and temperature dependences which were explainable strictly in terms of the known d_{x2-y2} order parameter symmetry of YBCO.

However, some of the junctions oriented within 15° or so of the 45° directions showed significant differences both in the structure of their $I_c(H)$ patterns and in their temperature dependences, which point to the need for further explanation. The junctions

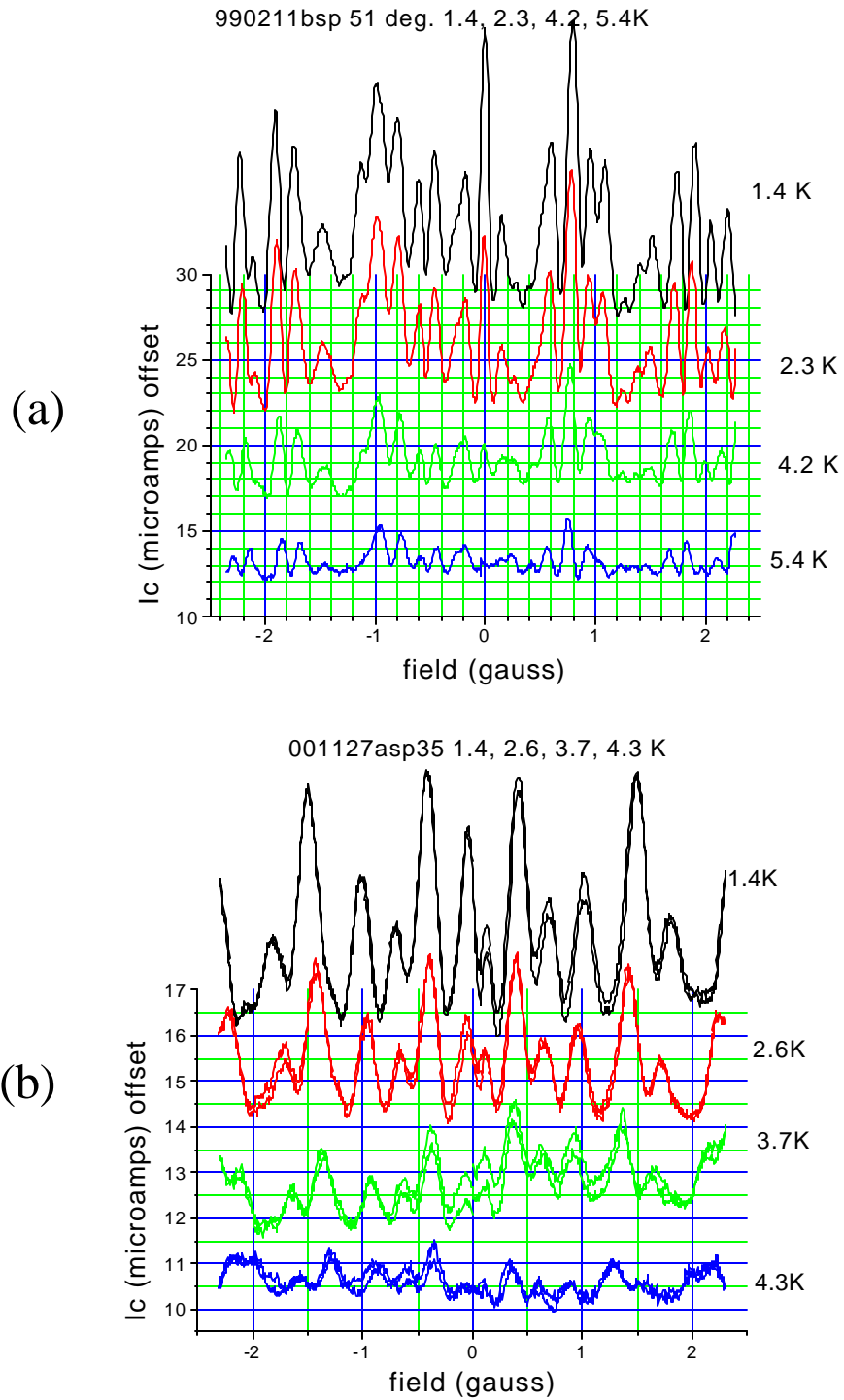
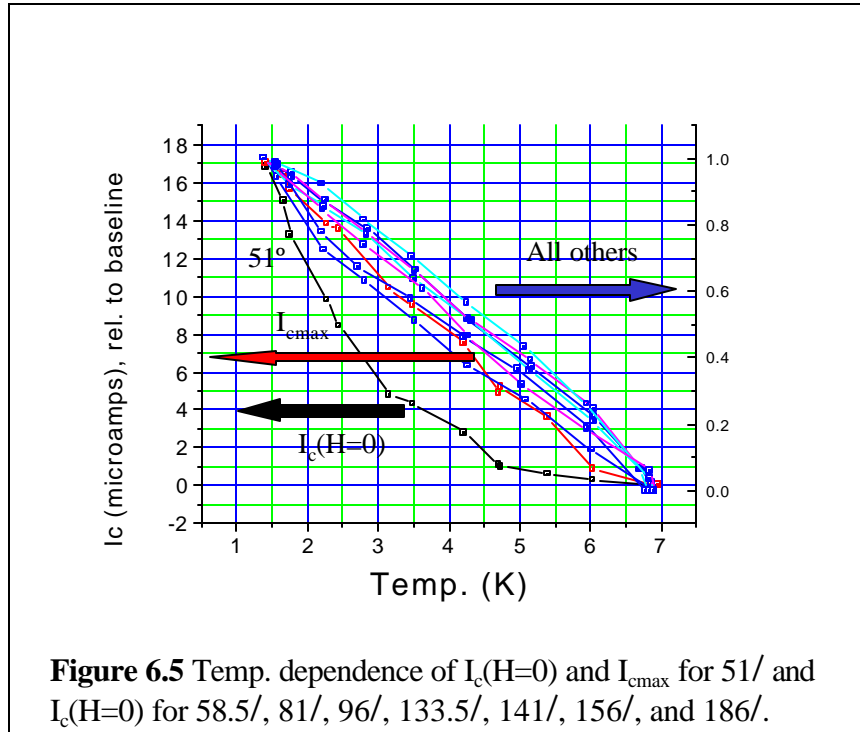


Figure 6.4 $I_c(H)$ for the 51/ (a) and 43/ (b) junctions discussed in the text at a range of temperatures. Both show anomalous increases in I_c near $H=0$, but (b)'s increase is off-center.

with the most dramatic such differences were oriented at 51 and 43 degrees and came from 990211 and 001127 respectively. The key properties of these junctions, in particular the temperature dependence of I_c near zero applied field, were repeatable on many different runs, some taken as much as several months apart.

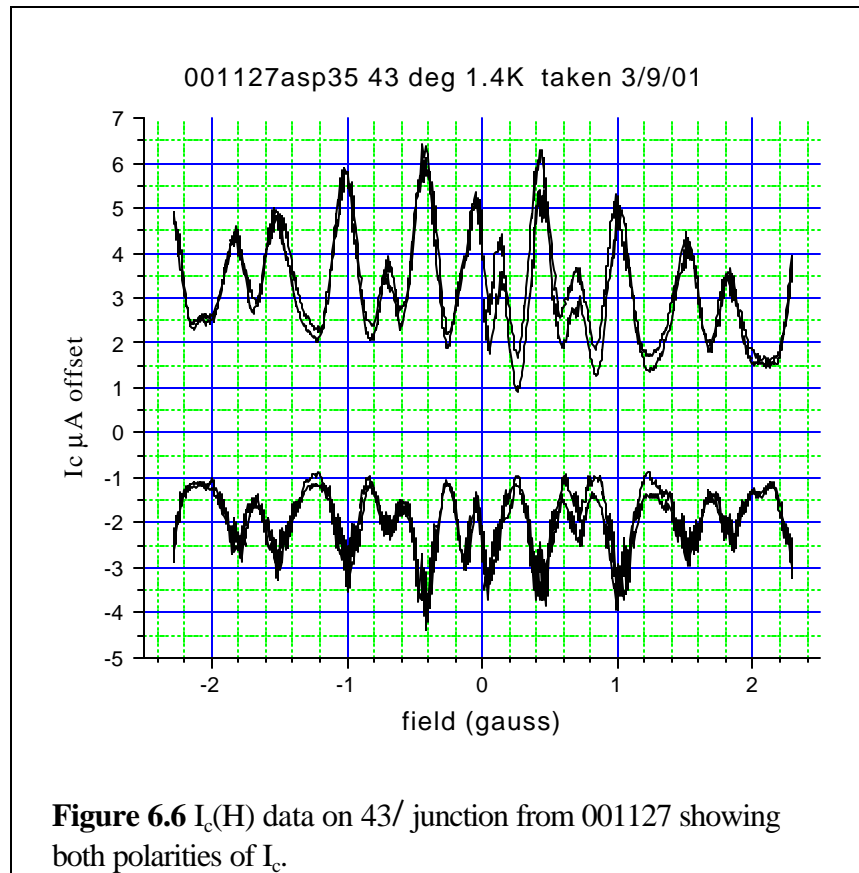
The $I_c(H)$ for several different temperatures in the range 1.4 to 6K of the 51/ and 43/ junctions are shown in figure 6.4 (a) and (b) respectively. For the 51/ junction at 5.4K, we observe a negligible critical current at zero applied field and a pattern in the side lobes in $I_c(H)$ which is not symmetric in magnitude under $H \leftrightarrow -H$, but does at least have a correspondence of peak locations between the plus and minus H sides. The pattern of these side lobes was repeatable even after several heatings and coolings above both the Pb/In and YBCO T_c 's during the same set of runs and their heights remained roughly proportional through the temperature range below the Pb/In T_c . Thus, although the broken symmetry between $\pm H$ most likely indicates the presence of a preferential arrangement of trapped flux near this junction, the repeatability and proportionality of this side-lobe pattern can still allow it to serve as a baseline for comparing the changes in $I_c(H)$ near $H = 0$.

In fact, as the temperature of this 51/ junction was lowered toward 1.4 K, a dramatic rise in the zero field critical current was observed starting at about 4.5 K. This rise in the zero field peak was in sharp contrast to both the side lobes of the same pattern and the overall patterns of junctions away from 45/, such as those in figure 6.2. This contrast can be seen again in figure 6.5, which shows a plot versus temperature of the zero field critical current of the 51/ junction, its largest side lobe and the zero field critical currents of the 186/ junction and others



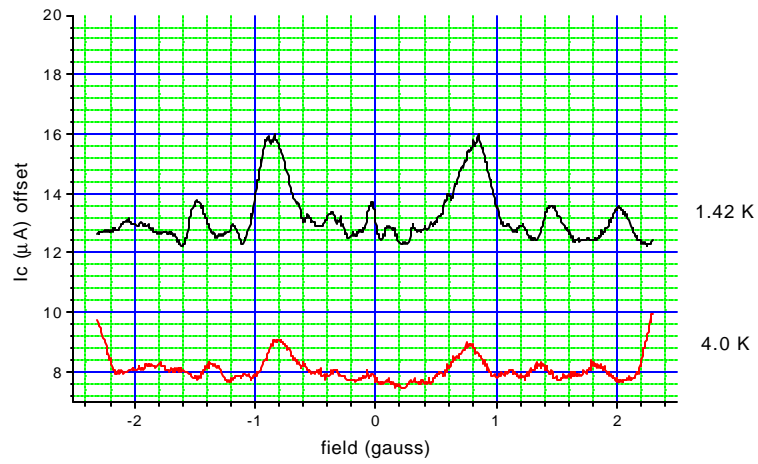
from sample 990211, all normalized to their 1.4 K values. Here, we see the change in slope of the 51/ zero field I_c at about 4.5 K as contrasted with the smooth, roughly linear, increase of I_c starting at the Pb/In T_c of 6.95 K for all the other peaks plotted. Note also that the rising zero-field peak in figure 6.4 is narrower than the other large peaks in the pattern by a factor of about 0.5 to 0.7, measured by the full width at half maximum (FWHM).

The $I_c(H)$ near $H=0$ for the 43/ junction in figure 6.4(b) shows a similar onset starting near 4 K, but in this case, the peak that develops is the first peak to the left from $H=0$. The side lobes of this pattern away from the center two exhibit excellent symmetry between H and $-H$, indicating very little, if any, trapped flux in this junction. The asymmetric rise in the first side peak away from the center could be explained by the onset of a possible secondary order parameter with two domains, but could also be the result of a self-field effect, as will be



discussed in the quantitative analysis section (6.3) below. To distinguish between these two explanations, this junction was re-measured in a later run (about 3 months later) where both the positive, $I_{c\max}(H)$, and negative values, $I_{c\text{negmin}}(H)$, were measured in the same cooldown by reversing both the current and voltage leads to the sample insert between runs with the analog feedback technique (see section 4.2.2). The data from this procedure are shown in figure 6.6 and are approximately inversion symmetric under $I_c \rightarrow -I_c$ and $H \rightarrow -H$, but not mirror symmetric under either of these operations separately, and hence favor the self-field explanation (see section 6.3 below.) Finally in this section, we show two junctions which had more subtle, but still measurable changes in the shape of their $I_c(H)$ patterns as their temperatures were lowered.

001127asp35 141 deg 1.42 and 4.0 K



001127asp35 139 deg 1.41 and 4.1 K

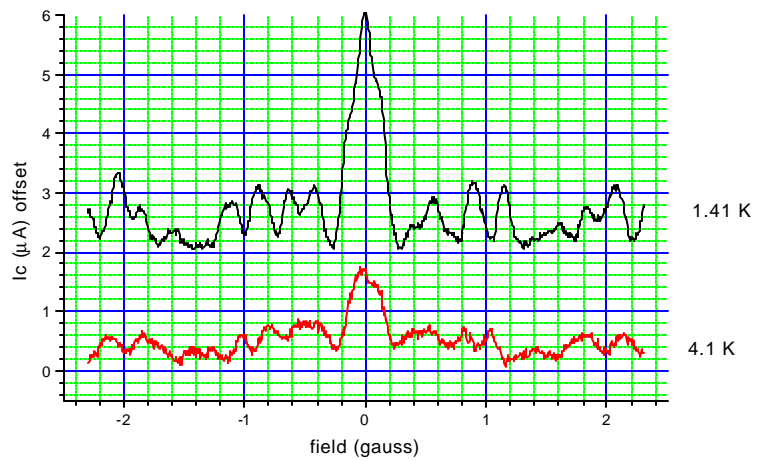


Figure 6.7 $I_c(H)$ patterns at 1.4 and 4 K for junctions at 139/ and 141/ showing the emergence of a narrow peak near $H=0$.

The junctions at 141 (figure 6.7(a)) on sample 001127 (same sample as the 43/ junction in figure 6.4(b) above) shows the growth of a zero field peak with about half the width of the side lobe peaks on cooling from 4.0 to 1.4 K, but with a much smaller height than the side lobe peaks. The 139/ (figure 6.7(b)) junction shows a narrower peak superposed on top of a base center peak at 1.4 K. The base center peak is twice as wide as the side lobes at 1.4 K, but at 4 K, the side lobes are not well resolved. There is a good correspondence between the side lobes at $\pm H$ in these two junctions, but not quantitative symmetry, probably indicating some residual stray field from trapped flux.

6.2 Dynamic Conductance Data (dI/dV)

To obtain a more direct comparison of our junctions with previous experimental tests for a possible secondary order parameter we also took conductance spectroscopy (dI/dV) on our junctions at temperatures from 1.4 K to 6.6K. The dI/dV data in the voltage range of ± 10 mV for temperatures ranging from 1.4 to 5.6 K for the 51/ junction of sample 990211 ($I_c(H)$ shown in figure 6.4(a)) is shown in figure 6.8. Positive voltage in the plots corresponds to positive bias of the Pb side of the junction. Conductance data from other junctions are similar but are not shown. We restricted the voltage range to ± 10 mV to avoid excessive sample heating. The negative spike at -10 mV is an artifact due to a zero crossing anomaly in the current source as described in section 4.3.

The data show a peak at zero bias with a width (HWHM) that varies from 1.3mV at 1.4 K to 2.4mV at 6.6K, as plotted in figure 6.9(a). In the middle of the zero bias peak is a

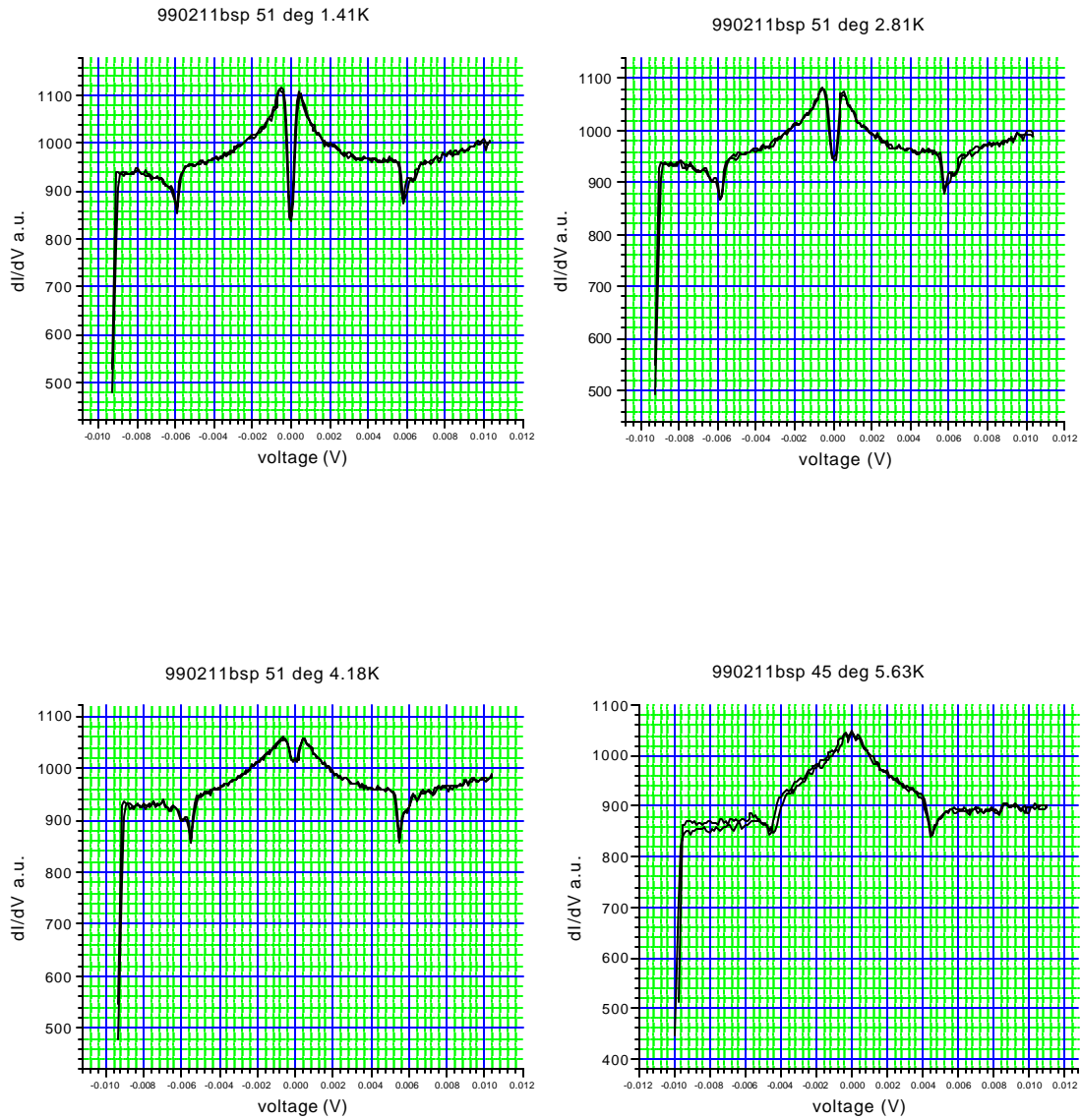


Figure 6.8 dI/dV data on the 51/ junction of 990211 at 1.41, 2.81, 4.18, and 5.63 K. The negative spikes on the left are artifacts.

gap-like dip feature due to the Pb order parameter proximity-coupled through the Ag layer.

The width of this dip is relatively insensitive to temperature while its area drops monotonically to zero as T is increased from 1.4 to about 6 K. On each side of the zero bias conductance peak are additional symmetrically located dips which shrink and move inward in voltage as the temperature is increased. The locations of the side dips are plotted versus temperature in figure 6.9(b). It is particularly interesting to note that the location of the side dips follows approximately a BCS gap temperature dependence plus a constant. This behavior is consistent with a phonon tunneling signature since such a signature should be located at the Pb gap energy plus a characteristic phonon energy (Scalapino 1966) and Pb has a transverse phonon signature at 4.2meV; adding in the Pb gap energy of 1.4 meV gives 5.6meV, which is reasonable close to 5.85mV, the lowest temperature location of our side dips. However, we have not investigated other possible explanations for the side-dip features.

Since we don't know whether our Pb(In)/Ag/YBCO junctions are really SNS, SNIS, or have some more complicated barrier, we can't necessarily equate our dI/dV data directly to the tunneling density of states as one would expect from a textbook analysis, *e.g.* (Tinkham 1996) (see also section 2.4 above). A standard technique to evaluate the amount of elastic tunneling in a junction is to observe a well formed gap at the correct energy for one of the superconductors, in our case Pb(In). (See for example (Covington 1997c).) If the Pb(In) is not well formed, or is at a lower energy than ideal, then the transport in the junction is mostly by inelastic processes and the tunneling density of

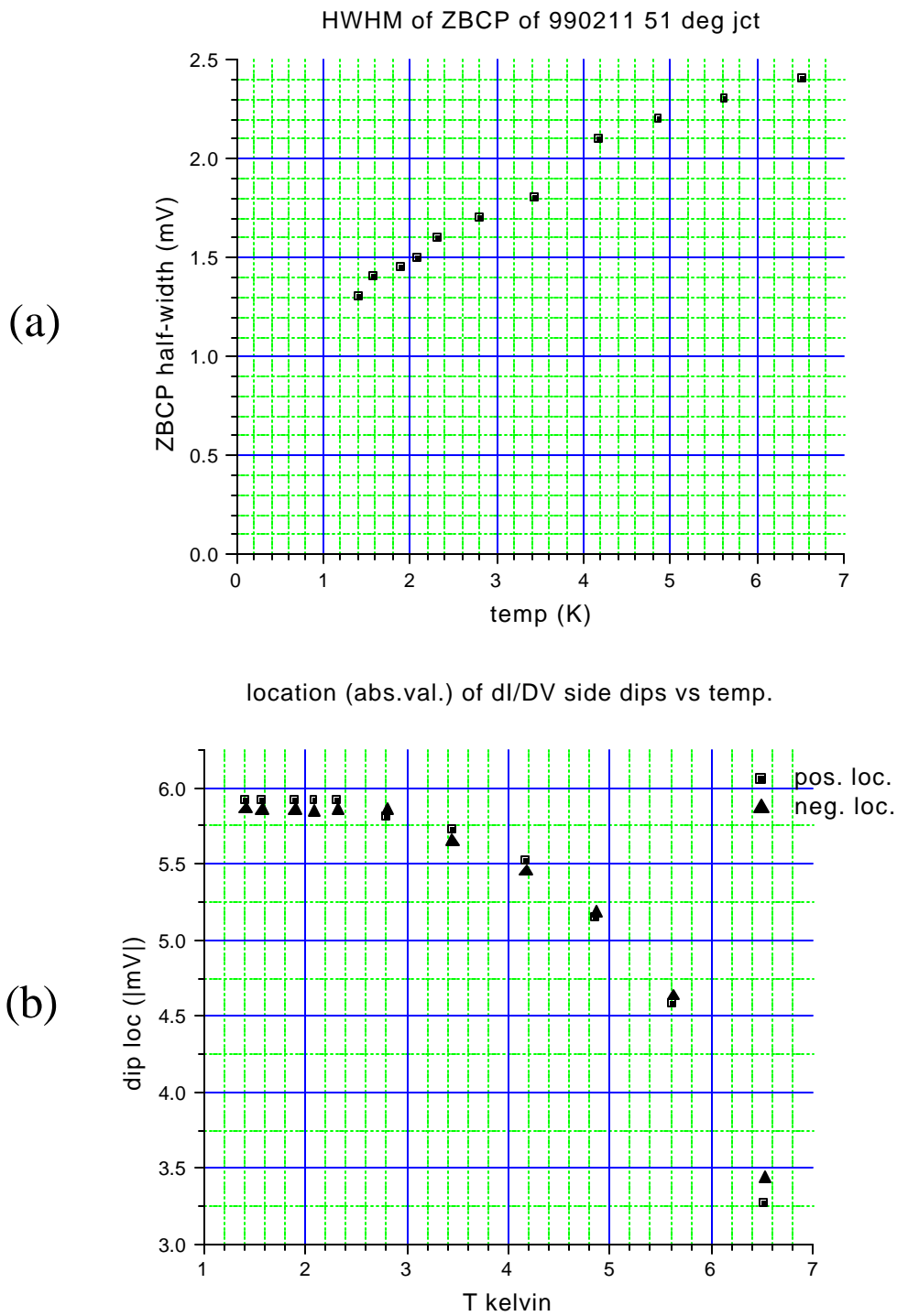


Figure 6.9 (a) Half width at half max vs temp. of the zero bias conductance peak from the 51/ junction of sample 990211. (b) Location vs temp. of the side dips in the conductance spectrum for this sample.

states information will be smeared. Since we don't know how much proximity reduction of the Pb(In) gap is caused by the Ag in our junctions, we cannot directly evaluate the amount of elastic tunneling in our junctions. However, even in a smeared density of states, a ZBCP must reflect a ZBCP in the true density of states because there it is not expected that any smearing function could create a ZBCP from a concave upward density of states at zero bias.

The overall conclusion of these conductance measurements is that we are observing the zero bias peak in the density of states expected (Hu 1994; Fogelstrom 1997a) for a non-(100) surface or any rough surface of a $d_{x^2-y^2}$ superconductor. Hence the spectral weight of this zero bias peak is available for possible secondary pairing near the surface. On the other hand, the presence of the gap-like feature from the Pb/Ag proximity layer obscures any possible splitting of the zero-bias peak, so a direct comparison with the low-temperature splitting seen in (Covington 1997a) and attributed to secondary pairing is not possible.

6.3 Realistic Quantitative Simulations and Comparison

In this section we will present and discuss simulations of the changes in $I_c(H)$ corresponding to changes in $J_c(y)$ expected in the cases of the onset of a secondary order parameter or second-order Josephson coupling for junctions with realistic faceting. We will defer to the next section a discussion of the overall plausibility of these two mechanisms, as well as others, to explain the anomalous temperature dependences seen in the $I_c(H)$ data for some of our junctions. Since the junctions near to 45/ for which the

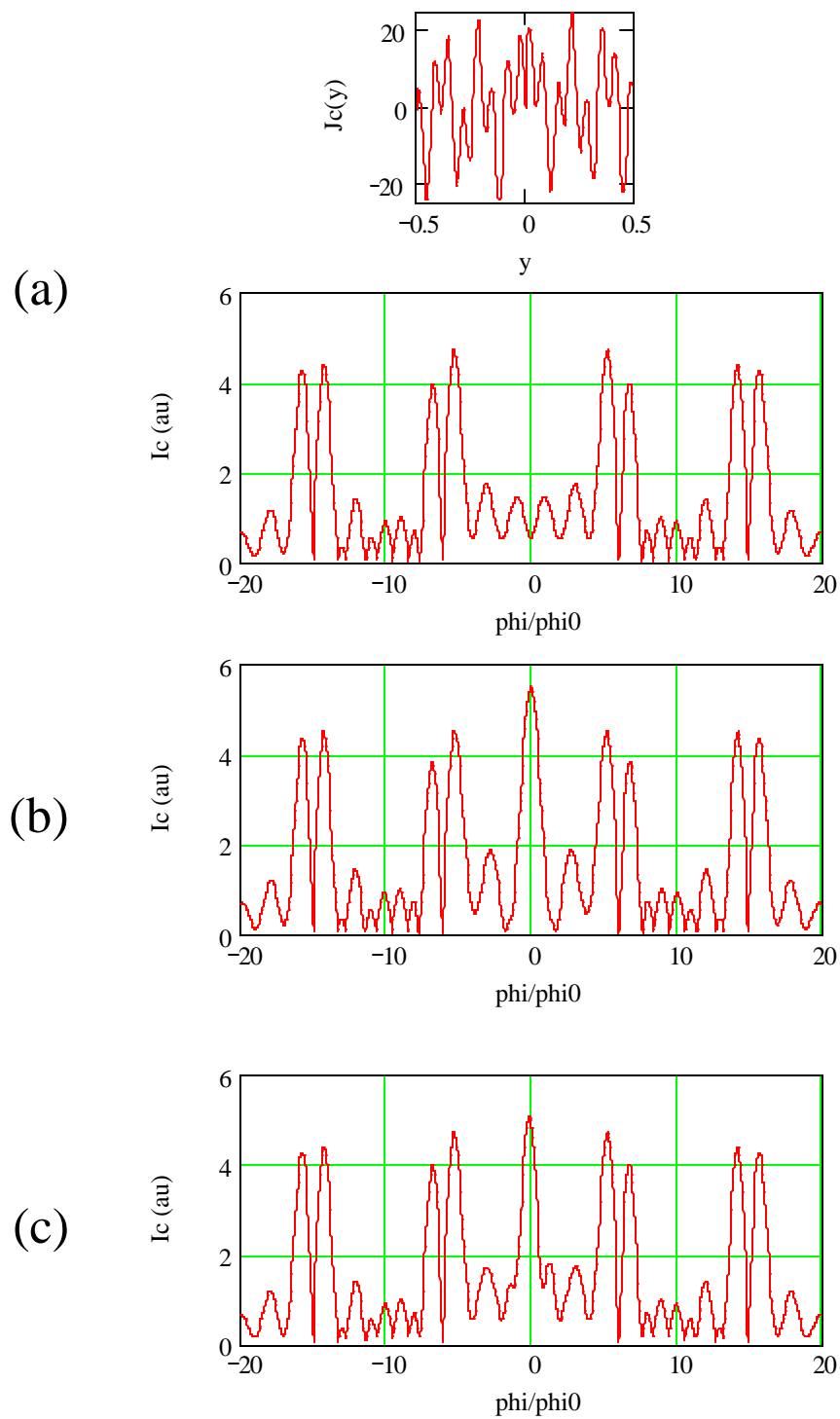


Figure 6.10 Simulated $I_c(M)$ for the current distribution $J_c(y)$ shown at top assuming a pure $d_{x^2-y^2}$ order parameter (a), $d + (5/12)s$ (b), and $d + (5i/12s)$ (c).

non-trivial temperature dependence of the $I_c(H)$ occurred were expected to have many sign changes in their $J_c(y)$ profile, we did not attempt to use the algorithm of Vartanians and Robinson (see section 5.1.2) on them, but resorted instead to assuming a $J_c(y)$ based on physical intuition, Fourier transforming the $J_c(y)$, and making a qualitative comparison to the $I_c(H)$ data. Thus the analysis of this section is essentially a demonstration of how in principle the important features of our data can be produced rather than a rigorous fit to the data.

We begin by finding a $J_c(y)$ distribution with sign and magnitude variations which will give an $I_c(H)$ similar to the high temperature limit (*i. e.* $>4K$) of the experimental data. One such $J_c(y)$ and its corresponding $I_c(H)$ is shown in figure 6.10 (a). The functional form of $J_c(y)$ chosen here is

$$J_c(y) = \text{sgn}(y)(\sin(2B*6y) + \sin(2B*15y)), -0.5 \# y \# 0.5,$$

which was chosen to create large side lobe doublets on either side of $I_c(H)$ and a number of smaller features in between. Adding a uniform secondary s-wave order parameter to this model junction would correspond to adding a constant, J_s , to $J_c(y)$. The effect this on $I_c(H)$ for the constants $J_s = 5/12$ and $J_s = 5i/12$ is shown in figure 6.10 (b) and (c). Similarly to the ideal case shown in figure 3.12, the addition of J_s causes a dramatic rise in $I_c(H=0)$ and a small effect on the first side lobes, but negligible effect on $I_c(H)$ further out. Also similar to the ideal case from figure 3.12, the mirror symmetry of $I_c(H)$ is broken when J_s has an imaginary component, although in the present case, the symmetry breaking is seen primarily in the first side lobes rather than in a shift of the central peak. Since this $\pm H$ mirror symmetry breaking is subtle and affects only the first side lobes, it

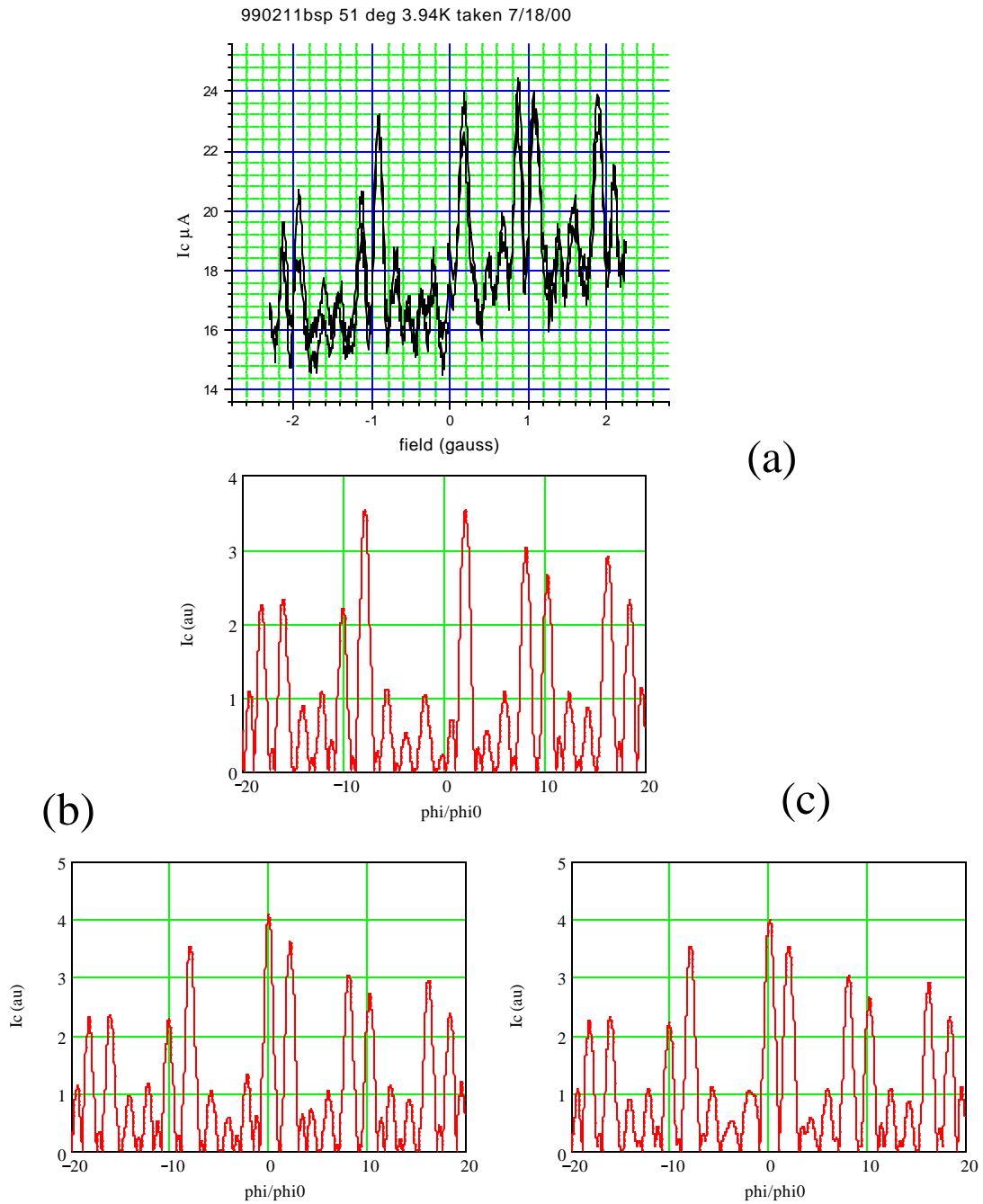


Figure 6.11 (a) Detailed model $I_c(M)$ chosen to reflect the major features of experimental data (top) on the 51/ junction. The effect of adding a real (b) or complex (c) mixture of s-wave order parameter is shown at bottom.

would be difficult to distinguish between a real and a complex addition of J_s in of our experimental $I_c(H)$ data.

Now a closer fit to the side lobes of our actual data can be obtained including terms of more different frequencies in $J_c(y)$ as shown in figure 6.11 (a) with data from the 51/ junction of 990211 for comparison. Note that these data were taken three months before the data on the same junction shown in figure 6.4(a). While the side lobe pattern is different, the rise of the zero field peak as the temperature is lowered to 1.4 K (not shown) is about the same.

The model $J_c(y)$ in figure 6.11 is made up of a sum of complex exponentials with equal and opposite frequencies $\pm k$ and real coefficients. If the coefficients for $\pm k$ are equal, then they just add to a real cosine component in $J_c(y)$, whereas if they are unequal, the difference in coefficients represents the phase term from a model stray magnetic field and spatial frequency k . As is seen in figure 6.11 (b) and (c) adding a current J_s due to a secondary order parameter in a real or complex superposition affects the central peak and first side lobes in much the same way as the simpler model system shown in figure 6.10.

Since the central peaks in some of our junctions' $I_c(H)$ were narrower than the side lobes in these junctions, we were motivated to consider the possibility of the onset of second-order Josephson coupling, for which the DC Josephson equation becomes

$$J = J_c \sin 2 \phi$$

As discussed in chapter 3, (Tanaka 1994) has predicted this possibility of second order Josephson coupling between an s-wave and a $d_{x^2-y^2}$ superconductor for a junction

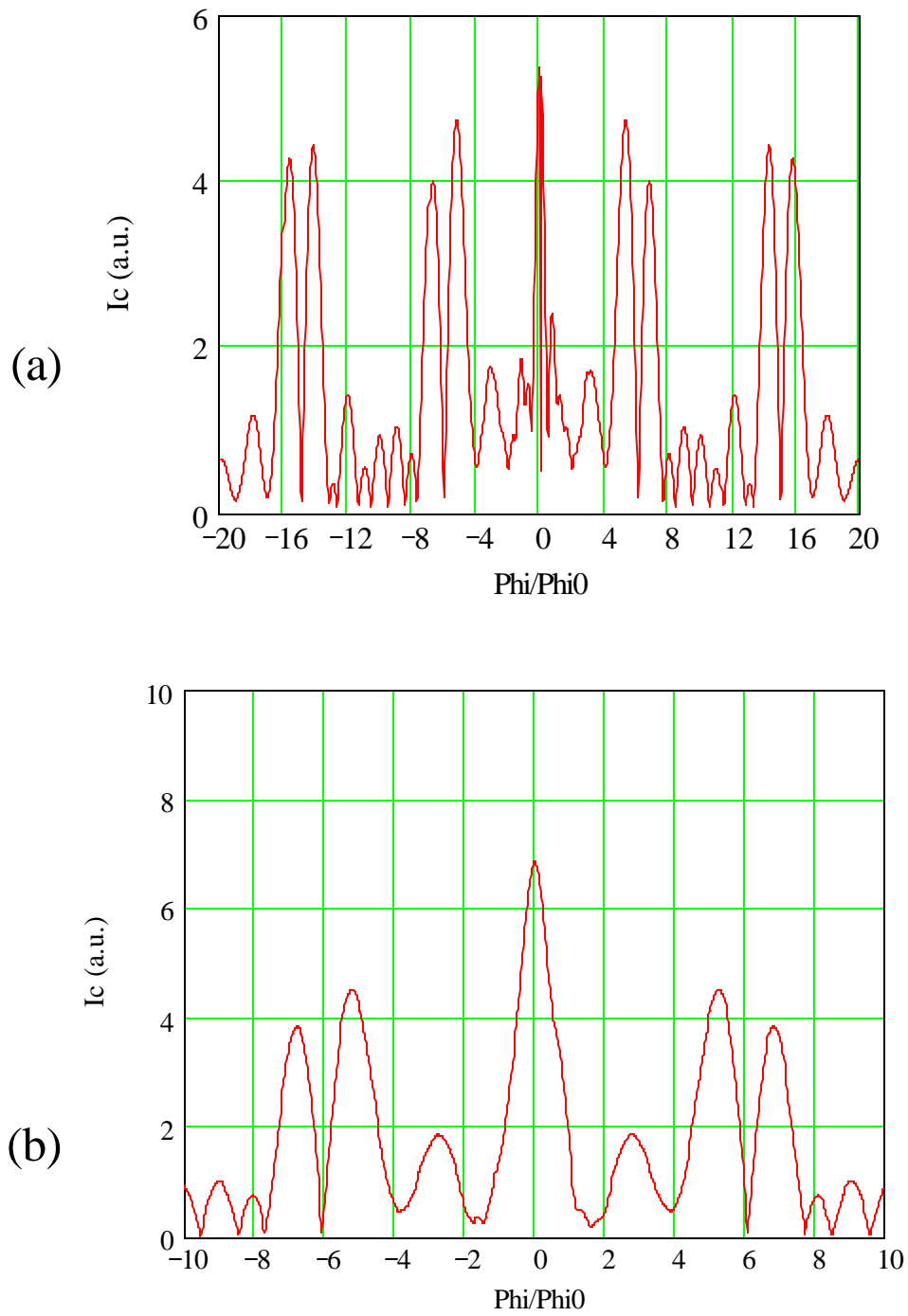


Figure 6.12 $I_c(M)$ calculations for the model system of figure 6.10 with the addition of a uniform second-order coupling term (a) and with the addition of uniform first and second order coupling terms in the ratio 2:1 (b).

oriented at 45° with respect to the $d_{x^2-y^2}$ superconductor. For an ideal flat 45° interface, second order Josephson coupling gives an $I_c(H)$ with the ideal Fraunhofer form, but narrower by a factor of 2 in H . For our experimental case of a faceted junction near 45° we would expect the first and second order Josephson currents to act as parallel channels driven by the same gauge invariant phase difference, ϕ . Since the overall current-phase relation for the junction is no longer sinusoidal, the $I_c(H)$ can no longer be calculated simply by taking the magnitude of the Fourier transform of the critical current density. Rather, the total Josephson current must be found and maximized separately for each field value with respect to an overall phase of the junction, \mathbf{N} . This total current is of the form

$$I(H, \mathbf{N}) = I_1(H)\sin(\mathbf{N} + \phi_1(H)) + I_2(H)\sin(2(\mathbf{N} + \phi_2(H))),$$

where the subscripts 1 and 2 denote the first and second-order contributions. Since in general ϕ_1 and ϕ_2 are different, the positive and negative extrema of $I(H, \mathbf{N})$ need not be the same magnitude. However, if the spatial current densities of the first and second order contributions are real, $\text{Max}[I(H, \mathbf{N})]$ will equal $-\text{Min}[I(-H, \mathbf{N})]$ and hence inversion symmetry of $I_c(H)$ will be preserved.

Adding a uniform distribution of second-order Josephson current to the model first-order current distribution from figure 6.10 and performing the current maximization at each field value, one finds the $I_c(H)$ shown in figure 6.12(a), which has a central peak half the width of its major side lobes. The addition of a uniform first and second-order Josephson current on the same initial model from figure 6.10 with a ratio of J_c 's of 2:1 is shown in figure 6.12(b) a possible model for the 139° junction from sample 001127. These two model calculations do a

good job of simulating the narrow features at $H=0$ of the 51/ junction from 990211 and the 139/ junction from 001127 respectively.

Lastly in this subsection, we consider possible models to simulate the 43/ junction on sample 001127 (see figure 6.4(b)), which had an asymmetric increase in its first side lobe as the temperature was lowered from 5 to 1.4 K. One possible model for this behavior of the junction is the onset of a secondary order parameter with two domains of roughly equal size, but different complex superpositions of the primary $d_{x^2-y^2}$ and secondary s-wave order parameter. Figure 6.13 (a) and (b) shows the model system from figure 6.10 with and without a superposition of $0.5i$ s in the right half of the junction and $-0.5i$ s in the left half of the junction. However, as mentioned above in section 5.1.1, any (first-order) Josephson junction has $\pm I_c$ mirror symmetry for any given applied H because the supercurrent at all points can be reversed by adding a phase offset of \mathbf{B} to each points sinusoidal current-phase relation. This $\pm I_c$ mirror symmetry is true even for junctions with complex order parameters or junctions in the presence of stray fields where $\pm H$ mirror symmetry is broken, so long as self-field effects or higher order Josephson coupling (which causes a non-sinusoidal current-phase relation) are not significant.

On the other hand, a junction with self-field effects can break $\pm I_c$ mirror symmetry at any finite H because the self-fields from $+I_c$ will add to the applied H with the opposite sign than those from $-I_c$. Further, if the junction with self-field effects has a real order parameter on both sides, and hence a real $J_c(y)$, and has no trapped flux or other sources of stray field, then its $I_c(H)$ will be symmetric under time reversal, which corresponds to $I \leftrightarrow -I$ and $H \leftrightarrow -H$.

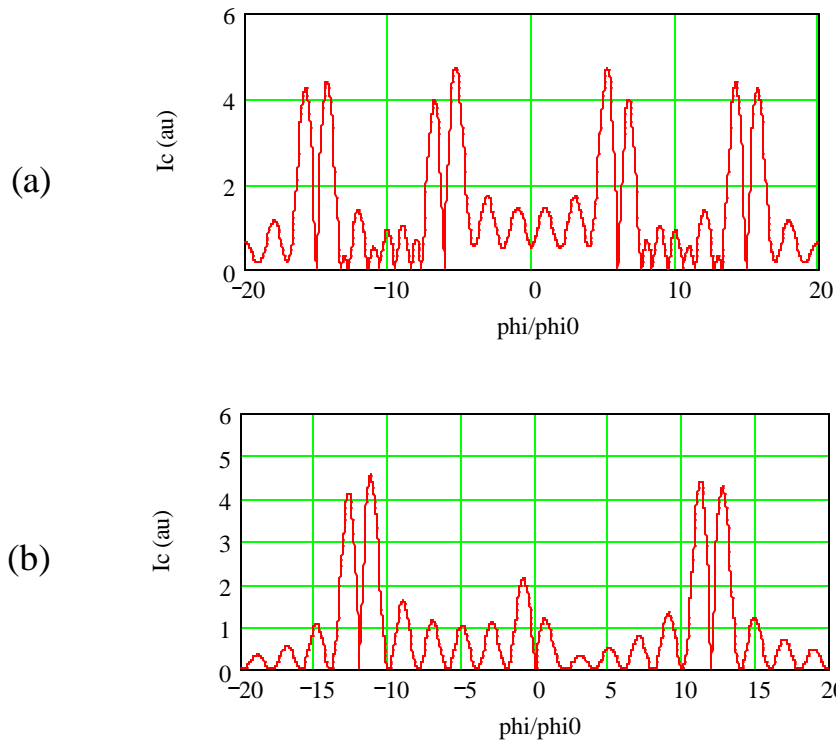


Figure 6.13 (a) $I_c(M)$ for model system from figure 6.9. (b) Same model system with admixture of a two domain (i/6)s order parameter component.

Since, this inversion symmetry is what is in fact observed for the 43/ junction, it follows that the low temperature increase of the first side lobe in its $I_c(H)$ is better explained as a self-field effect.

6.4 Discussion

As noted above in section 6.2, the $I_c(H)$ measurements of the majority of the edge junctions tested (33/38) were explainable strictly in terms of the known $d_{x^2-y^2}$ order parameter of YBCO. Of the remaining five, three (two shown) had narrow central peaks (about $\frac{1}{2}$ the width of the other major peaks in the $I_c(H)$), which increased in height relative to the rest of the

pattern, with the 51/ junction from 990211 showing by far the largest increase of the three. One junction, 139/ from 001127 had narrow central peak superposed on top of a broad central peak, and one 43/ from 001127 had one of its first side-lobes increase relative to the rest of the pattern as the temperature was lowered. It is the behavior of these 5 junctions which will require factors in addition to the $d_{x^2-y^2}$ order parameter of YBCO in their explanation, and on which the remainder of this subsection will focus.

The realistic simulations of the previous section showed that the rise of a central peak in $I_c(H)$ as the temperature is lowered could be explained by the onset of a surface order parameter in a real or complex superposition with the primary $d_{x^2-y^2}$ order parameter, or by the onset of second order Josephson coupling, while the rise of a side lobe peak could be explained by a two-domain secondary order parameter or by self-field effects.

To evaluate the plausibility of the surface secondary order parameter explanation, we consider together both the conductance data, dI/dV , and the diffraction pattern data $I_c(H)$ for all junctions measured. Now, in the presence of interface roughness, it has been calculated (Fogelstrom 1997a) that the suppression of the $d_{x^2-y^2}$ order parameter which leads to the zero bias conductance peak will occur for all interface directions and will have much less orientation dependence than for ideal smooth interfaces. This prediction is consistent with our conductance data in that all orientations we measured, ranging from 0 to 90 degrees, show about the same height, shape and temperature dependence of the zero bias conductance peak. Thus if the proposed secondary order parameter acts on the available spectral weight in the

zero bias peak, we would expect to see evidence of it in most or all of our junctions rather than only a few.

It might be that the relative rarity of the $I_c(H)$ signature (*i.e.* the rise in the central peak relative to the other peaks) for the secondary surface order parameter is due to sensitivity of the secondary order parameter to the detailed boundary conditions of each individual junction. If this explanation is true, it would seem to require an unconventional symmetry for the secondary order parameter, such as d_{xy} , because the conventional phonon-mediated s-wave superconducting state is known to be relatively insensitive to both impurities and boundary scattering (Anderson 1959). On the other hand, it might be the $I_c(H)$ signature for the secondary order parameter is obscured by the large central peaks already present in most of the junctions. Of course this would still require the secondary order parameter to be sufficiently small to escape notice.

Besides the rarity of observation of the $I_c(H)$ signature, the secondary order parameter explanation must also contend with the narrowness of the central peak in most of the cases where an anomalous low temperature rise of the central peak is seen. This is what led us to consider instead the possibility of an onset of second-order Josephson coupling. If true, this explanation could explain both the relative rarity of the $I_c(H)$ signature in question and its temperature dependence when it does occur, since the second order coupling term is sensitive to both the barrier strength and the temperature with a higher power law than the first order coupling term (Tanaka 1994). Furthermore, the second-order Josephson coupling explanation of our data would provide complementary evidence to recent current phase measurements of

YBCO grain boundary junctions (Il'ichev 1998; Il'ichev 2000) which have been argued to show a component of second order coupling. A useful cross-check on the second-order coupling explanation can be obtained by measuring Shapiro steps (steps in the I/V plots in the presence of microwave radiation) on the junctions with the narrow central peaks which are predicted (Tanaka 1994; Zhang 1995) to occur in voltage steps of $h/4e$ rather than the usual $h/2e$ when there is significant second order coupling in a junction. The author plans to attempt these measurements in the course of submitting this work for publication.

Two other possible explanations for the junctions with anomalous low temperature $I_c(H)$ behavior were also considered, but are now thought to be unlikely for the reasons stated below. The first such explanation is the opening of a physically separate conducting channel at the temperatures in question. However the dI/dV data show no significant change in the background conductivity, away from the zero bias peak and side dips, over the temperature range of greatest change in $I_c(H)$ as one would expect for a new conducting channel. The other explanation considered was that a secondary order parameter near the surface of the YBCO might come not from a pairing mechanism intrinsic to the YBCO, but from proximity coupling to the Pb. This would be similar to the theoretically predicted proximity induced Josephson effect (Thuneberg 1988; Wolf 1989). However, this explanation suffers from its inability to account for a truly independent phase of the proximity-induced order parameter from the Pb order parameter and hence an inability to account for a true contribution to the DC Josephson current (Kadin 1990)(D. Sheehy, private communication).

Chapter 7

SUMMARY AND FUTURE DIRECTIONS

In this thesis, Pb/Ag/YBCO ramp-edge Josephson junctions have been investigated in corner and straight edge geometries of various orientations in order to probe the details of the direction dependence of and possible surface effects on the YBCO order parameter. To this end, measurements of the critical current as a function of field, $I_c(H)$, and dynamic conductance, dI/dV , have been made in the temperature range 1.4 to 7 K, the Pb T_c . For comparison, model simulations of $I_c(H)$ have also been carried out.

The corner junction $I_c(H)$ results were consistent with the previously known $d_{x^2-y^2}$ bulk order parameter. The differences from the ideal $I_c(H)$'s for these junctions were attributable to non-uniformities in the supercurrent density due to junction roughness on the scale of $0.3 \mu\text{m}$.

For the straight-edge junctions, the $I_c(H)$ data for most junctions was consistent with the known bulk $d_{x^2-y^2}$ order parameter of YBCO. Junctions far from the YBCO (110) direction had a Fraunhofer-like $I_c(H)$ with a large central peak and much smaller side lobes, while junctions closer to the (110) direction had more structure in the side lobes of $I_c(H)$ with some side lobes approaching the central peak in magnitude. Dynamic conductance, dI/dV , data for all the junctions measured showed a zero bias conductance peak (ZBCP), consistent with the predictions for a d-wave order parameter near a rough surface.

However, some junctions near the (110) direction had an anomalous increase in $I_c(H)$ near $H = 0$ as the temperature was lowered. The principle explanations considered for these

junctions were the onset of a secondary order parameter and the onset of second-order Josephson coupling. While the rise of a zero field peak in $I_c(H)$ is qualitatively consistent with the expected signature for the onset of a secondary order parameter, the width of the zero field peak seen experimentally is in all but one of these anomalous cases only about $\frac{1}{2}$ that predicted by the secondary order parameter model. These cases are better explained by the onset of second-order Josephson coupling, which naturally predicts a central peak $\frac{1}{2}$ as wide as the other peaks in the $I_c(H)$ pattern. In the other case, the $I_c(H)$ peak that rises faster than the rest of the pattern is off center and the overall pattern exhibits inversion symmetry rather than $\pm I_c$ mirror symmetry as the secondary order parameter model would predict. This case is better explained by self-field effects in the junction.

In the short term, there are two main directions to be pursued in following up on this project. One is to make Shapiro step measurements on the junctions which exhibited the anomalous low-temperature increases in their zero field $I_c(H)$ patterns to check for the expected $h/4e$ step size predicted for second-order Josephson coupling. The other is to continue work on the iterative calculations discussed in section 5.1.2 for estimating the critical current density $J_c(y)$ from $I_c(H)$ in the hope of better understanding their range of validity for characterizing the corner junction experiments of this thesis and other similar junction experiments.

In the longer term there are many ways that the work of this thesis might be extended, only two of which I will mention here. First it would be desirable to attempt to make ramp junctions starting from cuprate films which don't suffer from the same degree of graininess as

the films of this thesis. This might involve either a more systematic optimization of the YBCO laser ablation process used in this thesis, or the procurement of films grown by other techniques, such as molecular beam epitaxy (MBE). Second, it would be desirable to attempt a direct measurement of the current-phase of the junctions from this thesis or similar junctions in the hope of finding complimentary evidence for second-order Josephson coupling.

REFERENCES

- Anderson, P. W. (1959). Journal of Physical Chemistry of Solids **11**: 26.
- Annett, J. F., N. Goldenfeld and S. R. Renn (1990). The Pairing State of $\text{YBa}_2\text{Cu}_3\text{O}_{7-x}$. Physical Properties of High Temperature Superconductors. D. M. Ginsberg. New Jersey, World Scientific. **II**: 571.
- Atiyah, M. F., V. K. Patodi and I. M. Singer (1975). Math. Proc. Camb. Phil. Soc. **77**: 43.
- Bardeen, J., L. N. Cooper and J. R. Schrieffer (1957). "Theory of Superconductivity." Physical Review **108**: 1175.
- Barone, A. and G. Paternò (1982). Physics and applications of the Josephson effect. New York, Wiley.
- Barrett, S. E., J. A. Martindale, D. J. Durand, C. H. Pennington, C. P. Slichter, T. A. Friedmann, J. P. Rice and D. M. Ginsberg (1991). "Anomalous behavior of nuclear spin-lattice relaxation rates in $\text{YBa}_2\text{Cu}_3\text{O}_7$ below T_c ." Physical Review Letters **66**(1): 108-11.
- Beasley, M. R., D. Lew and R. B. Laughlin (1994). "Time-reversal symmetry breaking in superconductors: a proposed experimental test." Physical Review B Condensed Matter **49**(17): 12330-2.
- Bednorz, J. G. and K. A. Müller (1986). "Possible high T_c superconductivity in the Ba-La-Cu-O system." Zeitschrift für Physik B-Condensed Matter **64**: 189-93.
- Bickers, N. E., D. J. Scalapino and S. R. White (1989). "Conserving approximations for strongly correlated electron systems: Bethe-Salpeter equation and dynamics for the two-dimensional Hubbard model." Physical Review Letters **62**(8): 961-4.
- Buchholtz, L. J., M. Palumbo, D. Rainer and J. A. Sauls (1995). "Thermodynamics of a D-Wave Superconductor Near a Surface." Journal of Low Temperature Physics **101**(5-6): 1079-1098.
- Covington, M., M. Aprili, E. Paroanu, L. H. Greene, F. Xu, J. Zhu and C. A. Mirkin (1997a). "Observation of Surface-Induced Broken Time-Reversal Symmetry in $\text{YBa}_2\text{Cu}_3\text{O}_7$ Tunnel Junctions." Physical Review Letters **79**(2): 277-280.

- Covington, M., M. Aprili, E. Paraoanu, L. H. Greene, F. Xu, J. Zhu and C. A. Mirkin (1997b). "Observation of Surface-Induced Broken Time-Reversal Symmetry in $\text{YBa}_2\text{Cu}_3\text{O}_7$ Tunnel Junctions (Vol 79, Pg 277, 1997)." Physical Review Letters **79**(13): 2598.
- Covington, M. W. (1997c). Growth, transport, and tunneling spectroscopy of $\text{Y}_{1-x}\text{Pr}_x\text{Ba}_2\text{Cu}_3\text{O}_7$ thin films as a function of crystallographic orientation. Ph.D. thesis. Physics, University of Illinois, Urbana, IL.
- Dijkkamp, D., T. Venkatesan, X. D. Wu, S. A. Shaheen, N. Jisrawi, Y. H. Min-Lee, W. L. McLean and M. Croft (1987). "Preparation of Y-Ba-Cu oxide superconductor thin films using pulsed laser evaporation from high T_c bulk material." Applied Physics Letters **51**(8): 619-21.
- Ding, H., M. R. Norman, J. C. Campuzano, M. Randeria, A. F. Bellman, T. Yokoya, T. Takahashi, T. Mochiku and K. Kadowaki (1996a). "Angle-Resolved Photoemission Spectroscopy Study of the Superconducting Gap Anisotropy in $\text{Bi}_2\text{Sr}_2\text{CaCu}_2\text{O}_{8+x}$." Physical Review B-Condensed Matter **54**(14): R9678-R9681.
- Ding, H., T. Yokoya, J. C. Campuzano, T. Takahashi, M. Randeria, M. R. Norman, T. Mochiku, K. Kadowaki and J. Giapintzakis (1996b). "Spectroscopic Evidence For a Pseudogap in the Normal State of Underdoped High-T-C Superconductors." Nature **382**(6586): 51-54.
- Dynes, R. C. and T. A. Fulton (1971). "Supercurrent density distribution in Josephson junctions." Physical Review B (Solid State) **3**(9): 3015-23.
- Fogelstrom, M., D. Rainer and J. A. Sauls (1997a). "Tunneling Into Current-Carrying Surface States of High- T_c Superconductors." Physical Review Letters **79**(2): 281-284.
- Fogelstrom, M., D. Rainer and J. A. Sauls (1997b). "Tunneling Into Current-Carrying Surface States of High- T_c Superconductors (Vol 79, Pg 281, 1997)." Physical Review Letters **79**(14): 2754.
- Furusaki, A. and M. Tsukada (1991). "DC Josephson effect and Andreev reflection." Solid State Communications **78**(4): 299-302.
- Geerk, J., X. X. Xi and G. Linker (1988). "Electron tunnelling into thin films of $\text{Y}_1\text{Ba}_2\text{Cu}_3\text{O}_7$." Zeitschrift fur Physik B Condensed Matter **73**(3): 329-36.

- Gerchberg, R. W. and W. O. Saxton (1972). "A practical algorithm for the determination of phase from image and diffraction plane pictures." Optik **35**(2): 237-246.
- Gim, Y., A. Mathai, R. C. Black, A. Amar and F. C. Wellstood (1996). "Symmetry of the Phase of the Order Parameter in $\text{YBa}_2\text{Cu}_3\text{O}_{7-x}$." Journal de Physique I **6**(12): 2299-2316.
- Ginzburg, V. L. and L. D. Landau (1950). Zh. Eksp. Teor. Fiz. **20**: 1064.
- Gurevich, A. and E. A. Pashitskii (1998). "Current transport through low-angle grain boundaries in high-temperature superconductors [review]." Physical Review B-Condensed Matter **57**(21): 13878-13893.
- Hardy, W. N., D. A. Bonn, D. C. Morgan, R. Liang and K. Zhang (1993). "Precision measurements of the temperature dependence of λ in $\text{YBa}_2\text{Cu}_3\text{O}_{6.95}$: strong evidence for nodes in the gap function." Physical Review Letters **70**(25): 3999-4002.
- Hilgenkamp, H. and J. Mannhart (1998). "Superconducting and normal-state properties of $\text{YBa}_2\text{Cu}_3\text{O}_{7-x}$ -bicrystal grain boundary junctions in thin films." Applied Physics Letters **73**(2): 265-7.
- Hu, C. R. (1994). "Midgap Surface States As a Novel Signature For $d_{x^2-y^2}$ -Wave Superconductivity." Physical Review Letters **72**(10): 1526-1529.
- Il'ichev, E., V. Zakosarenko, V. Schultze, H. E. Hoening, H. G. Meyer, K. O. Subke, H. Burkhardt and M. Schilling (2000). "Current-phase relationship of $\text{YBa}_2\text{Cu}_3\text{O}_{7-x}$ ramp-edge Josephson junctions." Applied Physics Letters **76**(1): 100-2.
- Il'ichev, E., V. Zakosarenko, R. P. J. IJsselsteijn, V. Schultze, H. G. Meyer, H. E. Hoenig, H. Hilgenkamp and J. Mannhart (1998). "Nonsinusoidal current-phase relationship of grain boundary Josephson junctions in high- T_c superconductors." Physical Review Letters **81**(4): 894-7.
- Jorgensen, J. D., B. W. Veal, W. K. Kwok, G. W. Crabtree, A. Umezawa, L. J. Nowicki and A. P. Paulikas (1987). "Structural and superconducting properties of orthorhombic and tetragonal $\text{YBa}_2\text{Cu}_3\text{O}_{7-x}$: the effect of oxygen stoichiometry and ordering on superconductivity." Physical Review B Condensed Matter **36**(10): 5731-4.
- Kadin, A. M. (1990). "Analysis of the proximity-induced Josephson effect in superconducting-normal contacts." Physical Review B Condensed Matter **41**(7): 4072-7.

- Kane, J. and K. W. Ng (1996). "Angular dependence of the in-plane energy gap of $\text{Bi}_2\text{Sr}_2\text{CaCu}_2\text{O}_8$ by tunneling spectroscopy." Physical Review B Condensed Matter **53**(5): 2819-26.
- Kaufman, H. R. and R. S. Robinson (1987). Operation of Broad-Beam Sources. Alexandria, Virginia, Commonwealth Scientific Corporation.
- Kirtley, J. R., C. C. Tsuei, H. Raffy, Z. Z. Li, A. Gupta, J. Z. Sun and S. Meert (1996). "Half-Integer Flux Quantum Effect in Tricrystal $\text{Bi}_2\text{Sr}_2\text{CaCu}_2\text{O}_8+\Delta$." Europhysics Letters **36**(9): 707-712.
- Kos, S. (2001). "Physical mechanism of the surface d to d+is transition." Europhysics Letters **53**(2): 246-50.
- Kotliar, G. (1988). "Resonating valence bonds and d-wave superconductivity." Physical Review B Condensed Matter **37**(7): 3664-6.
- Lahiri, S. K. and S. Basavaiah (1978). "Lead-alloy Josephson-tunneling gates with improved stability upon thermal cycling." Journal of Applied Physics **49**(5): 2880-4.
- Lesueur, J., L. H. Greene, W. L. Feldmann and A. Inam (1992). "Zero bias anomalies in $\text{YBa}_2\text{Cu}_3\text{O}_7$ tunnel junctions." Physica C **191**: 325-332.
- Mannhart, J. and H. Hilgenkamp (1998). "Possible influence of band bending on the normal state properties of grain boundaries in high- T_c superconductors." Materials Science & Engineering B-Solid State Materials for Advanced Technology **56**(2-3): 77-85.
- Mathai, A., Y. Gim, R. C. Black, A. Amar and F. C. Wellstood (1995). "Experimental Proof of a Time-Reversal-Invariant Order Parameter With a B Shift in $\text{YBa}_2\text{Cu}_3\text{O}_{7-x}$." Physical Review Letters **74**(22): 4523-4526.
- Matsumoto, M. and H. Shiba (1995). "Coexistence of Different Symmetry Order Parameters Near a Surface in D-Wave Superconductors .1." Journal of the Physical Society of Japan **64**(9): 3384-3396.
- Millane, R. P. (1990). "Phase retrieval in crystallography and optics." Journal of the Optical Society of America A Optics & Image Science **7**(3): 394-411.
- Moler, K. A., D. J. Baar, J. S. Urbach, R. Liang, W. N. Hardy and A. Kapitulnik (1994). "Magnetic field dependence of the density of states of $\text{YBa}_2\text{Cu}_3\text{O}_{6.95}$ as determined from the specific heat." Physical Review Letters **73**(20): 2744-7.

- Monthoux, P., A. V. Balatsky and D. Pines (1992). "Weak-coupling theory of high-temperature superconductivity in the antiferromagnetically correlated copper oxides." Physical Review B Condensed Matter **46**(22): 14803-17.
- Moriya, T., Y. Takahashi and K. Ueda (1990). "Antiferromagnetic spin fluctuations and superconductivity in two-dimensional metals—a possible model for high T_c oxides." Journal of the Physical Society of Japan **59**(8): 2905-15.
- Ohashi, Y. (1996). "Unusual proximity effect of d-wave superconductivity." Journal of the Physical Society of Japan **65**(3): 823-39.
- Orlando, T. P. and K. A. Delin (1991). Foundations of Applied Superconductivity. Reading, Massachusetts, Addison-Wesley.
- Ouboter, R. D. B. and A. T. A. M. de Waele (1970). Superconducting Point Contacts Weakly Connecting Two Superconductors. Progress in Low Temperature Physics. C. J. Gorter. Amsterdam, Elsevier. **VI**.
- Papoulis, A. (1962). The Fourier integral and its applications. New York, McGraw-Hill.
- Prozorov, R., R. W. Giannetta, P. Fournier and R. L. Greene (2000). "Evidence for nodal quasiparticles in electron-doped cuprates from penetration depth measurements." Physical Review Letters **85**(17): 3700-3.
- Rokhsar, D. S. (1993). "Pairing in doped spin liquids: anyon versus d-wave superconductivity." Physical Review Letters **70**(4): 493-6.
- Rzchowski, M. S. and B. M. Hinaus (1997). "Extrapolation procedures in high- T_c gap-function experiments." Physica C **273**: 3-4.
- Scalapino, D. J. (1995). "The case for $d_{x^2-y^2}$ pairing in the cuprate superconductors." Physics Reports **250**(6): 329-65.
- Scalapino, D. J., J. R. Schrieffer and J. W. Wilkins (1966). "Strong-Coupling Superconductivity. I." Physical Review **148**(1): 263-279.
- Schlichter, C. P. (1994). Experimental Evidence of Spin Fluctuations in High Temperature Superconductors. Strongly Correlated Electronic Materials. K. S. B. e. *al.* New York, Addison-Wesley.

- Schweinfurth, R. (1994). Growth, Fabrication, and Measurement of Superconducting $Ba_{1-x}K_xBiO_3$ thin films and devices. Ph. D. thesis. Physics, University of Illinois at Urbana-Champaign, Urbana, IL.
- Sharifi, F. (1989). Thermal activation and macroscopic quantum phenomena in superconducting devices. Ph.D. thesis. Physics, University of Illinois, Urbana, IL.
- Sharma, S. K. and J. Spitz (1979a). "Hillock growth and agglomeration in thin silver films." Thin Solid Films **61**(2): L13-15.
- Sharma, S. K. and J. Spitz (1979b). "Hole growth in thin silver films." Thin Solid Films **56**(3): L17-19.
- Sharma, S. K. and J. Spitz (1980). "Hillock Formation, Hole Growth and Agglomeration in Thin Silver Films." Thin Solid Films **65**(3): 339-350.
- Shen, Z. X., D. S. Dessau, B. O. Wells, D. M. King, W. E. Spicer, A. J. Arko, D. Marshall, L. W. Lombardo, A. Kapitulnik, P. Dickinson, S. Doniach, J. DiCarlo, A. G. Loeser and C. H. Park (1993). "Anomalously large gap anisotropy in the a-b plane of $Bi_2Sr_2CaCu_2O_{8+x}$." Physical Review Letters **70**(10): 1553-6.
- Taillefer, L., J. Flouquet and G. G. Lonzarich (1991). "Normal and superconducting phases of heavy fermions." Physica B **169**: 257-70.
- Takeuchi, I., R. P. Sharma, S. Choopun, C. J. Lobb and T. Venkatesan (1997). "Ion Milling Damage and Regrowth of Oxide Substrates Studied By Ion Channeling and Atomic Force Microscopy." Applied Physics Letters **70**(23): 3098-3100.
- Tanaka, Y. (1994). "Josephson effect between s wave and $d_{x^2-y^2}$ wave superconductors." Physical Review Letters **72**(24): 3871-4.
- Thuneberg, E. V. A. V. (1988). "Microscopic theory of the proximity-induced Josephson effect." Physical Review Letters **60**(4): 365-8.
- Tinkham, M. (1964). Group theory and quantum mechanics. New York,, McGraw-Hill.
- Tinkham, M. (1996). Introduction to superconductivity. New York, McGraw Hill.
- Tsuei, C. C. and J. R. Kirtley (2000). "Phase-sensitive evidence for d-wave pairing symmetry in electron-doped cuprate superconductors." Physical Review Letters **85**(1): 182-5.

- Tsuei, C. C., J. R. Kirtley, C. C. Chi, L. S. Yujahnes, A. Gupta, T. Shaw, J. Z. Sun and M. B. Ketchen (1994). "Pairing Symmetry and Flux Quantization in a Tricrystal Superconducting Ring of $\text{YBa}_2\text{Cu}_3\text{O}_{7-x}$." Physical Review Letters **73**(4): 593-596.
- Tsuei, C. C., J. R. Kirtley, M. Rupp, J. Z. Sun, A. Gupta, M. B. Ketchen, C. A. Wang, Z. F. Ren, J. H. Wang and M. Bhushan (1996). "Pairing Symmetry in Single-Layer Tetragonal $\text{Tl}_2\text{Ba}_2\text{CuO}_{6+x}$ Superconductors." Science **271**(5247): 329-332.
- Van Harlingen, D. J. (1995). "Phase-sensitive tests of the symmetry of the pairing state in the high-temperature superconductors-Evidence for $d_{x^2-y^2}$ symmetry." Reviews of Modern Physics **67**(2): 515-35.
- Van Harlingen, D. J., J. E. Hilliard, B. L. T. Plourde and B. D. Yanoff (1999). "Extending SQUID interferometry beyond the cuprates and beyond d-wave symmetry." Physica C **318**: 410-420.
- Vartanyants, I., C. Ern, W. Donner, H. Dosch and W. Caliebe (2000). "Strain profiles in epitaxial films from x-ray Bragg diffraction phases." Applied Physics Letters **77**(24): 3929-3931.
- Vartanyants, I. A., J. A. Pitney, J. L. Libbert and I. K. Robinson (1997). "Reconstruction of Surface Morphology From Coherent X-Ray Reflectivity." Physical Review B-Condensed Matter **55**(19): 13193-13202.
- Waldram, J. R. (1996). Superconductivity of metals and cuprates. Bristol, UK ; Philadelphia, Institute of Physics Pub.
- Walter, H., W. Prusseit, R. Semerad, H. Kinder, W. Assmann, H. Huber, H. Burkhardt, D. Rainer and J. A. Sauls (1998). "Low-Temperature Anomaly in the Penetration Depth of $\text{YBa}_2\text{Cu}_3\text{O}_7$ Films - Evidence For Andreev Bound States At Surfaces." Physical Review Letters **80**(16): 3598-3601.
- Wolf, E. L., E. V. Thuneberg, V. Ambegaokar, S. Han and K. W. Nh (1989). "Comment on 'Microscopic theory of the proximity-induced Josephson effect' (and reply)." Physical Review Letters **62**(19): 2334-5.
- Wollman, D. A. (1996). Experimental determination of the symmetry of the superconducting pairing state in YBCO. Ph. D. thesis. Physics, University of Illinois, Urbana, IL.

- Wollman, D. A., D. J. Van Harlingen, J. Giapintzakis and D. M. Ginsberg (1995). "Evidence for $d_{x^2-y^2}$ pairing from the magnetic field modulation of $\text{YBa}_2\text{Cu}_3\text{O}_{7-x}$ -Pb Josephson junctions." Physical Review Letters **74**(5): 797-800.
- Wollman, D. A., D. J. Van Harlingen, W. C. Lee, D. M. Ginsberg and A. J. Leggett (1993). "Experimental determination of the superconducting pairing state in YBCO from the phase coherence of YBCO-Pb dc SQUIDs." Physical Review Letters **71**(13): 2134-7.
- Wu, D. H., J. Mao, S. N. Mao, J. L. Peng, X. X. Xi, T. Venkatesan, R. L. Greene and S. M. Anlage (1993). "Temperature dependence of penetration depth and surface resistance of $\text{Nd}_{1.85}\text{Ce}_{0.15}\text{CuO}_4$." Physical Review Letters **70**(1): 85-8.
- Wu, M. K., J. R. Ashburn, C. J. Torng, P. H. Hor, R. L. Meng, L. Gao, Z. J. Huang, Y. Q. Wang and C. W. Chu (1987). "Superconductivity at 93 K in a new mixed-phase Y-Ba-Cu-O compound system at ambient pressure." Physical Review Letters **58**(9): 908-10.
- Zappe, H. H. (1975). "Determination of the current density distribution in Josephson tunnel junctions." Physical Review B (Solid State) **11**(7): 2535-8.
- Zhang, W. Y. (1995). "Identifying the Superconducting Pairing State of High-T-C Oxides by the Josephson Effect." Physical Review B-Condensed Matter **52**(5): 3772-3775.

VITA

Joseph Edward Hilliard Jr. was born on November 1, 1967 in Oak Park, Illinois. He pursued undergraduate education at the Massachusetts Institute of Technology where he received his B.S. in Physics with Electrical Engineering option (course VIIIA) in 1989. While at M.I.T., he was elected to the Sigma Pi Sigma physics honor society. From 1989 to 1991, he worked at M.I.T. Lincoln Laboratory in the High Energy Laser Beam Control and Propagation group under the leadership of Dr. Charles Primmerman.

Joseph Hilliard came as a graduate student in physics to the University of Illinois at Urbana-Champaign in 1991, where he spent his first year as a University Fellow. In 1992, he received his M.S. in physics. He worked from 1992 to 1995 in the research group of Prof. Munir Nayfeh on photoluminescence in porous silicon. From 1995 until the completion of his Ph. D. Joseph Hilliard worked in the research group of Prof. Dale Van Harlingen primarily on thin film Josephson experiments in $\text{YBa}_2\text{Cu}_3\text{O}_{7-y}$ (YBCO). Joseph also did some preliminary work on Nb/CuNi/Nb sandwich Josephson junctions during this time.

To date, Joseph Hilliard has been a co-author of eight published papers in Applied Physics Letters, Journal of Applied Physics and Physica C. He has also delivered five contributed talks at American Physical Society March Meetings.

Beginning in 2001, Joseph Hilliard will be employed in the Radar Design and Electronics Laboratory of Raytheon Corporation in Tewksbury, Massachusetts.